DISSERTATION

submitted to the

Combined Faculties for the Natural Sciences and for Mathematics

of the Ruperto-Carola University of Heidelberg, Germany

for the degree of

Doctor of Natural Sciences

presented by

Dipl.-Phys. Isabel Braun

born in Karlsruhe

Oral examination: May 2nd 2007

Improving the Pointing Precision of the H.E.S.S. Experiment

Referees:
Prof. Dr. Werner Hofmann
Prof. Dr. Stefan Wagner

Abstract

The H.E.S.S. experiment consists of four *Imaging Atmospheric Cherenkov Telescopes (IACTs)* located in Namibia. IACTs collect the Cherenkov light emitted from the cascade of secondary particles that is created when γ-rays interact with the atmosphere. The direction of individual γ-rays can be measured to about 0.1°, but the average source position can be determined to higher accuracy and systematic errors in telescope pointing can emerge as the main limitation. Typical pointing accuracies for IACTs are in the order of arc-minutes.
In H.E.S.S., the pointing is determined from reference measurements of stars. The telescope is pointed at a star while the Cherenkov camera is covered by a lid serving as screen for the reflection. A CCD Camera monitors the location of this reflection relative to the focal plane represented by positioning LEDs. A second CCD camera acts as guiding telescope. The systematic errors of possible influences on the pointing accuracy are discussed. An alternative pointing technique using CCD information measured in parallel to γ-ray observations is presented and compared to the standard method. The new method approximately bisects the systematical error on the pointing of the H.E.S.S. experiment to 6". Its validity is tested on point-like γ-ray sources of known position.

Kurzfassung

Das H.E.S.S. Experiment in Namibia besteht aus vier *Abbildenden Atmosphärischen Cherenkov-Teleskopen*, die anhand des Cherenkov Lichts von Sekundärteilchen aus der Wechselwirkung kosmischer Strahlung in der Atmosphäre die kosmische Gammastrahlung vermessen. Die Herkunftsrichtung eines einzelnen hochenergetischen Photons kann mit etwa 0.1° Genauigkeit gemessen werden, aber die mittlere Quellposition in einem großen Datensatz kann statistisch genauer bestimmt werden, wodurch systematische Fehler in der Kenntnis der Beobachtungsrichtung des Teleskops zum limitierenden Faktor werden können. Typischerweise liegt die Genauigkeit der Bestimmung der Beobachtungsrichtung für Teleskope dieser Art im Bereich von Bogenminuten.
Bei H.E.S.S. erfolgt die Bestimmung der Beobachtungsrichtung über Referenzmessungen an Sternen, auf welche das Teleskop ausgerichtet wird während die Cherenkov Kamera mit einer Abdeckung verschlossen ist, die als Abbildungsschirm dient. Eine CCD Kamera mißt den Ort des Sternbildes relativ zur Brennebene, welche von acht Leuchtdioden markiert wird. Eine zweite CCD Kamera agiert als Führungsteleskop. Die systematischen Fehler verschiedener Einflüsse auf die Beobachtungsrichtung werden diskutiert. Eine alternative Methode, die zeitgleich mit Cherenkov Beobachtungen gemessene CCD Informationen verwendet, wird präsentiert und mit der Standardmethode verglichen. Mit der neuen Methode wird der systematische Fehler der Kenntnis der Beobachtungsrichtung etwa halbiert auf 6". Tests an punktförmig erscheinenden γ-Quellen bekannter Position werden durchgeführt.

Contents

Introduction

Historic astronomers in China, Egypt, Greece or Polynesia studied the stars with the most advanced detectors available to them: their eyes. Worshiping the lights in the sky as gods, they eventually learned about their value for navigation, animal migration and agriculture. But human curiosity did not come to an end, and societies supporting science gradually collected an impressive knowledge about night sky objects. In Greece, astronomy was combined with mathematics to create cosmological models, while ancient Romans enjoyed the practical use of calendars and astrological predictions. In China, astronomy even merged with politics, because false predictions meant that the current ruler lost his justification. Due to this policy, the country has experienced fifty calender reforms up to today.

The invention of the telescope enabled scientists to extend the reach of their natural detector. To extend research possibilities even further, as much information as possible about a tested object had to be collected, so the development of new detection techniques became an important motor for scientific discoveries in different fields. Every exploration of a new electromagnetic frequency band in astronomy was followed by surprises and major detections, and the multi-wavelength picture of the universe gained more and more importance. The most recently explored wavelength band is studied by γ-ray astronomy.

The field of γ-ray astronomy is tightly connected to cosmic ray astrophysics, which has been the experimental side of nuclear and particle physics before particle accelerators. It has come a long way from the detection of air showers with the first electroscopes, cloud chambers and Geiger counters to current precision experiments like the H.E.S.S. Experiment, which is designed to detect the sources of cosmic γ-radiation and ultimately answer the question about the origin of cosmic rays.

To do so, the identification of detected γ-ray sources with counterparts in other wavelengths is an important step, especially in regions with more than one possible association like the Galactic Centre region.

The first chapter of this work will answer the question, what we can learn about the universe from gamma-ray astronomy. Cosmic rays and their production sites are introduced and their connection to cosmic gamma-rays is shown.

The second chapter presents methods and the experimental requirements for gamma-ray telescopes, with details about the H.E.S.S. experiment and its subsystems.

The third chapter covers the standard pointing procedure of the H.E.S.S. experiment. In H.E.S.S., reference runs on stars are used to model the image of a tracked sky location relative to the pixel matrix of the Cherenkov camera. The information is recorded by a CCD camera viewing the H.E.S.S. camera from the centre of the dish.

When a certain level of precision is reached, the accuracy of a position measurement can no longer be increased with the collection of more data and systematical effects have to be investigated. Individual effects determining the accuracy of this method are identified, quantified and finally combined into the systematic pointing error of the telescope system in chapter 4.

A new method to determine the observation direction with pointing information collected in parallel to γ-ray observations and the expected improvement from this method are discussed in the fifth chapter. Again a systematic error is derived and tested using an independent method.

The sixth chapter tests this new procedure on a gamma-ray point source of known position, the active galactic nucleus PKS 2155-304. Several consistency tests are shown to determine the validity of the given systematic error. The new precision pointing method will be applied to other point sources observed with H.E.S.S.

1 Gamma-Ray Astronomy

Gamma-ray astronomy is in many ways extraordinary. It explores the universe in the light of photons with extremely high energies up to TeV or PeV. The hottest stable objects in the universe emit continuous thermal radiation only up to about 10 keV; more energetic γ-rays cannot be produced thermally but are messengers of the most violent energy outbursts in our universe. In addition to the remarkable sources of the field, special detection techniques are required due to the lack of focusing optics for the studied photons and methods of particle physics are applied to astronomy.

Gamma-ray astronomy is tightly connected to cosmic ray research which was started by Viktor Hess in 1912, because it offers the possibility to identify the sources of the isotropic cosmic ray particles. The detection of the first γ-ray source emitting in the energy range of the H.E.S.S. Experiment in 1989 [CFG89] started the success of the field, even though the number of sources is still very limited compared to astronomy in other wavelengths. This chapter will present the relationship between comic rays and γ-rays. It starts with an introduction into the properties and possible acceleration mechanisms of cosmic rays, followed by an overview on γ-radiation and the processes leading to its emission. Both threads are then combined into a short review of the processes assumed to occur in different source classes.

1.1 Goals

The primary goal of γ-ray astronomy is to solve the mystery about the origin of cosmic radiation and the mechanism that is able to accelerate particles to energies of up to 10^{20} eV. Under certain conditions, photons are produced as secondaries of charged cosmic rays, but in contrast to the latter, they do not loose their directional information in interstellar magnetic fields on the way to earth. In addition, information about the mechanism responsible for the acceleration can be deduced from spectral properties of the γ-rays. Therefore, gamma-ray astronomy can pinpoint objects and processes that generate the highest energies in the universe.

Sources for γ-ray astronomy usually include extreme astrophysical objects like active galaxies, supernovae and their remnants or pulsars and pulsar wind nebulae. Several source types will be presented in chapter 1.4.

Even more exotic origins are possible, such as photons produced in the self-annihilation of dark matter particles in regions with high dark matter density. Galaxies are expected to be embedded into large scale dark matter structures, most likely forming halos with a dense cluster located at the galactic centre. Various possible candidates have been proposed as extensions of the standard model of particle physics. Their annihilation may produce γ-rays up to an energy corresponding to the mass of the dark matter particle, therefore a distinction between the models could be possible if the predicted dark matter signature was detected in γ-rays (e.g. [Aha06d]).

Another application uses the fact that high energy gamma-rays cannot pass intergalactic distances completely unhindered: they are absorbed by interactions with photons of the extragalactic background light (EBL) via pair-production. The range decreases with energy and steepens the observed spectrum of distant sources. Comparing similar remote objects at various distances enables one to probe the properties of the EBL photon field. [Aha06b]

For many questions, the precise knowledge on the position of γ-ray emission is vital to correctly identify the source. This work presents the efforts taken to understand and minimize systematic errors in the determination of the telescope orientation during γ-ray observations with the H.E.S.S. experiment. The resolution of previous experiments was typically in the order of arc minutes (0.05°-0.1° for the Whipple Telescope [SBB05]). The HEGRA telescope system reached a pointing accuracy of 0.01° [PDH97]. In this work, it will be shown that the H.E.S.S. experiment can reach 6" or 0.002° pointing accuracy.

1.2 Cosmic Rays

In 1912 Victor Franz Hess initiated cosmic ray research with a series of balloon experiments indicating that electroscopes discharged faster with increasing height [Hes12]. The discharge was caused by energetic particles ionizing the air between the capacitor plates of the electroscope. The electrons and ions created would drift to the poles and reduce their charge. Radioactive minerals in the earth were known as a source of radiation, so the measured radiation level was expected to decrease with increasing distance from the ground [Wul09]. When the opposite was found, Hess came to the conclusion that the additional component had to be of extraterrestrial origin and even excluded the sun as the main source comparing flights at different times of the day. In 1936, Hess was awarded the Nobel prize for this discovery. Since then, many balloons have ascended to investigate this extraterrestrial radiation, and were soon followed and complemented by satellites carrying elaborate detectors to study its composition. The dominant component found were protons (85%), followed by other fully ionized nuclei in relative abundances similar to those known from the solar system (yielding

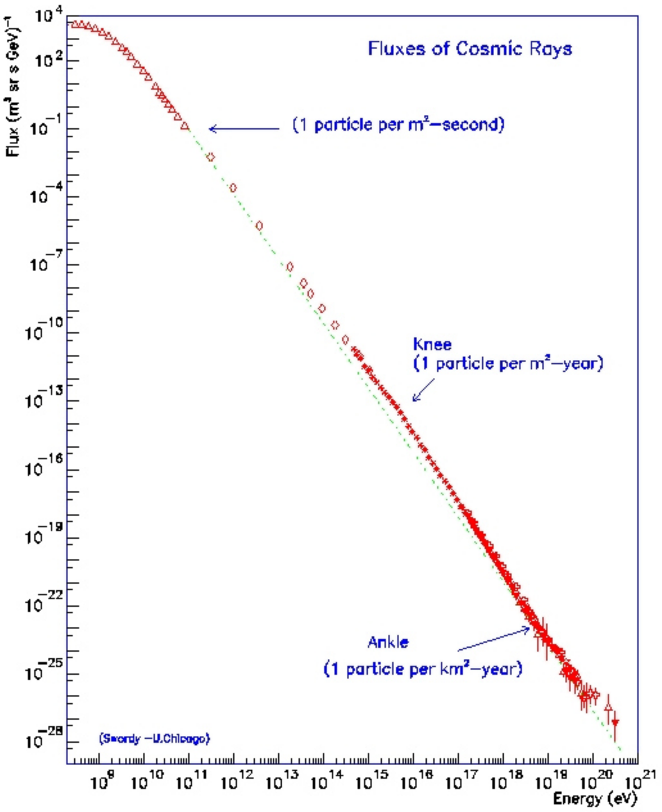

Figure 1.1: **Cosmic Ray Spectrum**, from [CGS97]. Shown is the measured differential flux (per energy bin) as a function of the energy of the Cosmic Ray particle. The spectrum is remarkably featureless with two changes of the power law index known as the knee and the ankle marked in the figure. A line indicating a simple power law is inserted to demonstrate the changes in slope. The data points of many direct and indirect measurements are combined.

about 12% helium, only 1% heavier elements), as well as 2% electrons. Only a fraction of about 10^{-4} are gamma rays and neutrinos. The total energy density is about 1 $\mathrm{eV/cm^3}$, comparable to that of interstellar magnetic fields.

In addition to the *primary* particles accelerated to relativistic energies in powerful cosmic sources, a *secondary* component is produced by the interaction of primary cosmic rays with interstellar gas or plasma. These secondary cosmic rays include nuclei of the (Li,Be,B) group that are more frequent in cosmic rays than expected from local abundances, as well as antiparticles. From the ratio of those secondaries one can estimate the escape time of primary cosmic rays from the galactic disk to be in the order of $3 \cdot 10^7$ years [LFM94].

Very high energy electrons suffer severe radiative losses in the interstellar medium, so their sources cannot be located further away than a few hundred parsecs to explain the observed energies. [AAV95]

The energy spectrum of cosmic rays (figure 1.1) covers at least 14 orders of magnitude in energy, extending from 10^6 eV with fluxes of about thousand particles per square metre and second, to 10^{20} eV, with only one particle per square kilometer and century [CGS97]. For energies beyond the influence of solar modulation (i.e. higher than some 10^9 eV), it basically follows a power law in energy like

$$\frac{dN}{dE} \sim E^{-\gamma} \tag{1.1}$$

with a spectral index γ of 2.7. Two additional features are observed: a steepening around 10^{15} eV to a photon index of about 3 called the *knee* and a flattening around $4 \cdot 10^{18}$ eV, known as the *ankle*. There is indication for a third structure at $\sim 4 \cdot 10^{17}$ eV, the *second knee*. The origin of the knee is still under discussion. Explanations range from the limit of acceleration in supernovae to propagation or interaction processes in interstellar space and even a possible energy transfer into unobserved particles within Earth's atmosphere. It is currently believed that at least a large fraction of the cosmic rays are accelerated in supernovae up to energies of $Z \times (0.1 - 5) \times 10^{15}$ eV depending on their nuclear charge Z. Higher energies are produced by additional sources, e.g. in γ-ray bursts having a larger escape propability from diffusion through the galactic disk with ingreasing energy [Hör05]. From the energy dependence of the secondary-to-primary ratio one can deduce that the acceleration spectra at the sources must be *harder* than the locally measured spectrum, meaning they have more particles with higher energies or a smaller spectral index γ.

The collection of particles at the highest energies known so far requires enormous detection areas and brought the experiments back to the ground. Air shower arrays detect the cascade of secondary particles created when a cosmic ray interacts with the atmosphere and have recorded events from primary particles with energies of up to 10^{20} eV [BCD93].

Possible sources for cosmic radiation are supernovae and their remnants, fast rotating objects like pulsars and neutron stars, binary systems, active galactic nuclei and accreting black holes. Chapter 1.4 gives more information about some of those source types. How the sources might actually produce the observed energetic particles is discussed in a general manner in the next chapter.

1.2.1 Cosmic Ray Acceleration

Man-made accelerators typically accelerate charged particles in electric fields. Yet, one can assume that most stellar objects themselves are neutral and that electrostatic fields would have been neutralized by interstellar plasmas (exception: environment of pulsars). Therefore varying magnetic fields, applying Faraday's law of induction

$\nabla \times E = -\partial B/\partial t$, are the only cosmic source of "traditional" electromagnetic acceleration.

Even regular stars can accelerate charged particles up to about 10^{11} eV in variable magnetic fields created by plasma turbulences. The acceleration regions can often be seen as sunspots, because the locally higher magnetic energy density requires a lower thermal energy for the region to be in energetic equilibrium. Therefore sunspots are cooler, hence darker than their surroundings. Stellar magnetic fields in sunspots are usually in the order of 0.1 T, but can reach local field strengths of up to several Tesla, which could roughly explain the observed energies through cyclotron acceleration or the changing dipole moment of drifting sunspot pairs.

Higher energies require extremely strong magnetic fields (occurring in pulsars, see section 1.4.2) or different acceleration mechanisms that should still reproduce the observed power law spectrum. Any repeatable process where a particle with initial energy E_0 gains an amount of energy ΔE proportional to its current energy ($\Delta E = \epsilon E$) and has a certain escape probability p will create a power law spectrum (see appendix A).

One of the most successful models of shock acceleration is the Fermi acceleration, which will be discussed in more detail in the following section.

1.2.1.1 Fermi acceleration

The acceleration on shock fronts and moving magnetic clouds is known as Fermi acceleration of first and second order, respectively. These two models are so far the only acceleration theories allowing quantitative predictions of the Cosmic Ray spectrum.

Fermi acceleration was originally proposed by Fermi in 1949 as stochastic gain of energy from collisions with irregularities of magnetic fields and was later adapted for shock front scenarios. Its main ideas are illustrated in figure 1.2. The shock front is created by a flow of particles hitting a cloud of material at rest. It progresses through the medium with a velocity U, that is smaller than the average peculiar speed of the energetic particles. The shock is assumed to be thin compared to the gyro-radius of the particles, so some may pass through it in either direction. They are scattered on turbulences or irregularities on the other side, yielding an isotropic velocity distribution. Considering a frame in which one side of the shock is at rest, the particle gets thermalized in the flow speed of the new region after crossing the shock and gains energy. This argument holds for both sides of the shock, so a particle gains energy with each crossing of the shock front until it escapes the shock region.

The average gained energy depends linearly on the relative velocity of the shock front to the medium. For an ideal gas it is given by

$$\frac{\Delta E}{E} = \frac{2}{3}\frac{U}{c}. \qquad (1.2)$$

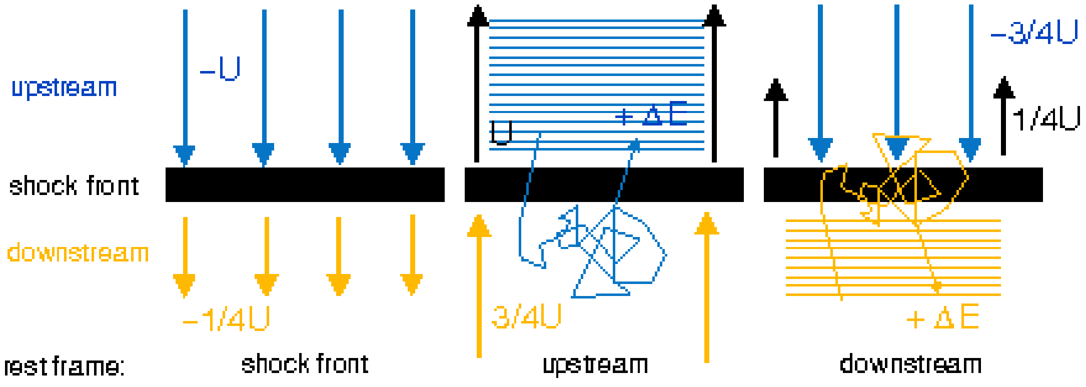

Figure 1.2: **Fermi Acceleration** in a shock wave with velocity U propagating into an upstream medium, figure from [Fun05]. The three image segments show the situation in the rest frames of the shock front (left), the upstream (middle) and the downstream medium (right). In the rest frame of the shock front, the interstellar medium moves toward the shock with a velocity of $-U$, while the shocked downstream medium follows with a lower velocity, which is $-1/4\,U$ for an ideal gas. In the rest frame of the upstream region, upstream particles at rest encounter gas of the downstream region coming towards them with a velocity of $3/4\,U$. They scatter on downstream turbulences and get thermalized with the flowing medium gaining the energy ΔE. In the rest frame of the downstream region, particles again encounter gas coming towards them with a speed of $3/4\,U$. They may diffuse into the upstream region and undergo the same process to increase their energy by ΔE. Therefore, each passage through the shock front increases the energy of the particle independent of the direction of the crossing.

An initially mono-energetic spectrum evolves into a power-law $dN/dE \propto E^{-\gamma}$ with a spectral index $\gamma = 2$. Exact calculations including more realistic assumptions differ slightly from this result.

As the energy gain is linear in U, this type of acceleration is called first order Fermi acceleration. The main difference from the original idea of Fermi is that the direction of movement is governed by the propagation of the shock. If each step occurred on a "magnetic mirror" or magnetic cloud moving in a randomized direction, the energy gain would only be proportional to $(U/c)^2$. This scenario is called second order Fermi acceleration. More details about both types of Fermi acceleration can be found in [Lon94].

Cosmic rays accelerated to very high energies are believed to create secondary energetic photons. Since those would point back to the production region when they reach earth and their spectral distribution carries information about the mechanism they were created in, the study of those photons can be used to indirectly study cosmic ray acceleration. The next chapter will focus on energetic photons.

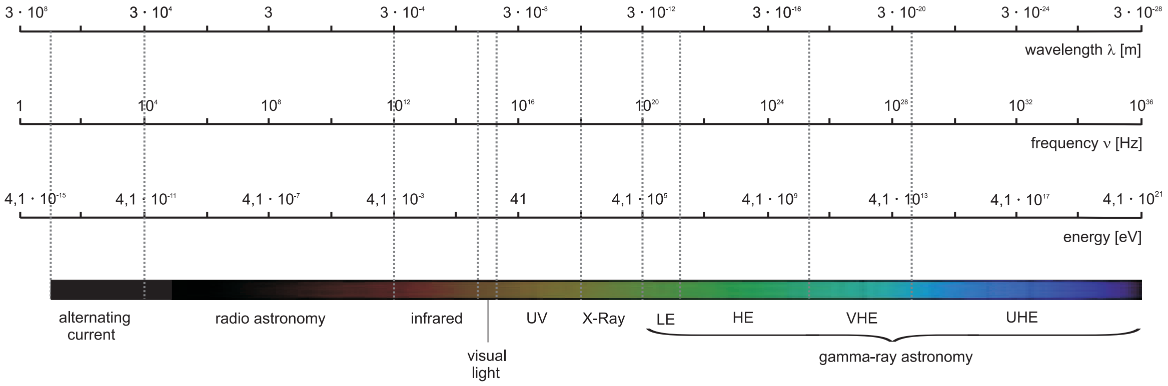

Figure 1.3: **Spectrum of electromagnetic radiation** in different useful units. Based on [Gru00], adapted by [Kuz06]

1.3 γ-radiation

Electromagnetic waves are found over a huge spectral range (see figure 1.3), but only a minority of these energies are directly accessible to ground-based astronomy. The atmosphere is transparent for visual light and in the near radio range from 1 cm to 100 m. Apart from those two wide frequency bands and some narrow windows in the infrared, the atmosphere does not transmit photons.

The term γ-ray refers to the upper end of the spectrum and applies to photons over at least 14 decades in frequency from $E = mc^2 = h\nu \approx 0.5 \cdot 10^6$ eV to more than 10^{20} eV, therefore the energy range of γ-rays covers photon energies of MeV (10^6 eV), GeV (10^9 eV), TeV (10^{12} eV) and PeV (10^{15} eV). Due to very different interaction properties at the various energies, the following sub-divisions are used e.g. in [Aha04a]:

- low energy (LE): below 30 MeV, LE γ-rays are the only ones that can still be produced by line emission of nuclear states, typical detection via Compton scattering.
- high energy (HE): 30 MeV - 30 GeV, up to this energy range γ-rays are best detected in satellite or balloon experiments, typical detection via pair production.
- very high energy (VHE): 30 GeV - 30 TeV typical detection via Cherenkov radiation.
- ultra high energy (UHE): 30 TeV - 30 PeV, typical detection in Air Shower Arrays, and
- extremely high energy (EHE): above 30 PeV, due to interaction with the microwave background radiation, the mean free paths in the PeV range are reduced to several kpc or Mpc, allowing only sources in our own Galaxy to be observed.

The limits between those energy ranges are not sharp and may differ between authors, so the values given above should be considered as rough and somewhat arbitrary ranges. This work will focus on VHE γ-rays observed with the H.E.S.S. array of Imaging Atmospheric Cherenkov Telescopes.

1.3.1 Suitable detectors

The wavelengths of γ-rays are too short to use traditional focusing lenses or deflectors, making it necessary to develop new detector designs. The most effective detection method for gamma-rays depends on their energy. In principle, it uses the inverse process of the typical production mechanism in each energy range: low energies up to a few hundred keV are best detected using the photo-effect, while MeV-energies are detected using the Compton-effect. For very high energies in the GeV-regime, pair-production is the dominant interaction effect and therefore the primary underlying detection principle.

The opacity of Earth's atmosphere to gamma rays represents an obstacle for ground based gamma-ray astronomy. Hence telescopes for this energy range have to be transported above the atmosphere in satellites. Above about 100 GeV, the flux becomes too low to effectively operate satellite telescopes and new techniques must be applied. Chapter 2.1 describes in more detail a very successful approach for the energy range between 100 GeV and a few TeV, the Atmospheric Cherenkov Technique. It is based on the detection of Cherenkov light from cascades produced by γ-rays in the atmosphere. Using the atmosphere itself as a detector, large collection areas become available for reasonable costs.

At energies above $\sim 10^{12}$ eV, secondary particles from gamma-ray induced showers may reach the ground and can be detected by the water Cherenkov experiment Milagro [Atk04] or at even higher energies by segmented air shower experiments like Auger [Man06].

1.3.2 Production mechanisms of γ-rays

Since thermal emission cannot explain the observed energies of γ-ray photons, the question about their origin arises. In contrast to emission in other wavebands, it cannot be answered thoroughly with one or two production mechanisms. Apart from the emission by thermal relativistic plasmas, it generally requires the interaction of energetic particles with targets like interstellar matter, magnetic fields or photons of lower energies. Various interaction processes compete for different particles in different environments, so groupings often refer to the accelerated particle (leptonic vs. hadronic), the nature of the interaction (e.g. absorption vs. radiation) or the type of the target (matter, photons or magnetic fields). The important processes and their implication

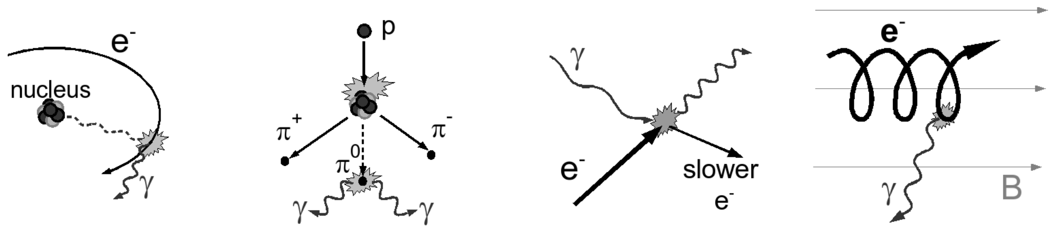

Figure 1.4: **Illustration of γ-ray production mechanisms.** From left to right: Bremsstrahlung, π^0-decay, inverse Compton scattering, synchrotron radiation

for γ-ray observations are discussed in e.g. [Aha04a]. Following the division of this book, a short overview will be given below.

1.3.2.1 Interactions with matter

Four major production channels for photons from accelerated particles in matter are found: *Bremsstrahlung*, π^0*-decay* after nucleon-nucleon interactions, e^+*-annihilation* and *nuclear transitions.* Photons produced by the annihilation of relativistic positrons and de-excitation of nuclei after neutron capture typically have energies in the MeV regime, but photons from Bremsstrahlung and π^0-decay reach the VHE energy range.

Bremsstrahlung The radiation emitted from charged particles due to acceleration is called Bremsstrahlung. It occurs for protons as well as for electrons, but is very inefficient for relativistic protons so they can be neglected. The energy loss rate dE_e/dt is proportional to the electron energy E_e, therefore the lifetime

$$t_{br} = \frac{E_e}{-dE_e/dt} \tag{1.3}$$

of a particle undergoing Bremsstrahlung is independent of energy and the slope of a power-law spectrum is unchanged by Bremsstrahlung. The produced γ-ray spectrum is continuous and in case of a power-law spectrum for the primary electrons reproduces their spectral shape and index Γ. This holds as long as ionization losses can be neglected, which are independent of E_e and reduce the photon index of both the electron and γ-ray spectrum to $\Gamma - 1$.

Decay of neutral pions produced by relativistic protons Relativistic protons collide inelastically with gas nuclei and transfer about half their energy to secondary pions (π) and kaons. The neutral pions decay almost immediately ($\tau_{\pi^0} = 8.4 \times 10^{-17}$ s) into two γ-rays, while the charged pions decay into muons and neutrinos with a longer lifetime of $\sim 2.6 \times 10^{-8}$ s. Equal amounts of energy go into each channel due to isospin symmetry, therefore photons carry one sixth of the proton energy. Similar to Bremsstrahlung, the γ-ray spectrum essentially follows the spectrum of the parent protons above ~1 GeV, hence VHE photons carry direct information about the acceleration spectrum of protons. This important property was already known to pioneers of the field (see [GS69]).

1.3.2.2 Interactions with photon fields

The most important production mechanism in photon fields is the *inverse Compton effect.* Hadrons (N) may additionally create pions from photo-meson productions ($N + \gamma \rightarrow N + k\pi$), that may again decay into photons as described above.

Inverse Compton scattering When energetic photons scatter on free electrons, they may transfer some of their energy to the electron, which is known as Compton effect. Electrons with very high energies may experience the inverse of this effect and loose some of their energy to lower energy photons. The averaged cross-section depends only on the product of the electron and photon energy. A power law distribution of electrons with photon index Γ will result in a power law with photon index $(\Gamma+1)/2$ in the non-relativistic regime [GS68], or a steeper spectrum following $E_\gamma^{-(\Gamma+1)}(ln(\Gamma+1)+const)$ for the ultra-relativistic case [BG70]. Inverse Compton scattering on primary protons is suppressed by a factor of $(m_e/m_p)^4$, so practically irrelevant.
Astrophysical objects offer plenty of photons from black-body radiation or starlight that might be up-scattered in such a fashion. Therefore, it works effectively almost everywhere, from compact objects like pulsars or AGN to extended SNR and also in the intergalactic medium scattering on infra-red background radiation.

1.3.2.3 Interactions with magnetic fields

Synchrotron radiation In magnetic fields, charged particles are deflected by the Lorentz force and travel on spiral arcs, thus radiating photons. The effect is very similar to the inverse Compton effect, as it can be seen as IC on the virtual photons of the magnetic field. Generally, the energy of Synchrotron photons is much smaller than that of the parent particle. For protons, production efficiencies are generally too low to be significant, but may be relevant for compact accelerators of $\sim 10^{20}$ eV. Synchrotron photons typically show a spectral cutoff at a position that depends on the mass of the emitting particle ($\sim$ 160 MeV for e^- and $\sim$ 300 GeV for protons). In case of a relativistically moving source it may be shifted towards the GeV and TeV range, respectively.

1.3.2.4 γ-ray absorption

All those production processes are countered by pair production according to $p+\gamma \rightarrow p+e^{+}+e-$ or $\gamma+\gamma \rightarrow e^{+}+e-$. Pair production prevents the escape of energetic γ-rays from compact objects and determines the *γ-ray horizon*.

1.4 Sources of VHE γ-rays

To identify the sources of cosmic rays, one may look for the sources of cosmic gamma-rays, but as discussed before, not all sources detected in γ-rays necessarily also produce the hadronic constituents. Accelerated electrons have a limited range of only a few hundred parsecs. If the measured hadronic cosmic rays were coming from the same sources, the accumulated deflection could not account for the observed isotropic distribution. Therefore, it is necessary to identify sources that unambiguously accelerate protons, in order to solve the cosmic ray question.

Known source classes and candidates include sources visible in our galaxy like supernovae and their remnants, pulsars, X-Ray binaries and accreting black holes, as well as the extragalactic active galactic nuclei (AGN).

1.4.1 Supernova Remnants

When a massive star runs out of fuel for hydrogen burning, it collapses until the core temperature is sufficient to initiate the fusion of helium. Depending on the stellar mass, this process may repeat for other fusion stages until the gravitational energy of the contraction is not enough to start the next reaction or until it has finished iron burning and can no longer gain energy from fusion. The inner Chandrasekhar mass ($M_{Ch} \sim 1.4\ M_{Sun}$) of an iron core cannot be supported by electron degeneracy pressure and contracts further. In the process, the pressure is reduced by disintegration of heavy ions and the conversion of electrons and protons to neutrons and neutrinos. The contraction becomes a rapid collapse that continues until the inner core reaches nuclear density, and is stopped by the neutron degeneracy pressure. The impact of the rest of the in-falling core creates an outward going shock carrying an energy of $O(10^{51})$ ergs that traverses the collapsing core and ejects the so far relatively undisturbed outer layers in a so-called supernova explosion.

Eventually, the outer hull hits the previously (in slower stellar winds) emitted material or the interstellar medium, where it may form a shock front in the supernova remnant. Particles accellerated in this shock may emit γ-rays in an interacion with this hull material.

Supernovae and their remnants have been the classical suspect for cosmic ray acceleration from energetic considerations. Only 10% of the energy released in the expected

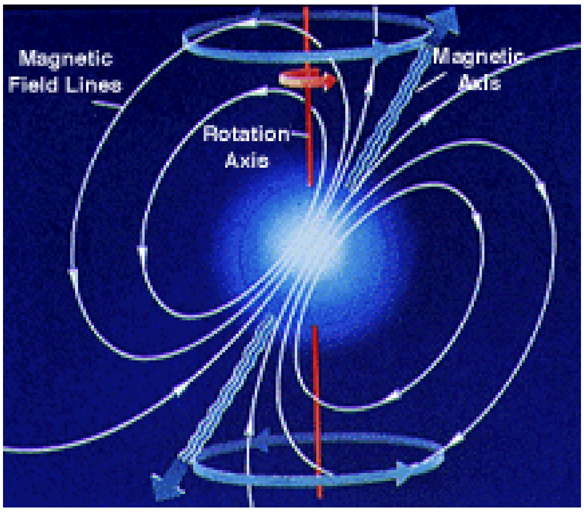

Figure 1.5: **Pulsar model** [God07].

explosions in our galaxy is sufficient to fuel cosmic rays. The presence of energetic shock fronts allowing first order Fermi acceleration additionally supports this hypothesis. The maximum energy from supernova explosions coincides with the knee of the cosmic ray spectrum, implying that higher energies have a different origin.

Gamma rays resulting from supernova explosions might be detectable in the first seconds of the explosion as *gamma ray bursts*, from the expanding supernova remnant [Aha06a] or as steady, periodic emission from the inner pulsar.

1.4.2 Pulsars

The remaining core of a supernova of the type described above is a neutron star, a compact object with nuclear density consisting of neutrons and supported by the neutron degeneracy pressure. Still, it may contain most of the angular momentum and magnetic field that once belonged to the much larger progenitor star.

Conservation of angular momentum yields very high rotational velocities. Ignoring mass losses during the contraction, one gets

$$T_{remnant} = T_{star} \cdot \frac{R^2_{remnant}}{R^2_{star}} \tag{1.4}$$

for the rotational periods T as function of the object radii R. Assuming $R_{star} = 10^9$ m, $T_{star} = 1$ month and a typical radius for neutron stars of $R_{neutronstar} = 10^4$ m, rotational periods are in the order of milliseconds .

The magnetic flux through the former surface of the star is also conserved, increasing the field at the surface of the remnant to

$$B_{remnant} = B_{star} \cdot \frac{R^2_{star}}{R^2_{remnant}}, \tag{1.5}$$

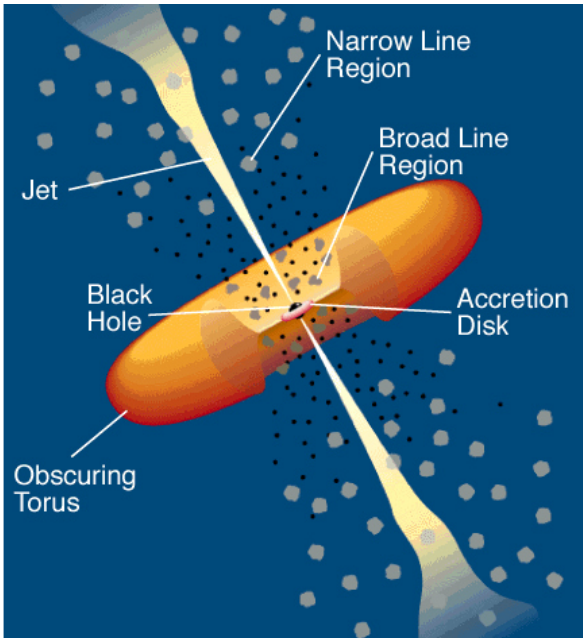

Figure 1.6: **Active Galactic Nucleus** [UP95] with central supermassive black hole, hot accretion disk possibly obscured by the larger dust torus in the same plane, relativistic jets and gas clouds capable of line emission.

so a stellar field of 0.1 T could increase to up to 10^9 T.

In the general case, the magnetic axis is not aligned with the rotational axis, which causes the periodic flux variations of a pulsar (see figure 1.5). The rotating field also creates an electric field $\overrightarrow{E} = \overrightarrow{v} \times \overrightarrow{B}$ that can accelerate charged particles. Mainly electrons and positrons created in pair cascades within the magnetosphere are expected to be emitted from pulsars. The observed radiation can be explained as synchrotron radiation from a leptonic source.

1.4.3 Extragalactic Sources: Active Galactic Nuclei

A large number of systems like the local galaxy known as the Milky Way can be observed. They usually contain a super-massive black hole with $\sim 10^6 - 10^{10}$ solar masses at the centre [RV07]. At least 5% of all galaxies show a small core of emission that is often brighter in the visual spectral range than the light of all the stars in the rest of the system together. They are called *Active Galaxies* and their luminous cores are known as *Active Galactic Nuclei* or AGN.

Special observed properties of AGN include high variability on relatively short timescales and mainly non-thermal emission over the entire electromagnetic spectrum from radio to γ-rays.

The current model to explain the emitted energy is the accretion of matter onto the central black hole. The energy gained from accretion of the mass m onto a black hole with mass M and the Schwarzschild radius $R_s = \frac{2GM}{c^2}$ is given by

$$\Delta E = \int_{\infty}^{R_s} \frac{GMm}{r^2} dr = \frac{GMm}{R_s} \sim 0.1\ mc^2 \tag{1.6}$$

This is extremely efficient compared to the thermal energy gained from fusion (about 0.7%)!

AGN are classified according to spectral differences, but many subclasses do not describe physically different objects, instead they are the same type of object seen from various viewing angles. Figure 1.6 illustrates the unified AGN model according to our current understanding. About 10% of all AGN are *radio-loud*. They form outflows of highly relativistic energetic particles approximately perpendicular to the accretion disk, which are called *jets*. These jets may contain shock fronts that are believed to generate the detected VHE emission. Objects of this class are historically also known as *quasars* (quasi-stellar radio objects). They are divided into *Fanaroff-Riley Galaxies* of type I and II (FR I and FR II respectively) according to the shape of the jets. The type FR I shows extended jets without distinct termination point and maximum intensity close to the core (core dominated), while FR II galaxies have narrow jets with maximum emission at the termination region (lobe dominated). In both cases, the jet pointed towards us may be much brighter than the other due to relativistic beaming. If the jet is pointed directly at us, the object is called blazar. All AGN observed in the VHE domain are blazars apart from M 87 and Cen A, which belong to the class FR I and are comparatively close.

When the jet is orientated close to the line of sight, the emission is Doppler boosted, yielding large fluxes and also large luminosity variations with relativistically shortened variability time-scales. The emission region appears smaller and VHE photons are able to escape the high radiation fields.

Populations of AGN may be used to study the intergalactic background photon field. On their way from the source to the Earth, gamma-rays may interact with photons of the IR background radiation producing e^+/e^- pairs. Therefore the observed spectrum softens with increasing distance. The H.E.S.S. collaboration has deduced a new limit on the extragalactic background light from spectral comparisons between AGN (see [Aha06b]).

1.4.4 The Galactic Centre region

The view to the centre of our own galaxy is obscured in visible light by dust. Still, the dust is transparent to light in other wavelengths, e.g. also to γ-rays. A TeV signal from the central region has been detected by [TEK04] and confirmed by [BV04],

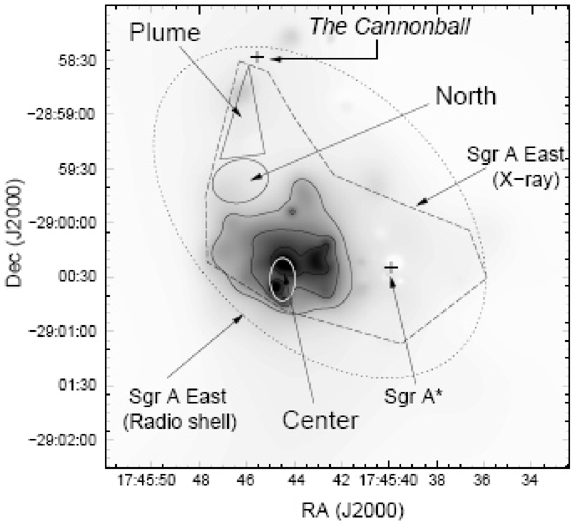

Figure 1.7: **Galactic Centre Region** [PMB05].

[Aha04c] and [AAA06]. From the multi-wavelength image, we know that several interesting candidates exist close to the dynamical centre that could be responsible for the emission:

- the accreting black hole **Sgr A***: the dynamical centre of our galaxy is a supermassive black hole with a mass of $2.6\times10^6\ M_\odot$ [SOG02].
- the supernova remnant **Sgr A East**: a relatively young (10^4 yr old) and unusually powerful (explosion energy 4×10^{52} erg) supernova remnant [MBF02].
- the pulsar candidate **G 359.95-0.04**: a newly detected object at a distance of only 4"-8" from Sgr A* could also be a plausible accelerator through Inverse Compton scattering [WLG06].
- **dark matter particles** may cluster around the gravitational centre of the galaxy and create γ-rays when they annihilate [BUB98].
- **curvature radiation** of protons near the black hole [Lev00].

To resolve the discrepancy between those possible interpretations, the accurate direction of the signal is a valuable piece of information, that can only be achieved with a good understanding of the used detector, in this case the H.E.S.S. experiment.

2 The H.E.S.S. Experiment

The High Energy Stereoscopic System (H.E.S.S.) is designed to study Gamma Rays using the Atmospheric Cherenkov Technique. It is sensitive to primary photons with energies ranging from 100 GeV to some 10 TeV.
This chapter will give details on Imaging Atmospheric Cherenkov Telescopes (IACTs) and the experimental setup of the H.E.S.S. telescope array as well as information on the data analysis.

2.1 Imaging Atmospheric Cherenkov Telescopes

Up to energies of a few GeV, gamma rays can be measured directly in satellite experiments. However, at higher energies the fluxes decrease considerably, making them exceedingly difficult to detect with the limited available detection areas of space-borne telescopes. The most successful approach to observe VHE photons is the Atmospheric Cherenkov Technique. Instead of trying to detect gamma rays directly, Cherenkov telescopes identify the electromagnetic cascade of secondary particles produced in the terrestrial atmosphere by the Cherenkov radiation of charged shower particles.

Gamma rays compete with a background of isotropically distributed charged cosmic rays that is stronger by a factor of at least ten thousand depending on the field of view of the instrument. Fortunately, it is possible to identify and reject most of this background based on differences in the development of the cascade and therefore its shape. Imaging Atmospheric Cherenkov Telescopes use pixelised cameras to resolve the shape of those cascades and extract additional information about the primary particle.

The first IACT experiment was the 10 m telescope of the Whipple observatory on Mt. Hopkins in southern Arizona, USA. It has been in operation since 1968. In 1989, the Whipple Collaboration detected the Crab nebula, a strong emitter of TeV radiation [WCF89]. This source became the standard candle in VHE γ-ray astronomy, because its steady flux allows one to compare results from different experiments and time periods.

In 1993, the HEGRA Collaboration [DHH97] used an array of Cherenkov telescopes to take advantage of stereoscopic observation, i.e. of imaging the shower from different perspectives. A coincidence trigger condition of detection in more than one telescope significantly reduced random triggers from night sky background and muons passing through a single telescope and enabled operation at a lower energy threshold. Also, the enhanced shower reconstruction allows both a better discrimination of the hadronic background by its less confined shower development and a significant improvement of the directional reconstruction. Measurements of the height of the shower maximum by triangulation improve the energy resolution.

Several imaging atmospheric Cherenkov gamma-ray telescopes are currently in operation around the globe:

- *The Whipple 10m Telescope* [WCF89]: the first experiment in this field now mainly monitors the variable emission of active galactic nuclei.
- *VERITAS* [HAB06] is the successor of Whipple and an array of currently four telescopes on the base of Mt. Hopkins.
- *MAGIC* [Fer05] is situated on La Palma and is at present the largest single dish γ-ray telescope. A second identical telescope will soon be completed next to the first to form a stereoscopic system. With a design energy threshold of about 50 GeV and a light-weight dish structure, MAGIC is optimized towards the observation of $\gamma - ray$ bursts.
- *CANGAROO* [Mor00] is an Australian-Japanese observatory located in Woomera, Australia. The current development phase CANGAROO III consists of four telescopes and has been completed in 2002.
- *The H.E.S.S. experiment* [Aha06e] is located in Namibia and the central component of this work. It is currently the most sensitive γ-ray telescope in the VHE regime. A detailed description can be found in chapter 2.2.

The geographically rather homogeneous distribution of Cherenkov telescopes has the advantage of providing the possibility to continuously monitor any source, as long as the moon does not impede telescope operation.

The image intensity is a measure of the energy of the primary particle. The resulting spectral information is vital for interpretations regarding the production and propagation of the detected γ-rays. Hence it is important to mention the physics of air showers in order to understand the Imaging Atmospheric Cherenkov Technique.

2.1.1 Extensive air showers

Particle avalanches induced by the entry of energetic particles into Earth's atmosphere are called *extensive air showers*. They can arise from all types of cosmic radiation carrying sufficient energy to produce additional particles by their interactions with air atoms and molecules. Characteristic length scales for air shower production are determined by the mean free path lengths of the processes involved. The radiation length $X_0 = 36.66\ \mathrm{g/cm^2}$ is the characteristic length scale for interactions of photons and

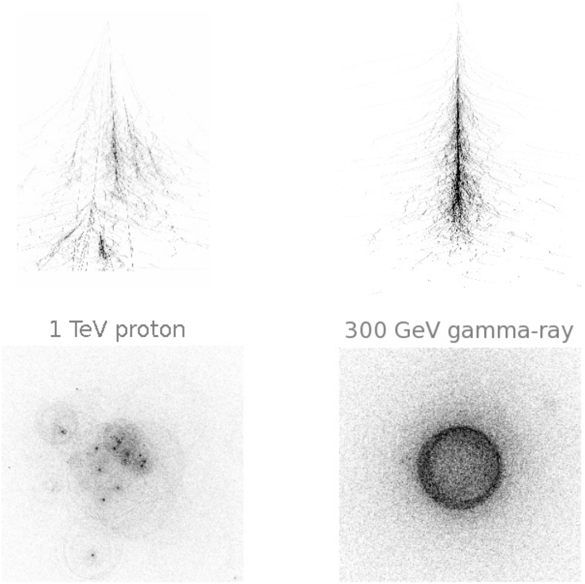

Figure 2.1: **Simulated air showers** of a proton carrying 1 TeV energy compared to a photon of 300 GeV primary energy. The upper images show the traces of individual shower particles in a lateral view, the two lower images show the distribution of Cherenkov light on the ground. The difference between the single Cherenkov cone of the γ-ray and the fragmented image of a hadronic shower is clearly visible.

electrons, yielding about 27 radiation lengths in the standard atmosphere. Hadronic processes can be described using the nuclear interaction length $\lambda = 90$ g/cm^2.

Extensive air showers contain three basic components: electromagnetic, muonic and hadronic sub-showers. In case of a photon or electron induced shower, only the electromagnetic component is present. Primary nuclei and protons, however, produce hadronic and muonic cascades in addition to electromagnetic sub-showers.

Air showers with different primary particles and energies can be modeled using Monte Carlo simulations. The showers seen in figure 2.1 were created with the simulation program *Corsika* [Hec01]. A large sample of such randomized air showers is usually used as a reference to deduce the properties of the primary particle from shower parameters.

2.1.1.1 Electromagnetic showers

Bremsstrahlung and pair-production form this component in an alternating sequence. Very energetic gamma rays interact with the Coulomb fields of air nuclei and may produce electron-positron pairs. The particles get deflected and produce new photons via Bremsstrahlung until ionization dominates the energy loss and the cascade stops at the critical electron energy of $E_{e^-} = 84\ MeV$. Up to this point, the number of particles increases exponentially with the amount of traversed material. The maximum number of particles is proportional to the energy of the primary particle, yielding a dependence of the length of the shower, and therefore of the atmospheric depth at the shower maximum that is proportional to the logarithm of the energy [Hei54].

Because pair production and Bremsstrahlung at relativistic energies emit the secondaries predominantly in the forward direction, electrons follow the shower axis without significant displacement (the lateral extent of the shower is given by the Molière radius of the secondary particles). A typical gamma ray carrying 1 TeV energy will create an electromagnetic shower starting at the first interaction height around (20-25) km and will reach the shower maximum with up to 10^3 particles at an atmospheric depth of 350 g/cm^2 or ~8 km above sea level.

2.1.1.2 Hadronic showers

The strong inelastic interaction processes of hadrons hitting air nuclei can produce new nucleons and mesons. These may scatter again and form the hadronic component, or decay into muons and neutrinos to feed the muonic component. Due to their higher momentum, muons suffer only negligible energy loss to Bremsstrahlung and are barely affected by Coulomb scattering. They also produce Cherenkov light, but the opening angle is smaller than for electrons and larger than the Colomb scattering angle. They decay with a relativistically prolonged lifetime into electrons and neutrinos.

Hadronic showers produce electromagnetic sub-showers in many interaction steps. Nucleon-nucleon collisions transfer transverse momenta to the secondary hadrons, yielding a much larger lateral distribution of particles than pure electromagnetic showers.

2.1.2 Cherenkov light

Only cosmic rays with energies starting on the order of 10^{15} eV produce secondary particles (apart from muons) able to reach the ground. Still, air showers with lower energies also leave detectable traces like Cherenkov light.

Most secondary particles in air showers still carry relativistic energies. Charged particles traversing a transparent medium with velocities exceeding the local phase velocity of light emit Cherenkov radiation. Since it is the fundamental effect allowing astronomy at TeV energies, a short review will be given following the arguments given in [Jel58] with a focus on the resulting requirements for Cherenkov telescopes.

The medium around a charged particle is polarized and returns to its normal state once the particle is removed. Normally, the distortion is isotropic, so no resulting field at large distances and therefore no radiation occurs. If however the particle is moving with velocities comparable to the speed of light in that medium, the polarization field

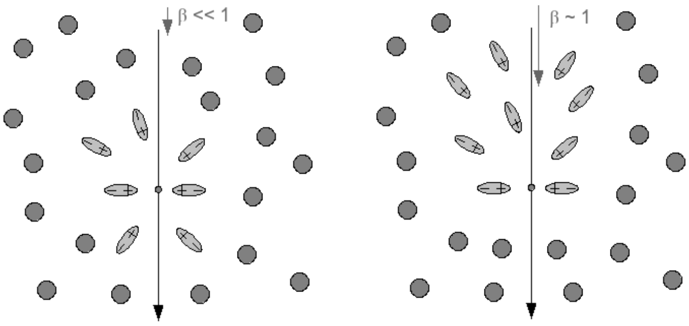

Figure 2.2: **Cherenkov emission** is caused by the asymmetric polarization of a medium (right) from a transversing relativistic particle.

is no longer symmetric to the direction of the particle. Along the path of a charged particle, the medium around each track element will radiate a short pulse of radiation, which will still interfere destructively in the general case, unless the particle is moving faster than the local phase velocity of light (see figure 2.2). This allows constructive interference on a plane similar to the acoustic shock wave of a Mach cone.
The emission angle relative to the particle direction is given by

$$\cos\theta_C = \frac{1}{\beta n}. \tag{2.1}$$

with refraction index n and the usual kinematic definition of $\beta = v/c$. From this it can be seen that no radiation is possible below a threshold velocity of $\beta_{min} = 1/n$, and that there is a maximum emission angle for ultra-relativistic particles ($\beta = 1$) of $\theta_{max} = \arccos(1/n)$.
The refraction index depends on the density, so it varies with atmospheric depth. Therefore the energy dependent height of the shower maximum yields an also energy dependent emission angle.
Assuming a density profile following the barometric formula, the refractive index can be calculated for a typical height at shower maximum around 10 km, leading to a light cone of about 1° opening angle and an illuminated area of approximately 120 m radius on the ground. A sufficiently sensitive telescope anywhere within this pool of light is able to detect the shower, yielding very large detection areas independent of the actual mirror area.

The spectrum of emitted Cherenkov light peaks in the UV, but due to absorption and scattering processes in the atmosphere, it arrives with dominant wavelengths around 300-350 nm (UV-blue), which experiences less attenuation. Smaller wavelengths are almost totally absorbed by fission of ozone molecules down to about 200 nm. The remaining photons suffer Mie- (λ similar to dimensions of target particles) or Rayleigh scattering (λ larger than targets), both of which are more effective at smaller wavelengths.

2.1.3 Detection of Atmospheric Cherenkov light

Cherenkov light is very faint, with a photon density in the order of 100 m^{-2} depending on the altitude of the observation and the site for a 1 TeV γ-ray. Therefore large mirror collection areas are required to project a sufficient amount of light onto a multi-pixel camera.

In addition, the flashes of light are extremely brief, only lasting for a few nanoseconds. Hence a very fast response time of the Camera is required to achieve an optimal signal to noise ratio.

For inclined showers additional geometric effects must be taken into account. As the formation of the shower depends mainly on the traversed atmospheric depth, light from showers detected at larger zenith angles has travelled a longer distance to the detector, thus a widening of the area illuminated by Cherenkov light and increase the effective area of the telescope system has occurred. On the other hand, the intensity of the image decreases because of additional scattering and absorption as well as the spread of the light over the larger cone.

The sensitive photo-multipliers needed to detect such faint flashes of light normally restrict observation time to moonless nights (with the exception of the MAGIC telescope which is operated in the presence of a thin crescent moon). The effective observation time per year is in the order of 1600 hours.

Thus, the Atmospheric Cherenkov Technique uses the atmosphere itself as detector medium. Shower imaging yields additional information about the primary particle, hence both an improved gamma-hadron separation resolution using shower shape parameters, as well as directional reconstruction become possible.

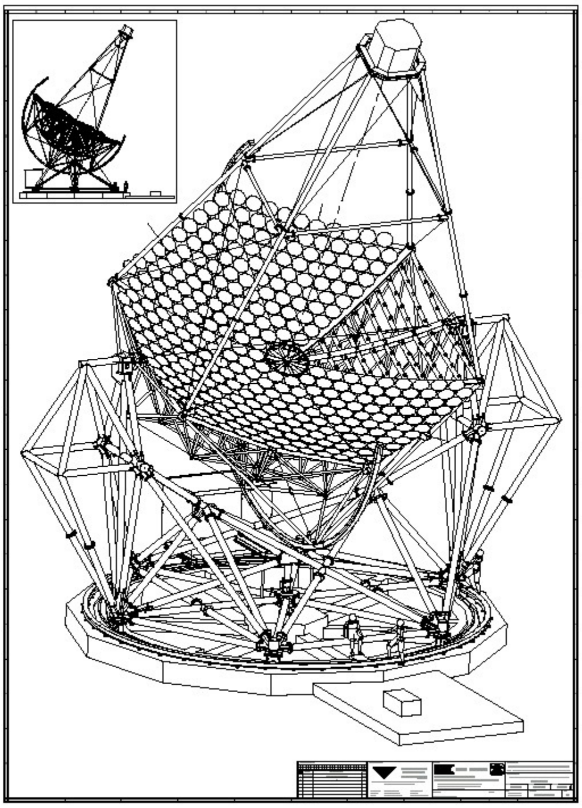

Figure 2.3: **Technical Drawing of a H.E.S.S. telescope**

2.2 The H.E.S.S. telescope system

The **H**igh **E**nergy **S**tereoscopic **S**ystem (H.E.S.S.) is an array of four Imaging Atmospheric Cherenkov telescopes located in the Khomas Highland of Namibia. Its name also honours the memory of Victor Hess, who discovered cosmic rays in 1912 (see chapter 1.2).

The array is located about 100 km south-west of the capital Windhoek at coordinates 16°30'00" East, 23°16'18" South and an altitude of 1800 m above sea level. The area is sparsely inhabited and known for its excellent conditions for astronomical observations [Wie98]. Its desert climate offers a large fraction of clear nights.

The southern hemisphere was chosen because the Galactic Centre culminates at zenith in the dry season, giving optimal observational possibilities for this target and other candidates in the inner galaxy.

The four 13-m-diameter telescopes are positioned in a square of 120 m side length, which is chosen to balance the need for wide spacing for stereoscopic reconstruction with a narrow spacing which yields a higher probability to have several telescopes within the same Cherenkov light cone. They are named CT1 though CT4, counting counter-clockwise with CT1 being the telescope furthest east. The oldest telescope is CT3.

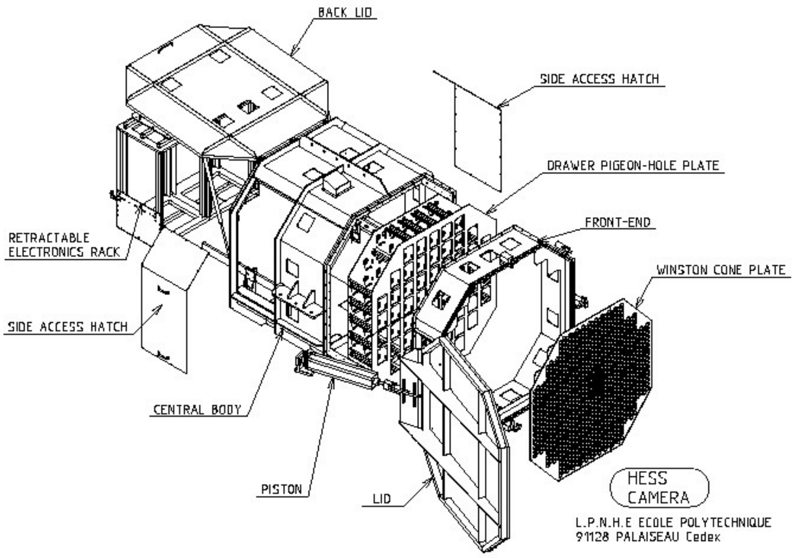

Figure 2.4: **Exploded view of a H.E.S.S. camera**

Each telescope mirror consists of 380 individual facets providing a total mirror area of 107 m^2 and a focal length of 15 m. They reflect light onto a Cherenkov Camera covering a large field of view of 5° and equipped with 960 photo-multipliers to image the shower. The angular resolution of H.E.S.S. for individual gamma rays is in the order of a few arc minutes, its energy resolution is better than 20% and its sensitivity allows the detection of a γ-ray source with 1% of the flux of the Crab Nebula at 5 σ significance in 25 hours of observations.

2.2.1 Mirror System and Camera

Having discussed the production of Cherenkov light in chapter 2.1.2, the focus of this chapter will be its detection using the H.E.S.S. telescopes.

To collect the Cherenkov light, 380 spherical mirror facets, each with a diameter of 60 cm, are mounted on a spherically shaped dish structure in a hexagonal arrangement. They are made of ground glass, aluminized and then coated with a protective layer of quartz. Mirrors and frame have the same focal length of 15 m. The general layout of such a segmented reflector is called Davies-Cotton design [DC57]. This design is very cost efficient and has a slightly better performance for off-axis photons than a parabolic layout. Differences in travelled path lengths yield a time dispersion of 5 ns between photons hitting the central part or periphery of the reflector. The RMS of the time differences is 1.4 ns, below the intrinsic spread in a Cherenkov wavefront. Details about the optical system can be found in [BCC03]. The connection between the facets and the dish is designed for remote motorized focal alignment [CGJ03].

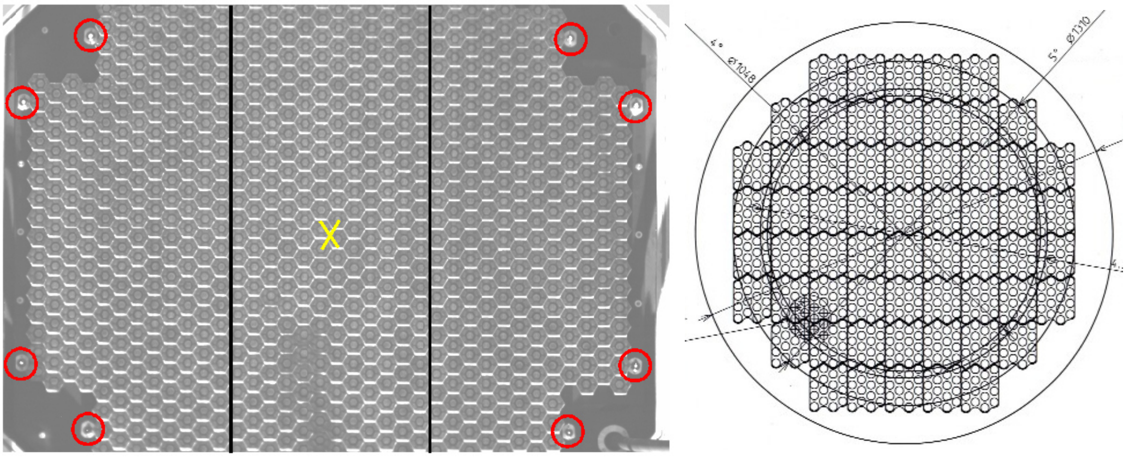

Figure 2.5: **Winston cone plate with positioning LEDs.** The left picture was taken in moonlight with the LidCCD. Red circles highlight the eight positioning LEDs, the two black lines mark the borders between the three funnel plate segments and a yellow cross is placed at the camera centre. The pixel matrix continues above and below the image forming the shape seen in the design study on the right, where the division into the 60 drawers is shown.

Spherical aberrations and additional deformations caused by gravitational pull, as well as misalignment of individual mirror facets, widen the apparent size of a point source in the focal plane (optical Point Spread Function or "oPSF"). Its value, which changes with altitude, is monitored regularly using star images. Since the initial alignment after the completion of the telescopes, the on-axis oPSF has never exceeded the design specification of 0.9 mrad.To measure the PSF, one has to take into account the difference between images of stars (perfectly parallel light) and those of showers coming from an altitude of about 8-12 km. This corresponds to a 3 cm difference in the focal planes and is corrected by placing the screen for star images closer to the mirrors by that amount. Conveniently, the lid protecting the photo multipliers of the Cherenkov camera from ambient light was designed as such a screen. A detailed study of the PSF can be found in [CGJ03].

The central detector of each H.E.S.S. telescope is the Cherenkov Camera (figure 2.4). It measures about 1.5 m × 1.5 m × 2 m and weighs approximately 800 kg. It includes all photon detectors and signal processing electronics needed, from programmable trigger electronics to data acquisition.
Light is detected by 960 Photonis XP2960 photo-multipliers (PMTs), that are organised in a modular design with 60 drawers of 16 PMTs each for simplified maintenance.

To collect all light in the focal plane onto the PMTs and reduce stray light with large incidence angles, Winston cone light concentrators (sometimes called "funnels") with hexagonal collection areas are mounted in front of the PMT entrance windows. The plates holding the Winston cones ("funnel plates") are built in three segments, each covering about one third of the PMTs. Next to the Winston cones, *positioning LEDs* mark the location of the camera. Figure 2.5 shows the hexagonal funnel structure, the LEDs and the division into three segments.

Each photo-multiplier signal is sent into in two separate amplification channels to increase the dynamic range of the detector. The *high-gain* channel shows a linear response between one and 200 photo electrons and is e.g. used for trigger decisions, while the *low-gain* channel operates between 15 and 1600 photo-electrons.

2.2.2 Trigger System and Data Acquisition

The high rate of cosmic rays requires a fast decision on the probability that an event is produced by a γ-ray to reject some of the background and avoid large dead times due to unnecessary camera readout. In H.E.S.S., this decision is made by a two-level trigger that combines the trigger information of multiple telescopes.

Trigger The trigger electronics for an individual telescope demand a minimum number of pixels within one of the 64 overlapping trigger sectors to exceed a threshold of a few photo-electrons within a time window of about ~ 1.3 ns to form a camera trigger. During the trigger decision time, the signal is stored in the analogue ring sampler and the trigger information sent to the *central trigger* [FHH04], where the decision to read out the data is made from multiple telescope coincidence requirements. If a given number of telescope triggers is received within a 80 ns coincidence window, the triggered cameras read out the ring buffer region corresponding to the original trigger time. This multi-telescope coincidence reduces triggers from fluctuations in the night sky background and local muons. Only multiple telescope coincidences start a full readout inducing dead time.

Data Acquisition The data are sent to a central data acquisition system controlling the different subsystems. Connected sets of data are combined in *"Runs"*. H.E.S.S. usually takes data in 28 minute periods, called *"Observation Runs"*. Different Run-types exist for calibration, tests and preparation of ObservationRuns.

Experiments with a smaller field have traditionally used an observation mode with *"On-"* and *"Off-Runs"*, where runs point directly at a presumed source and are followed or preceded by runs towards a background region. To cover the same range of zenith angles and comparable atmospheric conditions, Off-Runs are usually taken at the same declination as the On-Run, but with an offset in right-ascension corresponding to the time difference between the two runs.
Due to the large field of view of H.E.S.S., the measurement of cosmic rays in each ObservationRun uses a technique called *"Wobble-Mode"* observations. Instead of tracking a presumed source directly, pointing positions with certain offsets are chosen. Effects

due to the radially changing acceptance of the Camera can be avoided by choosing regions for background measurements that have the same distance from the Camera centre as the signal region. Wobble-Runs are usually performed to positions on each side of the source in Right Ascension and Declination. Typical offsets are 0.5 or 0.7°.

2.2.3 Data Analysis

Calibration Four general components can add to variations of the measurement: the camera, the optical system, the atmosphere and irregularities in the shower. Reproducible or measurable effects need to be corrected for before the analysis of gamma-ray sources may begin. The first step in data analysis is the calibration of photo-multiplier signals. Differences in High Voltage settings, responses to single photo-electrons, and dark currents in the PMTs are corrected for:

- pedestal: The position of the narrow dark-pedestal peak depends on the pixel temperature and needs to be recalculated frequently for each observation run. For each event, pixels that do not contain Cherenkov light according to the most recent pedestal measurement are included until enough statistics for an updated value is collected (about 1/min, depending on the trigger rate). The distribution may widen due to a background of starlight.

- response to single photo-electrons: the signal of each PMT varies strongly with the high voltage (HV) setting and is monitored using an LED pulser system in the camera shelter. The signal caused by single photo-electrons may be identified in the High Gain channel.

- ratio between signals in the High and Low gain channel: Cherenkov events in normal observations can be used to determine the average ratio between a signal in the two channels for the range where both are linear. The response for the Low Gain channel is then calculated from this ratio and the single photo-electron measurements of the High Gain channel.

- inter-calibration of the PMTs of one camera: a different LED system creates a uniform illumination of the whole camera providing flat-fielding information that corrects for different quantum efficiencies of the PMTs as well as different reflectivities of the Winston cones in front of each pixel.

- night sky background (NSB): the level of NSB light may be determined from the pedestal width or the PMT currents. The total current a pixel draws from the HV supply is used because of its large range and small dependence on the camera temperature (the same as used for the pointing tests described in chapter 3.4). Both methods agree very well [Aha04b].

These steps of data calibration are described in detail in [Aha04b].
After the correction of the camera response, optical effects like shading from the camera

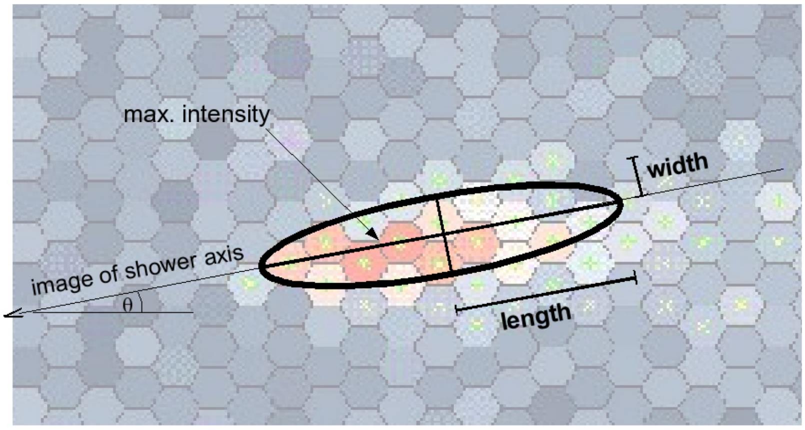

Figure 2.6: **Definition of Hillas Parameters**

support structure or the decreasing reflectivity of the mirrors and an overall degradation of the Winston cones can be measured using the Cherenkov light of single muons hitting or passing close to the telescope. [Bol04] gives details on this method of absolute calibration.

Reconstruction Runs performed in unstable conditions are rejected and the camera images are "cleaned" from fluctuations not related to the shower using a cut in favour of connected signal regions. The standard choice is a *5-10 tail-cut*, meaning that only pixels with a minimum of five photo-electrons are kept, when they have at least one neighbouring PMT that counted at least ten photo-electrons and vice-versa.

For the analysis of Cherenkov images, a technique using *Hillas parameters* [Hil85] has proven successful [CFG89]. For this approach, the roughly elliptical shower images are parametrized by their first and second moments, i.e. the centre of gravity and the two axes (Hillas parameters *width* and *length* as in figure 2.6) and orientation (θ) of an approximated ellipse. The intensity of the image (Hillas parameter *size*) is a first-order measure for the primary energy, the relation between length and width allows gamma-hadron separation, and the shower geometry can be determined from the parameters θ and the centre of gravity in stereoscopic systems.
A detailed description of the analysis is published in [Aha06e]

The stereoscopic technique allows a simple and efficient way to determine the arrival direction of a shower. For each shower image, the origin of the event is located along the major axis of the Hillas ellipse. The intersection point of the major axes of images from two different cameras determines the origin of the shower. Since the direction reconstruction is of special interest for this work, an improved method described in [HJK99], that is implemented for H.E.S.S. will be discussed in more detail in chapter 6.1.2.

2.2.4 Atmospheric Monitoring

Since the actual detector medium for atmospheric Cherenkov telescopes is the atmosphere, strong fluctuations in the trigger rate of cosmic rays can be caused by uncontrollable changes in the atmospheric condition. Hence continuous monitoring of atmospheric parameters is desired. The H.E.S.S. Experiment includes several weather stations, which are recording data on the environmental / air temperature, pressure and humidity, and also detect the presence of clouds and the transparency of the atmosphere [Bro05]. It should be noted that the transmissiometer setup includes clearly visible LEDs in a distance of 29.8 km[1] from the site, which are attached to the telecommunication mast on the Gamsberg and can be used as a target for maintenance work on the SkyCCDs.

2.2.5 Drive System and Guiding

Imaging Cherenkov telescopes observe only a limited area of the sky, hence it is necessary to point the detector in the desired direction and follow the source during observation time. To ensure this motion, each telescope is supported by a sturdy steel structure that is mounted in a rotating frame on a circular rail with 13.6 m diameter, allowing horizontal movement. The clock-wise angle between north and the telescope direction is called *azimuth*. Mirrors and Camera are attached to a dish structure rotating in an angle perpendicular to the horizon called *elevation* or *altitude*. The complementary angle to 90° is called zenith angle. An alt/az mount is favourable for the stability of heavy telescopes which in this case weighs about 60 t.

Friction wheels drive the telescopes in altitude and azimuth with a slewing speed of up to $100°/min$. To achieve accurate tracking, the current position is monitored with 17 bit shaft encoders returning the absolute position with a digital step size of 10" (Grey code) and analogue verniers for a finer relative resolution. In each initialization of the tracking system, the absolute position is read out with 10" precision. This introduced offset remains constant for the rest of the operation, allowing to follow a source with arc-second-precision. Further details can be found in [Bol04].

2.2.5.1 Guiding System

Due to the large field of view of the H.E.S.S. camera, it is not vital to point exactly at the desired position during the observation, but sufficient to record the orientation for off-line analysis. The actual orientation of the telescope can be measured with a system of two CCDs installed on each telescope, one in the centre of the dish, on the so called *central hub*, the other 3 m to one side, so its field of view is not obscured by the Cherenkov camera or masts. These cameras are called the LidCCD and the SkyCCD

---

[1] GPS coordinates: -23.34° S / 16.232° E, height: approx. 2356m asl.

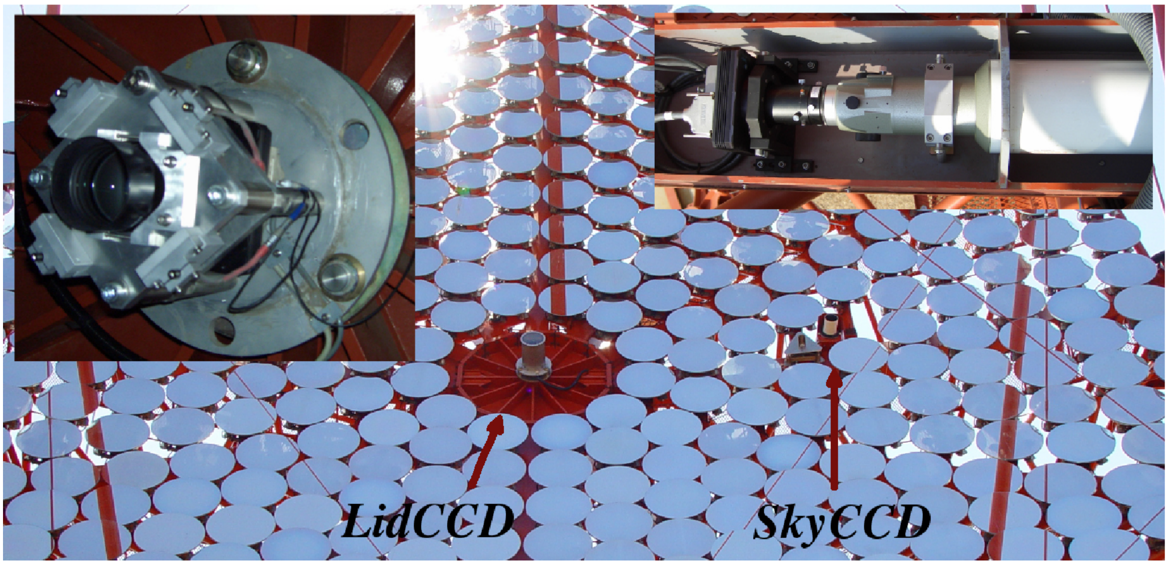

Figure 2.7: **Image of the CCD cameras** showing the dish of the telescope CT3 with the SkyCCD to the right and the LidCCD on the left. The picture is overlaid with close-ups of the two cameras with opened casing.

respectively, and technical details are listed in table 2.1. Both CCDs are cooled by Peltier elements keeping a constant temperature difference to the environment

SkyCCD With an 800 mm focal length, the SkyCCD easily qualifies as a small telescope. It is used as guiding telescope and is mounted to the dish of the Cherenkov telescope in parallel to the nominal pointing direction. Using the SkyCCD, it is possible to determine the unknown 10" offset of the shaft encoders, or, more generally, to connect the actual pointing direction at the time of a SkyCCD image to the telescope structure.

	Apogee Ap1E, SkyCCD	Apogee Ap2Ep, LidCCD
Chip	KAF-400E	KAF-1600E
number of pixels	768 × 512	1536 × 1024
f.o.v	$0.51^\circ \times 0.33^\circ$	$5.8^\circ \times 3.9^\circ$
resolution	2.3"/pix	13.7"/pix
pixel size, capacity	9 μm, 85.000 ph.e.	9 μm, 100.000 ph.e.
lens	Vixen NA120S	Nikon Nikkor
lens specifications	800 mm, 6.7	135 mm, 2.0
fullframe readout	$\sim$ 1 s	$\sim$ 50 s

Table 2.1: **Technical details about the CCD Cameras of the H.E.S.S. Experiment.**

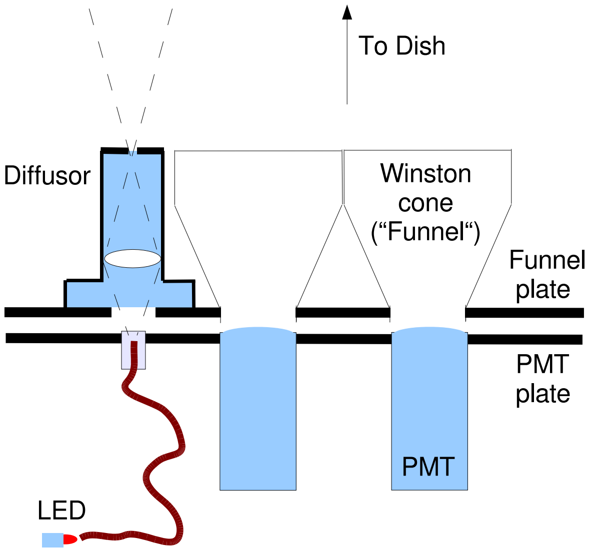

Figure 2.8: **Funnels and Diffusor**.

LidCCD The LidCCD is used for two basic applications:

- *mirror alignment and monitoring of the Point Spread Function:* the process of mirror alignment is described in [CGJ03]. Images of stars on the lid can be used to continuously monitor the optical quality of the reflector.
- *pointing applications* including the creation of pointing models, monitoring of mast and dish bending and the imaging of the funnel edges. These applications will be discussed in chapter 3.

The LidCCDs are firmly attached to the central hub in a steel casing, holding the camera housing as well as the lens. It is designed to observe the camera body and stars on the camera lid. The lenses were changed in late 2004 from 180 mm to 135 mm focal length. The field of view with the newer lenses ($5.8^\circ \times 3.9^\circ$) includes all eight Positioning LEDs, while the old setup showed only two or three LEDs and the central region where the reflected image of a well tracked star should appear. The original higher magnification was of advantage for the initial mirror alignment, however the larger field of view is beneficial for pointing corrections.
The readout time of a full-frame image is in the order of 50 seconds, but faster readout of smaller sub-frames is also possible.

Positioning LEDs Each LidCCD observes eight red positioning LEDs next to the Winston cones. The light sources are located within the camera and the light is guided in glass fibers to the desired positions on the plate holding the PMTs (see figure 2.8). On the funnel plates, the light is collected and focused on a 0.7 mm hole in the same plane as the funnel entrances using so called "diffusors". This construction allows to have a purely optical connection between main camera and funnel plate, and still allows to locate the Winston cone entrance positions. Holes in the camera lid can be opened to observe these spots without exposing the camera to ambient light.

3 Standard Pointing

Astronomical observations are insubstantial without the ability to relate the measured results to a direction in the sky. The reproducibility of this pointing direction is important for all telescopes, especially those needing long exposure times. Optical astronomers often use bright stars of known position within the field of view to identify the observation position. Basing the pointing on known, strong reference emitters is, however, not possible for experiments pioneering and advancing a field like the H.E.S.S. telescope system, thus alternative methods become necessary. Due to the large size of the telescopes, achieving high pointing accuracy is not trivial. This chapter will introduce the standard techniques used to determine the precise orientation of H.E.S.S. relative to its observed targets.

The final goal of accurate pointing for H.E.S.S. is to relate the direction of showers in the Cherenkov Camera to the origin of the primary γ-ray in the sky. This includes three main steps:

1. transformation of inherent coordinates (e.g. RA/Dec) to apparent ones (Alt/Az). The implementation of this step for H.E.S.S. is described in [Gil04]. It will be reviewed in section 3.1.
2. application of modifications caused by local atmospheric conditions (i.e. refraction). A short discussion can be found in section 3.1.
3. understanding the behaviour of the detector. This involves inaccuracies of the tracking and timing system, mechanical deformations of all components and optical properties of the reflector, but also realistic assumptions about the errors induced by the analysis method and software. Due to this large variety of effects, this step is the main focus of the technical part of this work and will be addressed throughout this and the next two chapters.

In H.E.S.S., the pointing is derived from calibration runs (pointing runs), where the telescope is aligned directly towards a star. The star is reflected on the mirrors and its image appears on the camera lid covering the PMT entrances. The centre of gravity of the image marks the actual observation direction for stars (shower images might differ slightly due to different refraction) and is compared to the centre of the camera, which is the assumed observation direction of an ideally pointed telescope. The difference is recorded for various telescope orientations and fitted to a model. Under the assumption that pointing deviations are reproducible, caused e.g. by elastic deformations of the telescope structure, the model can be applied to regular observations.

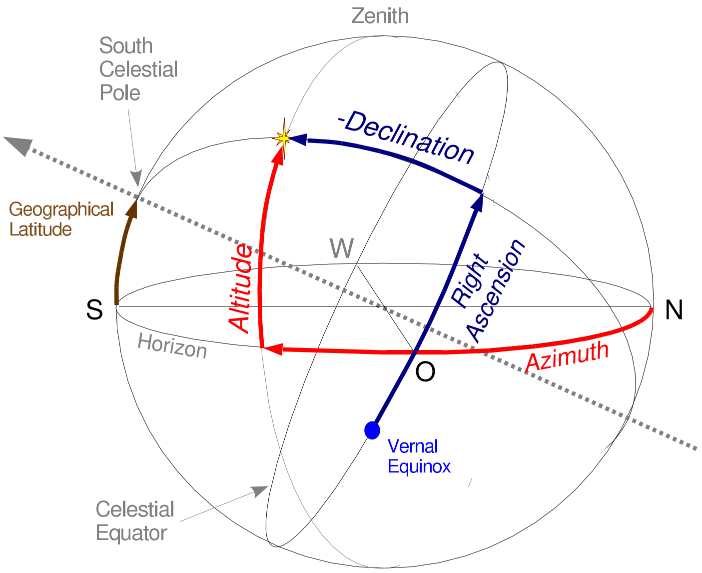

Figure 3.1: **Visualization of RA-Dec (blue) and Alt-Az (red) coordinate systems:** a celestial coordinate may be described by its angular distance from northern direction along the equator (azimuth) and its angular height above the horizon (altitude), or by its distance from the point of vernal equinox on the celestial equator (right ascension) and its height above the celestial equator (declination).

The chosen parametrisation is the *Mechanical Model* [PDH97], its implementation in H.E.S.S. is described in [Gil04]. [Gil04] showed that the intrinsic accuracy of this method can be as good as 10”, but also found indication for additional systematic errors using independent tests.

This work investigates possible systematic errors in detail (see chapter 4) and presents a new pointing approach in chapter 5. But initially, the standard pointing in H.E.S.S. is introduced to offer a better understanding of the following research.

3.1 From the Sky to the Ground

Astronomical Coordinate Transformations

Most astronomical coordinate systems are defined by two angular coordinates that are perpendicular to each other and some reference plane passing through the observer. One of the coordinates usually runs from $-90°$ to $+90°$ and denotes the distance from that reference plane while the other runs from $0°$ to $360°$ and marks the orientation on that plane, so that they are defined in a similar manner to latitude and longitude on the surface of the Earth.

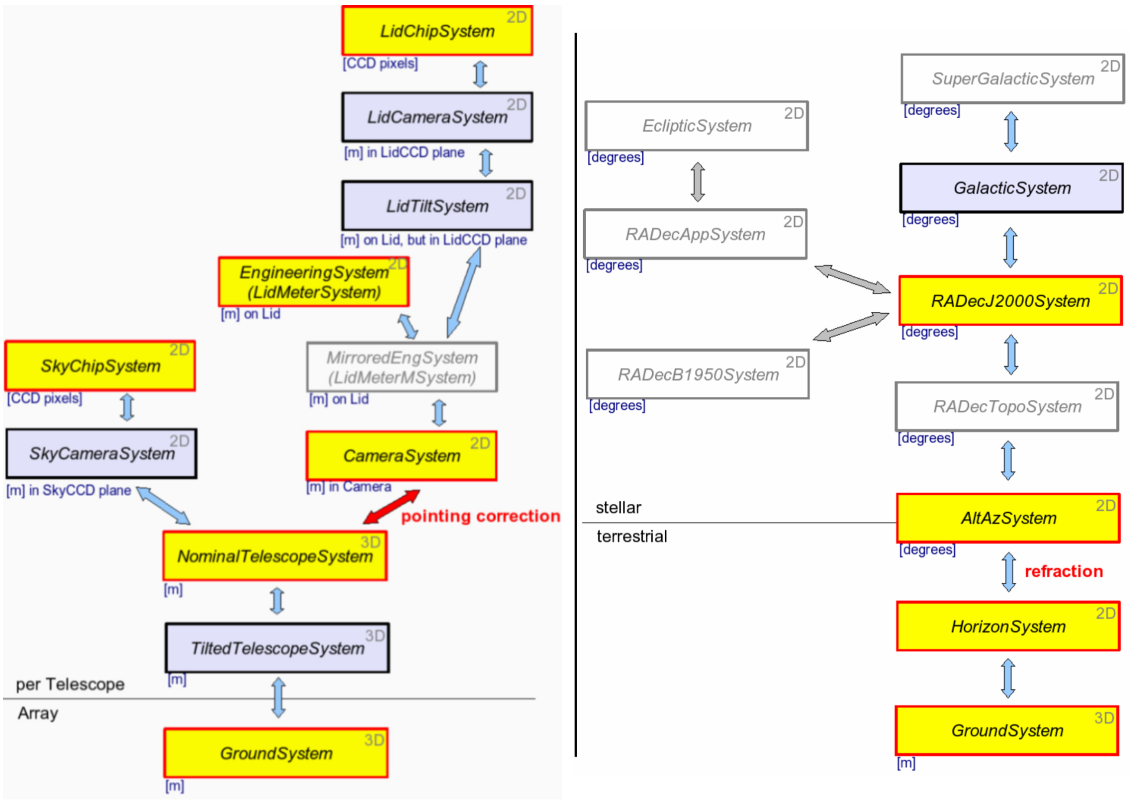

Figure 3.2: **Coordinate tree** including the various systems used in H.E.S.S. to connect spot coordinates in the CCD cameras to the Telescope and from there to celestial systems. System names refer to the implementation in the H.E.S.S. software. The left side of the figure shows the coordinate systems used to describe the telescope, while the right side depicts different ways of describing telescope orientations and celestial coordinates. The two trees are connected through the GroundSystem. Yellow systems are discussed within this work, while faint grey systems are used rarely.

Star coordinates are usually given in *Right Ascension (RA)* and *Declination (Dec)*. The RA-Dec or *Equatorial* coordinate system is based on the celestial equator and the celestial poles (see figure 3.1). The Declination of an object is its angular distance from the celestial equator, ranges from 0° at the celestial equator to 90° at the celestial poles and is taken to be positive when north of the celestial equator and negative when south. The Right Ascension is defined relative to a celestial reference point: the vernal equinox or first point of Aries (one of the crossing points of ecliptic and celestial equator) going counterclockwise. The slow precession of Earth's rotational axis leads to the necessity to specify the time at which this reference point was fixed. The current epoch is called J2000 and was fixed at January 1st 2000. Of course, the direction of a given RA-Dec coordinate on the observed sky changes with time, therefore it is not very practical for the description of telescope orientations.

The most intuitive coordinate system is the *HorizonSystem*. It is based on the tangent plane of the Earth passing through the observer. The angle measured vertical from the horizon to an object determines the *Elevation* of that object. It lies in the range from $-90°$ to $+90°$, with values greater than zero for objects above and negative values for objects below the horizon. The second angle called *Azimuth (Az)* spans 360° running clockwise and starting from 0° in northern direction. The apparent height of a star at a given time is also affected by refraction, which is taken into account in the *AltAzSystem*. The *Altitude (Alt)* for a given Elevation can be calculated with the knowledge of the appropriate refraction correction (see chapter 3.1), the Azimuth remains the same as in the HorizonSystem.

A chain of coordinate transformations (see figure 3.2) connects each system with the others, sometimes through intermediate systems to obtain a more general implementation. The systems group into five basic classes according to the transformations needed to connect the system to the rest of the tree. These transformations are implemented within the system and are either a combination of shift, rotation and scaling, a change in orientation, the projection of a 3-dimensional system onto a 2-dimensional system, the mirroring of one coordinate, or a relative tilting between two planes.

Atmospheric Refraction Correction

The first correction applied for accurate telescope pointing is the refraction correction. The distance of a star from the horizon appears larger due to the bending of light on layers of increasing refractive index within the atmosphere. Due to the relation

$$\sin(\theta_2) = \frac{n_1}{n_2} \cdot \sin(\theta_1) \tag{3.1}$$

between the angles $\theta_{1,2}$ relative to the surface normal and the refractive indices $n_{1,2}$ for two adjacent layers indicated with indices 1 and 2, the atmospheric refraction is strongest for incident light at large zenith angles. The necessary altitude correction may reach the order of 2' for $60 - 70°$ zenith angle and depends on the composition of the atmosphere and the wavelength of the light (see figure 3.3). Extensive air showers are created lower in the atmosphere, which is taken into account applying a *reduction factor* r to the correction given by

$$r = 1 - e^{-(h_{shower}(alt) - h_{location})/(8600\ m)}. \tag{3.2}$$

An important detail for H.E.S.S. is that showers emit blue Cherenkov light, so the effects might differ from the results for starlight, especially when showers are compared to stars detected by the primarily red-sensitive CCD cameras.

Several models exist to calculate the effects of refraction on star light of different wavelengths. The two models implemented in the H.E.S.S. Software are based on the Astronomical Almanac [Nau92] (referred to as *"exact"* model and *"approximate"*

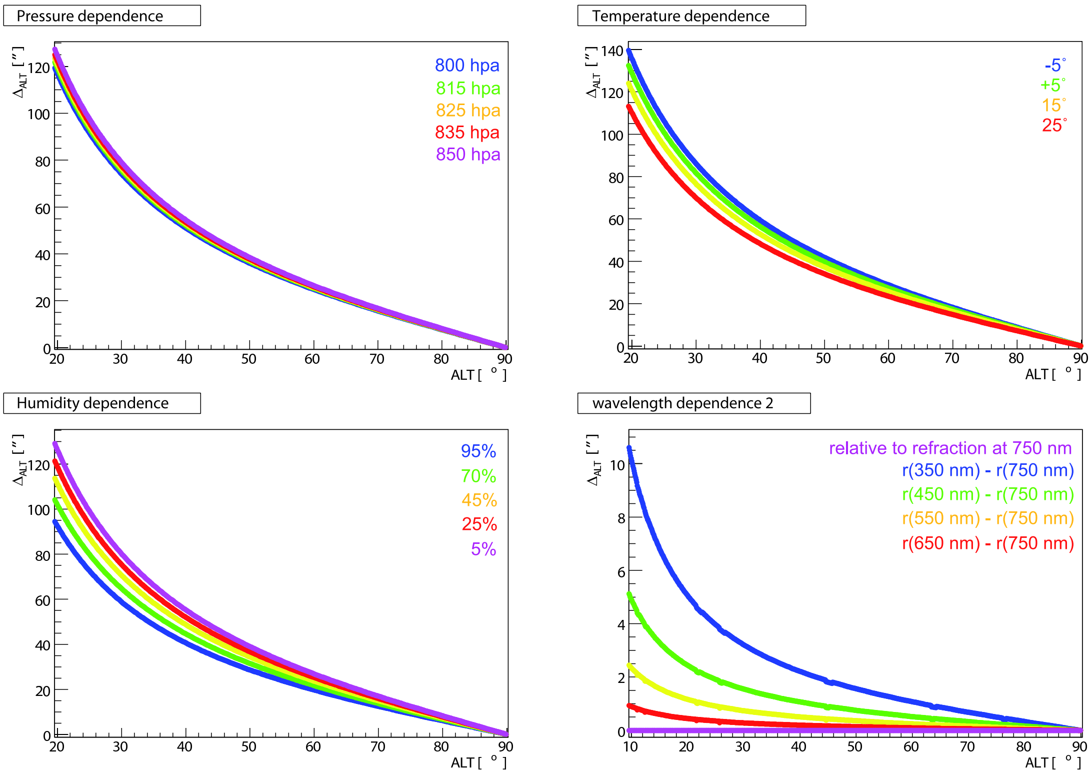

Figure 3.3: **Atmospheric Refraction:** comparison of different atmospheric conditions and for different visual wavelengths. The range of parameters was chosen to mirror the range of weather conditions measured so far at the H.E.S.S. site. The refraction correction using the "exact" formula is plotted as a function of altitude varying one involved parameter at a time, keeping the other parameters at defaults values (15°C, 825 mbar, 20% humidity and 450 nm wavelength).

model). They depend on varying atmospheric parameters like ground pressure, temperature and humidity that can be measured with the weather station on the H.E.S.S. site, but also need assumptions about the atmospheric pressure profile. The correction was calculated for different atmospheric conditions and wavelengths and is shown in figure 3.3 using the "exact" model. The main differences for different parameter values are observed for low altitudes, where typically no observations with critical pointing questions are performed. A comparison of those models and an additional parametrisation proposed by [Yan98] yields less then 5” difference in refraction above 45° altitude.

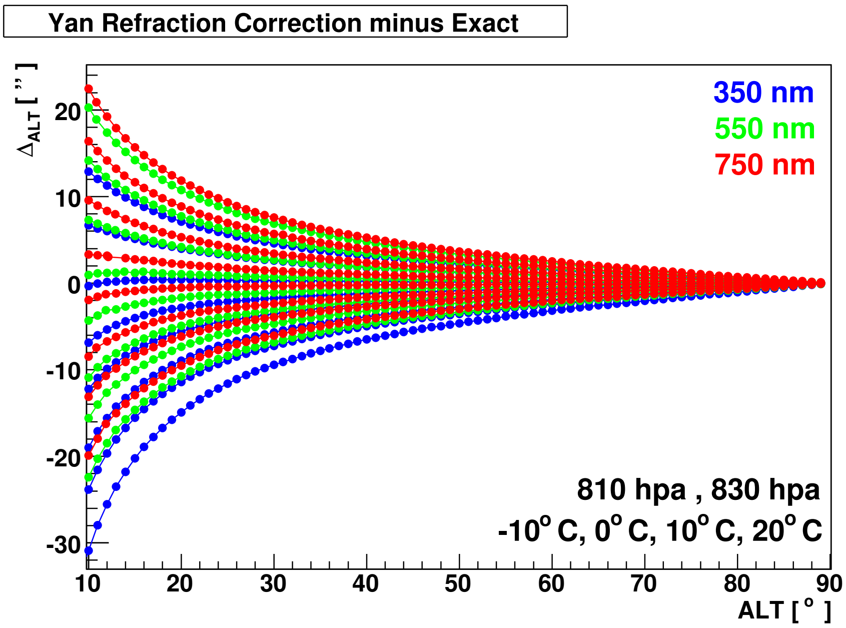

Figure 3.4: **Refraction model comparison.** The difference between two competing refraction models is plotted vs. altitude for various colours, pressures and temperatures.

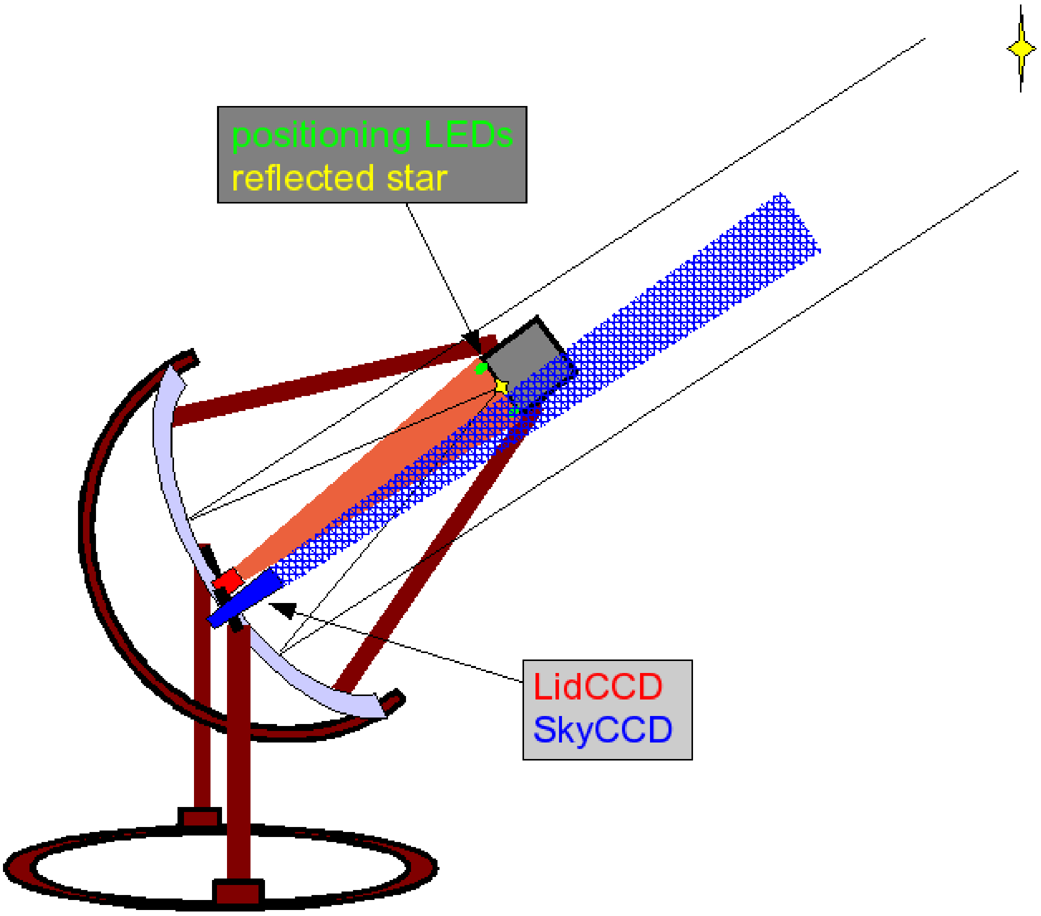

Figure 3.5: **Pointing: basic principle.** The figure shows the relevant pointing components of a H.E.S.S. telescope. The field of view of the SkyCCD (blue) passes next to the Cherenkov camera and observes the sky directly, while the reflection of stars on the Lid is recorded using the LidCCD (light red). The LidCCD also measures the position of the Cherenkov camera with the help of positioning LEDs (green) fixed to the Winston cone plate.

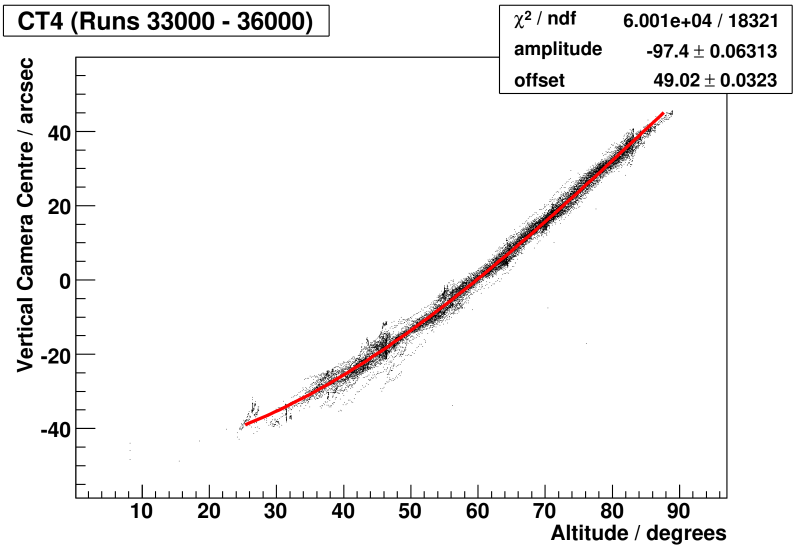

Figure 3.6: **Mast bending** illustrated on the example of CT 4. The plot shows the vertical camera centre determined from the fitted LED spots from LidCCD images in arc-seconds relative to an arbitrary offset. Each point corresponds to one LidCCD fullframe image containing at least seven LED spots. Pointing and observation runs from June to November 2006 are included. The data points between 30 and 88° altitude were fitted to a cosine function (red line) describing the data well, the residuals to this function spread with an RMS in the order of 2".

3.2 H.E.S.S. Standard Pointing

As mentioned in the introduction to this chapter, the pointing deviation is determined from the difference of the position of a star imaged on the camera lid and the camera centre measured with the positioning LEDs in reference runs. The technical realization of this measurement is done using the LidCCD. From the difference in CCD pixels (LidChipSystem in figure 3.2), one can deduce the mispointing on the sky knowing the focal length and pixel size.

A pointing run involves the tracking of a star, ten images from the SkyCCD, one image of the reflected star in the central region of the lid with the LidCCD, and one image showing the eight positioning LEDs, again with the LidCCD. The exposure time for images of stars is adapted to the star's nominal magnitude. In addition, meteorological information is stored to apply the refraction correction and correct for other effects caused by different temperatures (this is so far only done for the precision pointing described in chapter 5). All components contributing to the pointing of the H.E.S.S. telescopes are summarized in the illustration 3.5.

The mispointing depends on the orientation of the telescope, therefore it is necessary to use many measurements in different directions of the sky. The targets are scheduled

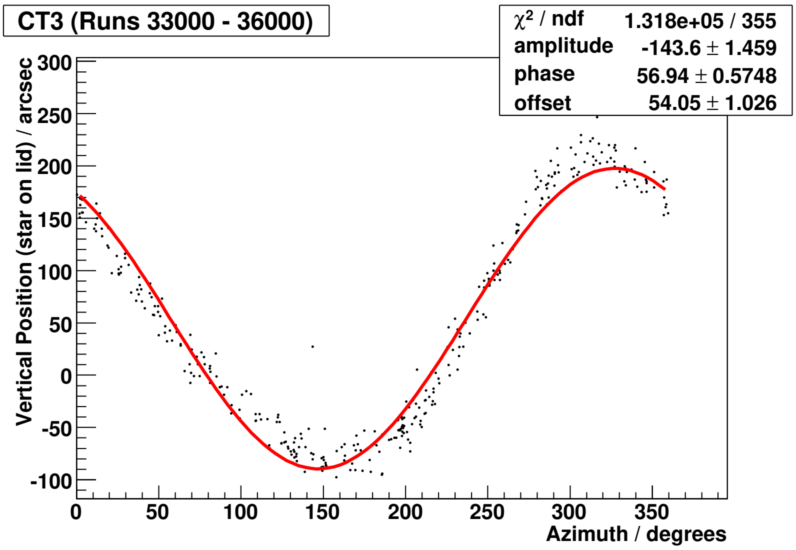

Figure 3.7: **Azimuth dependence on vertical star position on the lid.** The vertical position of the central star on the lid is transformed into arc-seconds (arbitrary offset subtracted) and corrected for refraction. When this value is plotted as a function of azimuth, a roughly sinusoidal dependence can be seen (red curve), indicating a tilt of the azimuth axis. The plot shows this effect for CT3, where it is largest. The data set includes pointing runs taken between June and November 2006.

automatically from stars of the Hipparcos catalogue in order to achieve a uniform coverage of the azimuth-altitude plane. The coverage is not homogeneous on angular scales, because the changes depend on the telescope structure and therefore the mount (imagine two "bumps" on the azimuth rail; the distance between them will not change for higher altitude observations, even though the angular distance decreases). Pointing runs are performed in regular intervals to account for possible changes in the telescope structure or CCD cameras. Astronomical darkness is not required, so the sets are typically produced at the beginning and end of each dark period while the moon is above the horizon.

The total set of mispointing corrections is approximated by a function accounting for mechanical tilts, shifts and rotations of the telescope structure, and amplitudes and phases of periodic errors. Parameters of the mechanical model worth mentioning separately are

- global camera offsets and camera rotation,
- the bending of the camera support masts under the influence of gravity following

$$\Delta alt \sim \cos(alt). \tag{3.3}$$

  Figure 3.6 shows an example of the vertical position of the reconstructed camera centre as a function of telescope altitude to visualise the effect. The fitted cosine

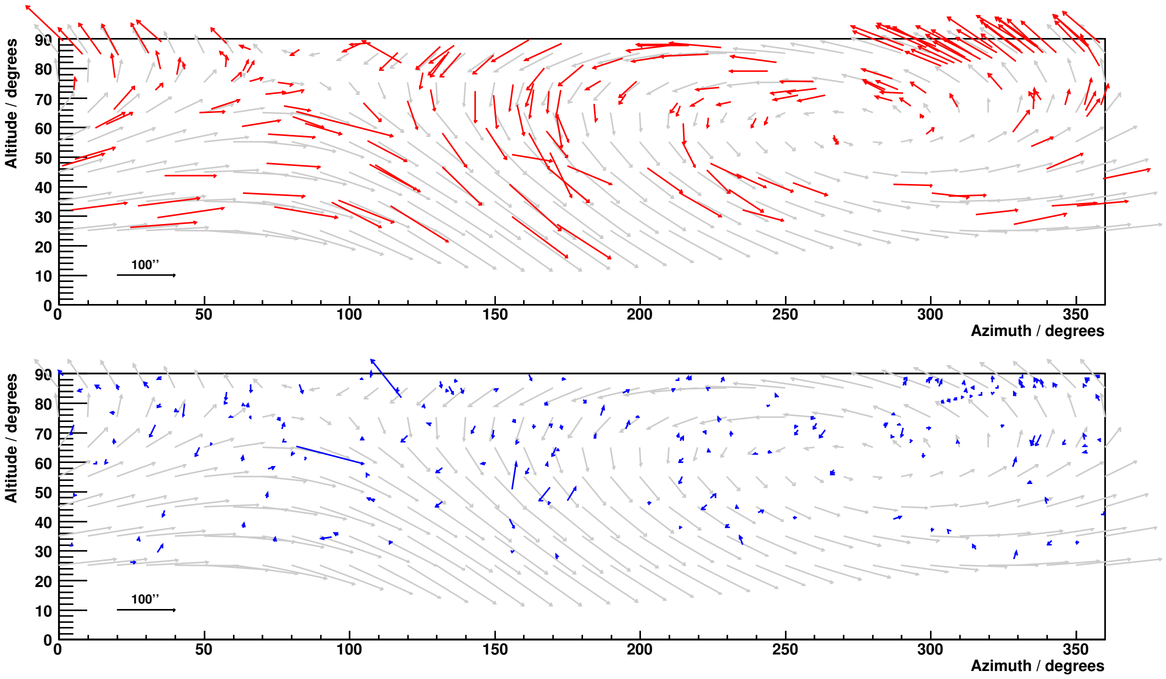

Figure 3.8: **Pointing model** for CT2 valid during July 2005. Red arrows show the 193 individual corrections contributing to the model, grey arrows indicate the fitted pointing model. The arrows are magnified with respect to the Alt-Az grid by a factor of 720 (1° corresponds to 5”). In the lower plot, the blue arrows represent the residuals of each pointing run. The residual width is 9.6” and 10.4” for altitude and azimuth corrections, respectively.

dependence describes the data well, the residuals to this function spread with an RMS in the order of 2”.

- tilts of the altitude and azimuth axis that can be seen in the position dependence of the image of tracked stars on the lid. An example is given in image 3.7.

The model is then applied to Cherenkov data as a shift in the focal plane (rotation and enlargement is practically constant) depending on the telescope orientation in azimuth and altitude. A visualisation of a typical model is shown in figure 3.8.

A second independent mechanical model is produced for the SkyCCD. All parameters except the bending term are in the same order of magnitude. This model will be important for the precision pointing described in chapter 5.

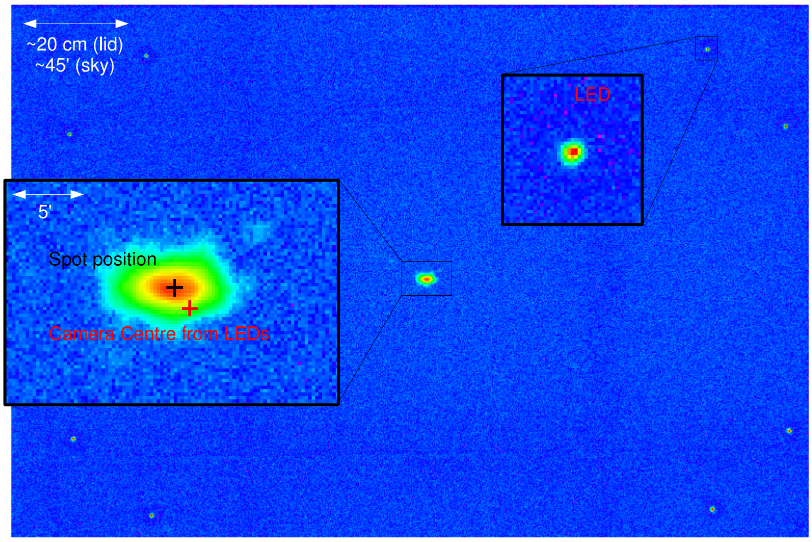

Figure 3.9: **LidCCD image** of a pointing run on Arcturus in logarithmic colour scale. The eight LEDs and the central star are clearly visible. The image is overlaid with a zoom into the region of the central star showing the positions of the spot (black cross) and the camera centre deduced from the LEDs (red cross).

3.3 Image Processing

Figure 3.9 shows an image of the lid taken during a pointing run with CT2 including the eight positioning LEDs and the reflection of the central star. The inlay shows a comparison of the positions determined from star and LEDs, hence visualises the pointing correction. In this section, the derivation of those two positions within the image will be explained.

3.3.1 Spot Extraction from CCD Images

To gain the desired correction, the CCD images have to be processed into a list of spots contained in the image. This is done in a two-step procedure with the help of the eclipse library [Dev01] developed by the ESO (European Southern Observatory). In the first step, objects in an image are identified according to the following procedure: a 3x3 pixel median filter removes outlier pixels. Then the median pixel value (i.e. the threshold containing half of the pixel intensities) is computed. Under the assumption that the image consists mostly of background, this value is a bit larger than the average background intensity. A binary map of signal pixels (getting the value 1) with an intensity greater than this value plus a previously chosen threshold offset is created and smoothed using the median filter. The remaining connected signal regions are then individually analysed with standard eclipse procedures.

In the second step, a more accurate spot extraction method is used in sub-frames of 20 x 20 Pixels around each major object's position. The algorithm removes outlier pixels using the same median filter as before and applies a segmentation method to identify one single spot on a possibly non-constant background. After background subtraction, a cut additionally removes weak spot regions (tails) with less than 1/4 of the maximum spot intensity (reduced by the median filter). Finally, the centre of gravity of the remaining image is returned as the position of the spot.

More details can be found in [Gil99] and [Dev01]. The uncertainty of this spot extraction method is part of the systematic error of the pointing and will be discussed in section 4.2.2.1.

3.3.2 Determination of the Camera Centre

The spots identified as stemming from one of the eight positioning LEDs are passed to a Minuit [JR75] based fitting algorithm. The physical positions of the corresponding LEDs (*EngineeringSystem* in diagram 3.2) are scaled, rotated and shifted to minimize the summed square distances between spot and expected position. This transformation marks the transition between *LidCameraSystem* and *LidTiltSystem* in diagram 3.2 and can be performed with a minimum of three identified LEDs. It is important to have as many LEDs as possible in the fit to reduce systematics. Due to a hardware problem, the procedure to turn on one LED is only successful in 97.3% of the cases. In average, 7.80 of the eight LEDs are turned on in pointing and observation runs. The systematic influence of missing LEDs is discussed in chapter 4.2.2.2.

3.4 Independent Monitoring of the Pointing using Camera Currents

Once a model is created, it is desired to test its correct application in an independent way. The most direct assessment of the connection between the sky and the Cherenkov camera can be made using the pixel "temperatures". Stars in the field of view induce DC currents in the photo-multipliers in addition to the brief flashes of air shower light. Due to the rotation of the sky and the Alt/Az mount of the telescope, the stars seem to travel on arcs around the centre of the camera with an angular velocity depending on the the change of the angle between polar axis, observation position and zenith (see [TG97]). This increase in photo-multiplier currents is recorded and can be traced back to the corresponding star.

Pixel currents are derotated and transformed to the RA/Dec plane using a standard pointing model as described in 3.2. The validity of that model can be tested on the consistency between known star positions and the projected pixel temperature fluctuations (see figure 3.10).

For each observation run and telescope, the derotated current maps are fitted around known star positions with an asymmetric function accounting for off-axis aberrations of the mirror support structure. The difference between the fitted position and the stellar coordinate is averaged for all successfully identified stars in the field of view and written to a database. The accuracy of this test is better than the size of a pixel due to field of view rotation, so the component perpendicular to the camera radius is determined most accurate (lower left in figure 3.10). The average deviation for all runs taken in 2006 is about 1' for CT3 and O(30") for the other telescopes. Still, the overall accuracy for a typical run does not exceed 5', therefore it is not a stringent test for pointing models, but still useful to detect errors like mistaken run parameters or larger timing offsets.

3.5 Conclusion

The mechanical model is based on the assumption of elasticity and does not account for time dependent effects. This introduces systematic errors. The image analysis is also a source of systematic errors like optical aberrations and errors due to the spot extraction. Since problems have been seen in [Gil04], the systematic influences of all those parameters were studied and will be discussed in the following chapter.

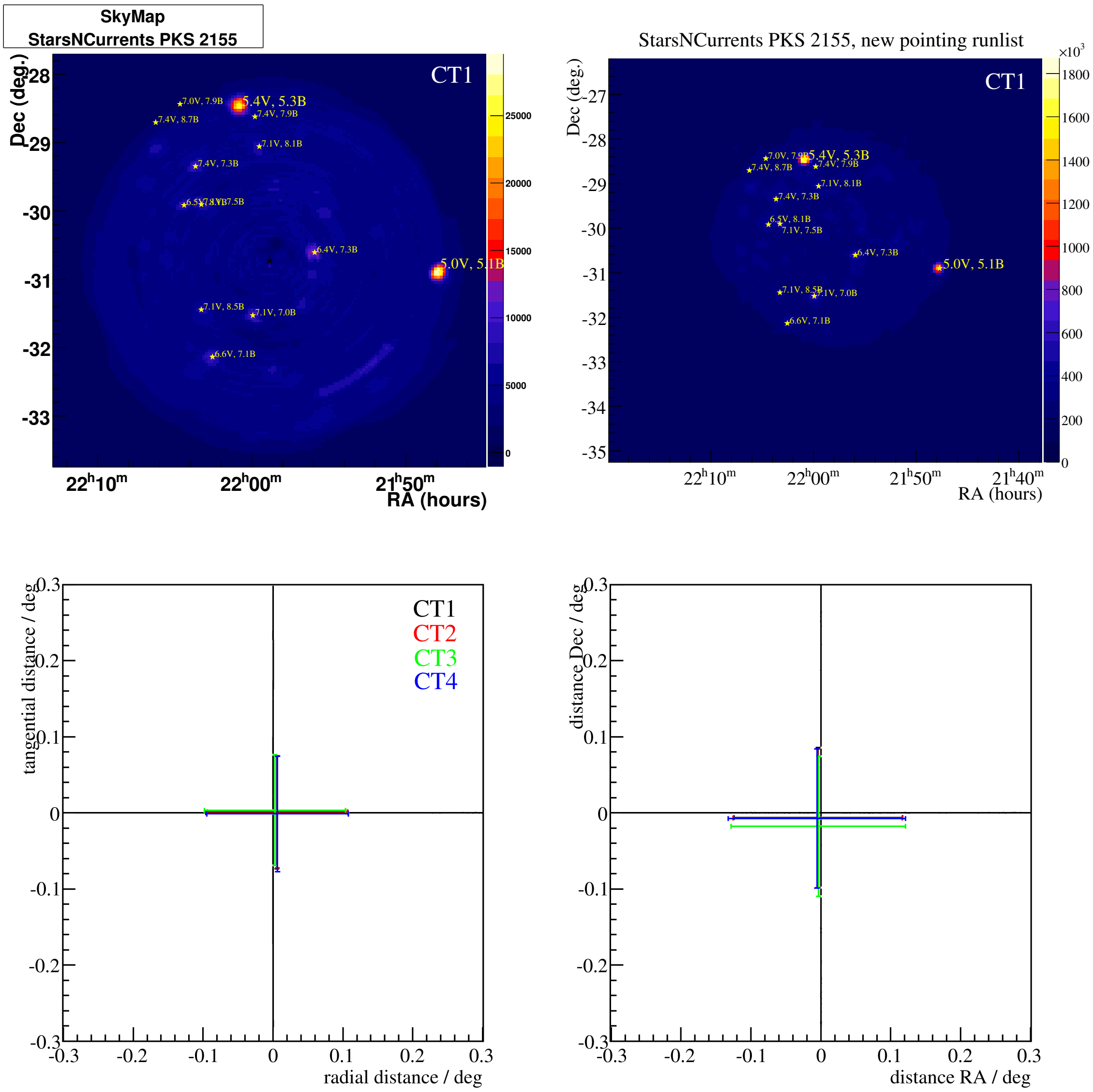

Figure 3.10: **Comparison between pixel currents and star positions** for an individual run (top left) and summed over all runs on one source (top right). The histogram representing pixel currents transformed to RA-Dec coordinates is overlaid with the positions of stars in the field of view giving their magnitude in the visual and blue spectral range. The average deviation over all stars successfully fitted in all runs taken in the first half of 2006 (8269 stars in more than 1000 runs) is shown in the two lower histograms. It is split into components in the camera (left: tangential vs. radial with respect to the camera centre) or in the sky (right: declination vs right ascension). The error bars indicate the RMS of the distribution.

4 Sources of Pointing Deviations

In the previous chapter, it was shown with an independent method relating stars and pixel currents, that the standard pointing method is good to one arc-minute if averaged over a large sample of runs. To determine the error more accurately and identify possibilities to improve the systematic error, one has to study the individual components carefully. Several possible error sources have been mentioned throughout the last chapter. This chapter is dedicated to the detailed discussion of those and additional effects.

For the discussion of "errors", it should be distinguished between physical effects of the instrument and inaccuracies of the method used to correct them. For the pointing, physical causes include a misorientation of the whole telescope and deformations within its structure (covered in chapter 4.1) as well as the atmospheric refraction discussed in chapter 3.1. Errors induced during the correction for those processes will be called *methodic errors* and are caused by pointing components like the CCD cameras and positioning LEDs, but also approximations and the accuracy of analysis steps during image processing, model creation or application. While those are generally smaller than the physical errors, they have to be taken into account for the evaluation of orientation and deformation errors that are analysed using the CCD cameras. Details on methodic errors can be found in chapter 4.2.

4.1 Analysis of Telescope Orientation

This section covers the mechanical behaviour of the telescopes and analyses its effects on the pointing accuracy. First, the orientation of the telescope is discussed, beginning with the component measured with the shaft encoders of the tracking system (section 4.1.1), then studying the tilting of the entire telescope in section 4.1.2. In section 4.1.3, elastic deformations of the telescope masts and mirror support structure are analysed, followed by a study of inelastic deformations in section 4.1.4.

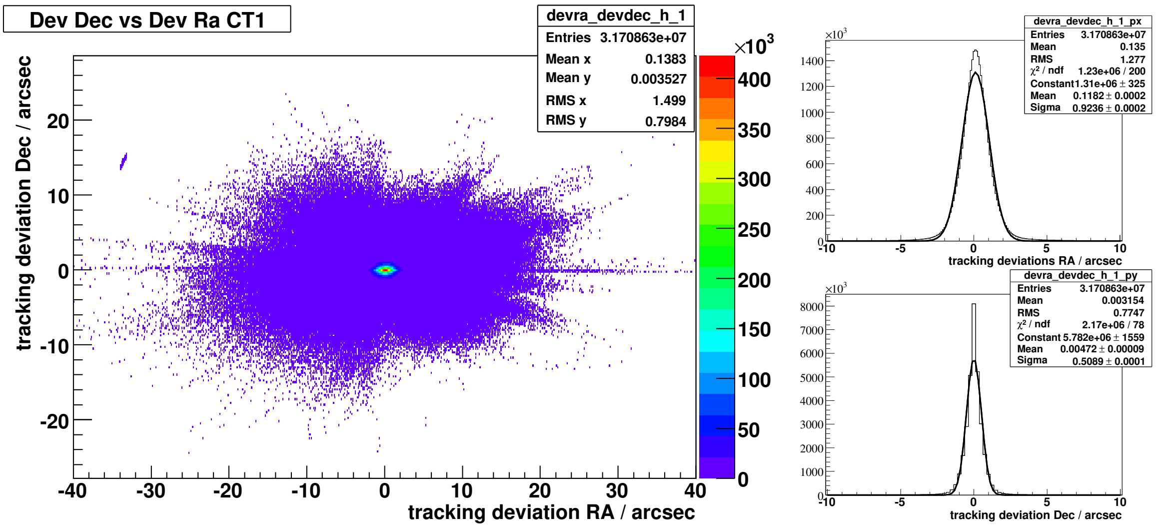

Figure 4.1: **Tracking deviations.** The left graph shows the difference between target position and orientation in right ascension and declination according to shaft encoder information for all runs taken until November 2006. On the right, the projections to the right ascension (upper) and declination (lower) axis are compared to a Gaussian distribution.

4.1.1 Misorientation due to Tracking Deviations

The telescope's orientation toward the desired target coordinate is not always perfect. Deviations caused by welds or other flaws on the tracks, systematic offsets to lower azimuth due to the high tracking velocities required for following sources near zenith and similar influences are measured by the shaft encoders to an accuracy of about 1". Figure 4.1 shows the difference between nominal target position and telescope orientation as measured by the shaft encoders for all runs taken until November 2006.

The tracking may have an additional offset in an interval of 10" that changes from day to day. Assuming that all offsets within the 10" interval (Δ) occur with the same probability, the average error in arc-seconds is given as

$$\sigma_x = \frac{\Delta}{\sqrt{12}} = 2.9'' \qquad (4.1)$$

This is not a systematic error source for standard Cherenkov data, because observations of many different nights are usually combined. Still, a pointing model that is created within one night would imprint the offset to the observations it is applied to. Even though the minimal errors seen in figure 4.1 prove that the tracking can be assumed to *follow* a target position perfectly for all practical applications, this systematic error of 2.9" due to the initialisation offset is introduced.

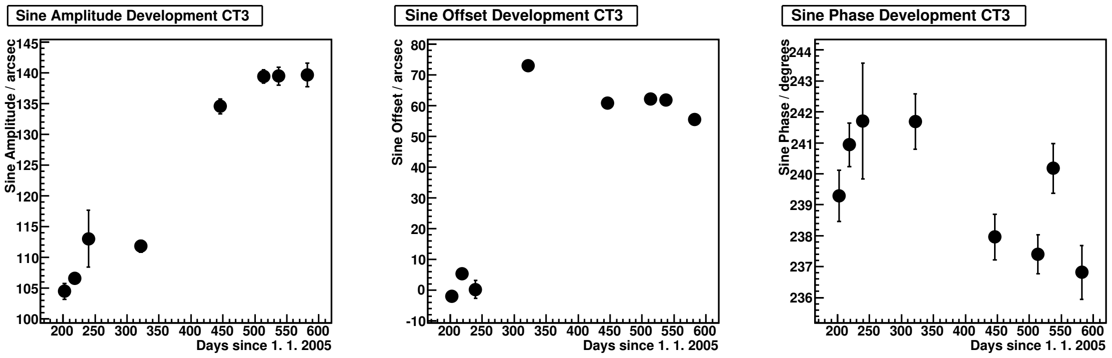

Figure 4.2: **Time evolution of the Azimuth dependence of the vertical star position on the lid.** The fit parameters amplitude (left), offset from arbitrary constant (centre) and phase of a fit to the vertical star position vs telescope azimuth is shown. The increasing amplitude for CT3 can be connected to a minute tilting of the whole telescope towards an Az of 150° (minimum is at phase - 90°), which corresponds to the south-east direction. The step in the offset parameter marks the time of a reorientation of the CCD camera.

4.1.2 Tilting of the Whole Telescope

Once the overall orientation of the telescope according to the internal shaft encoders is known, it is important to determine the relative position of the structure with respect to the sky. As mentioned in chapter 3.2, the tilt of the azimuth telescope axis can be studied using the images of stars on the camera lid. The vertical position of the reflected star after refraction correction varies with telescope azimuth as seen in figure 3.7, indicating a tilt of the telescope.

This tilt is included and corrected in the mechanical pointing model, but it changes with time as seen in figure 4.2: to study the temporal evolution, all pointing runs taken since May 2005 were divided into subsets containing 150 star images and fitted according to figure 3.7. Fits with a χ^2/ndf. worse than 25 were considered to be created from an inconsistent data set, probably caused by maintenance work on the CCD cameras, and omitted. The fit parameters were plotted vs. time.

CT3 continues tilting with a rate of 4"/month, the other telescopes are more stable (less than 1"/month). Pointing models should be regenerated frequently, to reduce the systematic error of CT3 at the end of the period.

4.1.3 Elastic Deformations of the Telescope Structure

So far, the telescope itself could be assumed to be rigid for all considerations in this chapter. But deformations due to gravity exist and depend on the telescope altitude.

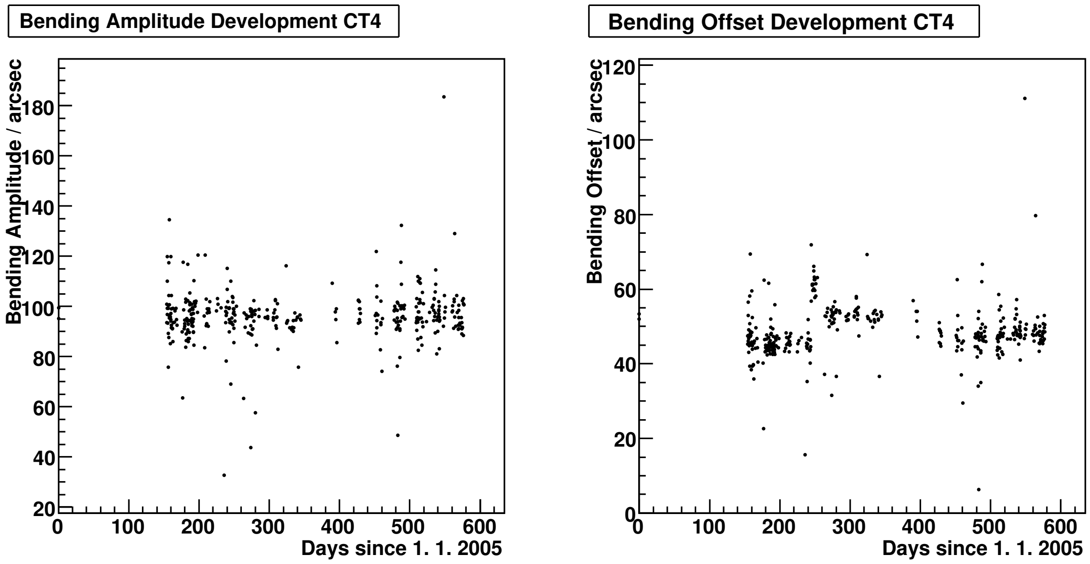

Figure 4.3: **Time Evolution of Bending Parameters.** All available LidCCD data starting March 2005 were subdivided into sets containing 100 images. The data were fitted as shown in figure 3.6 and the fit parameters are shown vs. the average day of the data set.

The deformations are considered elastic if they are reproducible independent of the history of the telescope. Covered in this section are deformations of the camera masts and the dish, including changes of the camera location when the lid is opened. All those effects were studied using the LidCCD.

4.1.3.1 Bending of the Telescope masts

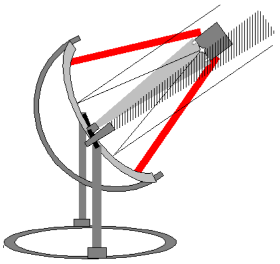

The bending of masts is included in the mechanical model and was mentioned in section 3.2 and shown in figure 3.6. To study the stability of this effect, all available data starting March 2005 were subdivided into smaller sets and fitted to a cosine function as seen in figure 3.6. The evolution of the fit parameters is shown in figure 4.3. It can be seen that the amplitude does not vary significantly over time, indicating no severe aging of the masts. Steps in the offset development are caused by maintenance work performed either on the CCD cameras or on the Cherenkov camera if the latter involved unmounting the funnel plate.

Again, the effect is covered by the mechanical model. Because of the stability of the correlation between altitude and caused camera offset, it does not induce additional systematic errors to the pointing, but makes the creation of a new model necessary after major maintenance work.

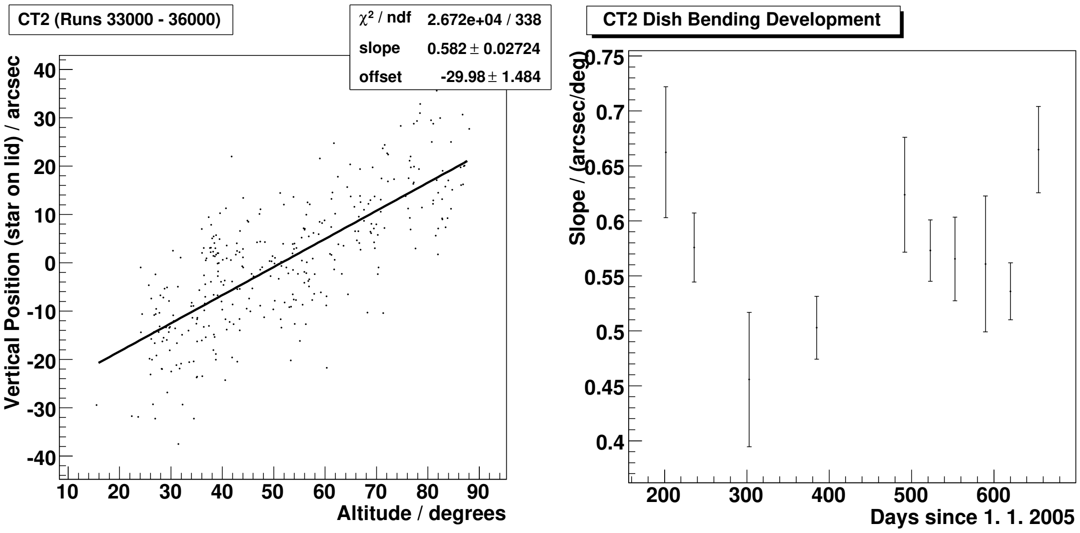

Figure 4.4: **Dish Bending.** The vertical star position from pointing runs of CT2 between June and November 2006 was corrected for refraction as well as the tilt of the azimuth axis and plotted vs. altitude. The right figure indicates the time development of the slope parameter for CT2.

4.1.3.2 Deformation of the Mirror Support Structure

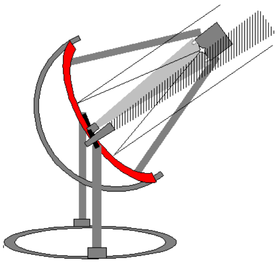

The camera masts are attached to the dish structure, which also supports the mirror facets. The pull of gravity on the masts and the mass of the structure itself can cause deformations and therefore affect the arrangement of the mirrors. This could change position and shape of the reflection on the focal plane, thus manifest as position dependent optical aberrations of the telescope.

To measure the effects of dish deformation on the imaging quality of the telescope, images of stars on the Lid can be analysed regarding to their shape and position, if one keeps in mind that the CCD cameras, too, are attached to the dish, and the deformation could also have indirect effects on the LidCCD. In chapter 4.1.4.2, it will be shown that the behaviour of the LidCCD with respect to the dish is reproducible, therefore the LidCCD is a valid tool to measure the imaging properties relevant for pointing issues.

After refraction correction and the correction of the axis tilt described in chapter 4.1.2, the vertical position of a target star still depends on the altitude of the observation as seen in figure 4.4. The direction of the effect (the star appears lower at lower altitudes) indicates that CCD bending is not the dominant effect. The slope of the dependence and magnitude of the effect over an operational range of 60° altitude are given for the

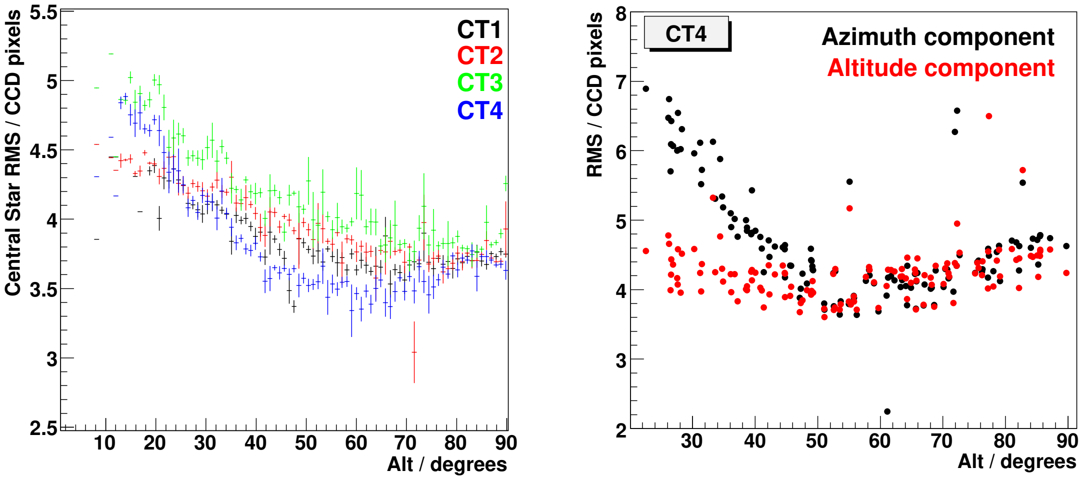

Figure 4.5: **Dish deformation.** The left image shows a telescope-wise comparison of the RMS of the spot created by the target star in all pointing runs, from July 2005 to November 2006 (about 1700 runs) in a profile histogram. The right image shows the altitude dependence of the horizontal (azimuth) and vertical (altitude) component of the RMS only for June 2006 and CT4.

	Slope star vs. alt	mag./60°	mean dist. from fit
CT1	0.17"/deg	10.2"	7.8"
CT2	0.58"/deg	34.8"	6.2"
CT3	0.52"/deg	31.2"	12.2"
CT4	0.42"/deg	25.2"	7.4"

Table 4.1: **Dish bending.** .

different telescopes in table 4.1. The fit parameters do not show a significant trend over time that would indicate structural aging.

The width of the central spot is shown as function of altitude in figure 4.5. The spot is well contained within one Cherenkov camera pixel (about 42 CCD pixels). It can be seen that the spot is generally wider in the horizontal direction for low altitudes but the extensions become comparable above 60° altitude, which can be attributed to the fact that the initial mirror alignment was performed on stars above 50° altitude.

Dish bending is contained in the mechanical model (not explicitly, but in combination with mast bending), and due to its temporal stability it induces no additional systematic error. However, the large spread of positions contributes to the statistical error of the method.

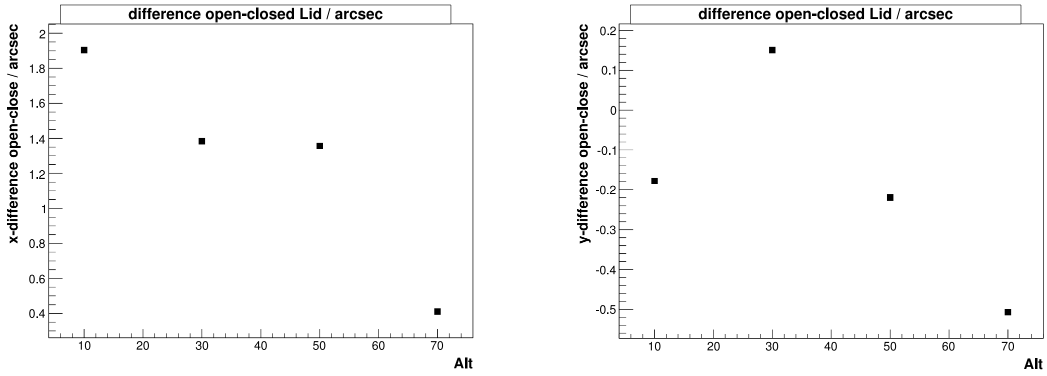

Figure 4.6: **Effect of opening the camera lid.** The figures were created from pairs of images taken at different altitudes on CT4. One image was taken with an open, the other with a closed camera lid. The difference of the reconstructed camera centre between the two images (open-closed) in horizontal (x-) and vertical (y-) direction was plotted vs. the altitude. As indicated in appendix C, the LidCCD of CT4 would see the camera lid opening to the right, so at larger values of x.

4.1.3.3 Torque of the Camera due to the Weight of the Lid

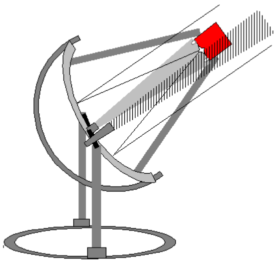

When the camera lid opens, it changes the centre of gravity of the camera, which produces a small shift of the camera position. This leads to a difference in the reconstructed camera centre between pointing runs and observation runs coming from the closed or opened lid.

To measure this error, images of the LEDs with opened and closed lid have been taken shortly after each other at different altitudes. Figure 4.6 shows the altitude dependent shift of the extracted camera centre in the direction of the movement of the centre of gravity. The maximum deviation of all telescopes is 2” at 10° or 1.5” at 50° Altitude. While the deviation is very small for typical observations, it is an unavoidable source of error for the standard pointing method, as pointing runs require a screen for the image of the test star.

4.1.4 Inelastic Deformations

The last deformation effect discussed in this chapter covers inelastic deformations yielding a different telescope response depending on the history of the measurement.

The term hysteresis will be used to describe a different pointing direction depending on the previous positions of the telescopes. It will be shown that the highest previous target altitude since park-out is the key variable for this effect.

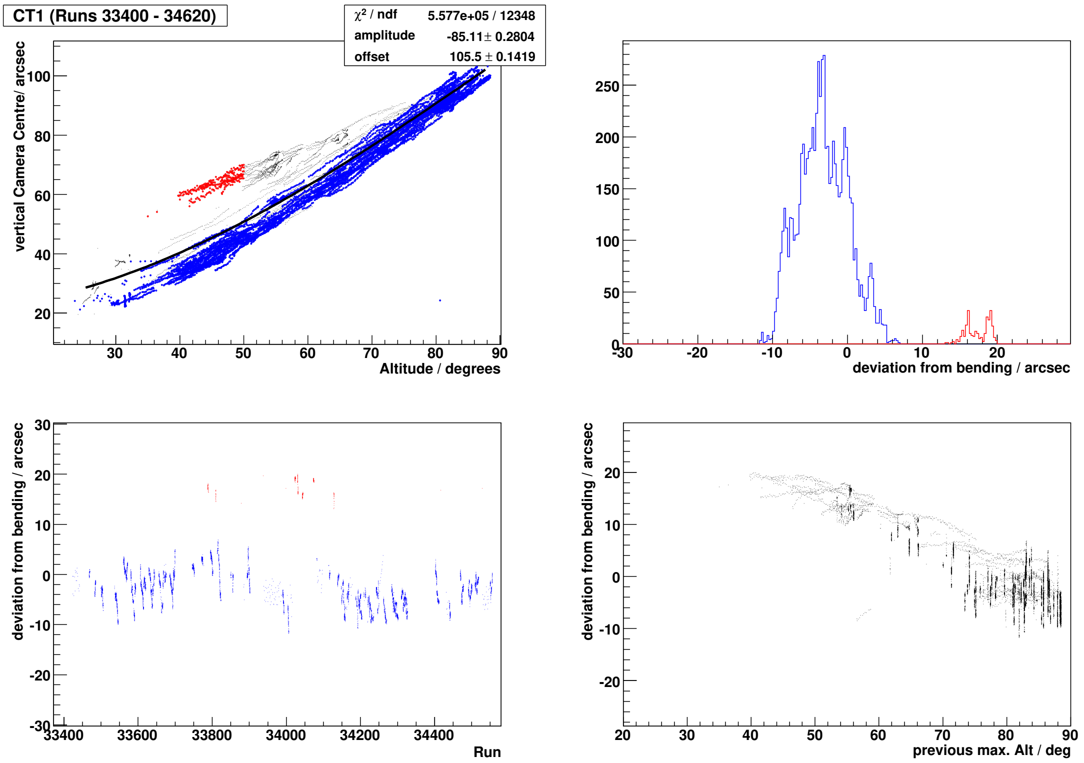

Figure 4.7: **Observation of Inelastic Bending Behaviour** for CT1 in July-September 2006. The data set is split into runs for which the telescope has been above 80° before in the same night (blue), and those for which the previous altitudes did not exceed 50° (red). The figures show the vertical camera centre vs altitude, the deviations from the fitted cosine function histogrammed and as function of run number, and the dependence of the deviation from the fit on the maximum previous altitude.

4.1.4.1 Hysteresis Observations

Figure 4.7 shows measurements taken during regular observation implying some sort of inelastic behaviour. The top-left plot of this figure shows the bending of the camera masts as discussed in section 3.2, but this time a separate population of data points above the main set can be seen. Its difference from the other points becomes clear when the data set is divided into measurements where the telescope was operated above an altitude of 80° before the measurement was taken and those for which the previous operations did not exceed e.g. 50° (marked red). The mast bending at lower altitudes right after parkout obviously differs from that after the telescope pointed upwards. To quantify this peculiarity, the vertical camera centre deviation from the fit can be used. The upper right plot shows the split of those two samples, the lower left plot its development with run number. The lower right plot shows the deviation from the fitted cosine function on the maximum altitude that was reached before within that night.

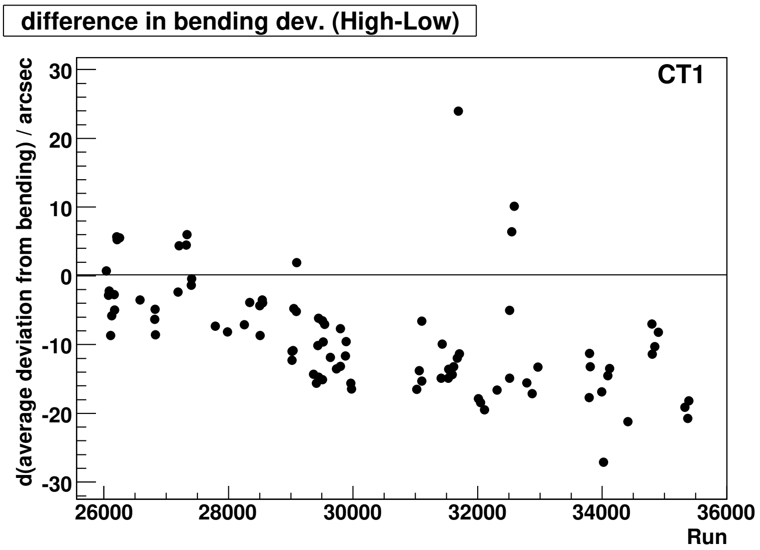

Figure 4.8: **Time development of the hysteresis effect** for CT1 between June 2005 and November 2006. The deviations from the bending fit are filled in separate histograms until each set contains at least ten points. Then, the average of those runs where the previous altitude has not reached 50° is subtracted from those where the telescope has been above 80° and the difference is plotted vs. runnumber.

The effect is increasing with time for CT1. To show this, the "blue" and "red" data points have been histogrammed separately until each subset contained at least ten measurements. The average of both histograms were subtracted ("blue" minus "red") and the difference was drawn vs. the run number where the required number of entries was collected. This time development is shown in figure 4.8. A trend towards a stronger splitting is visible. In summer 2006 the splitting reached 20” between 40 and 50° altitude, and even measurements at 70° altitude are subject to hysteresis in the order of 5”.

Of the other telescopes, CT3 shows the largest similar split with a magnitude of 5”, the hysteresis shifts of CT2 and CT4 are in the order of 2” (Appendix D). Pointing runs usually reach high altitudes near the beginning of a test sample, therefore large zenith angle observations of several nights are subject to this systematic error.

Fig. 4.9 visualises directional considerations for several possible causes. Since subsequent to park out, the camera appears higher than after pointing to high altitudes, the most intuitive explanation, a deformation of only the telescope masts, is not supported. Further investigations of the origin of the effect are introduced in the following section.

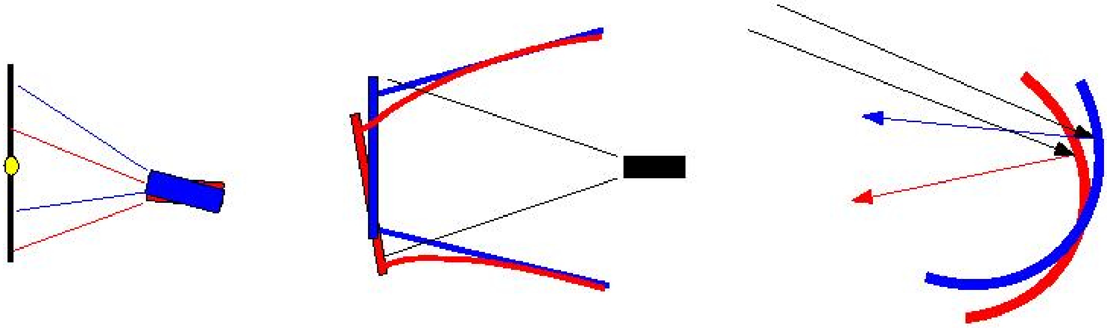

Figure 4.9: **Directional considerations for inelastic deformation effects** as expected if the difference was created by the reduced pull of gravity at high altitudes. The red version of each sketch visualises the situation including possible deformations caused by the gravitational pull, the blue version symbolises the possible change after pointing at high altitudes.

4.1.4.2 Special Test Measurements

To explain the observations presented in the previous section, dedicated test runs were taken that provoke the effect in a reproducible manner. Low pointing runs on the same star are taken right after park out and after pointing near zenith, then the initial conditions are restored with a park-in and the measurements are repeated for comparison. Figure 4.10 shows results from such a test. The camera centre (left figure) shows a step of over 20" when the telescope is moved near zenith, that is restored after parking in. The right figure shows the vertical deviation from the modeled star position in the SkyCCD. The behaviour is similar to the camera centre, with about half the amplitude. It is sufficient to visit the high altitude shortly (one minute) and a short park-in resets the system.

Figure 4.11 shows tests for the influence of several possible error sources. A detailed discussion of the investigation will be given in appendix D, here only the results will be summarised:

- a shift was seen for the camera centre, the reflected star on the camera lid (in position and spot size) as well as the observed star in the SkyCCD.
- the direction is the same for all three observables (the measured position is lower after the telescope was pointing up).
- the LidCCD is fixed to the central hub.
- the magnitude of the effect depends on the maximum previous altitude.
- the star images are subject to an additional short term movement on timescales of minutes that indicates a gradual rising of the whole telescope structure after reaching the target. It does not matter whether the approach happened from higher or lower altitudes.

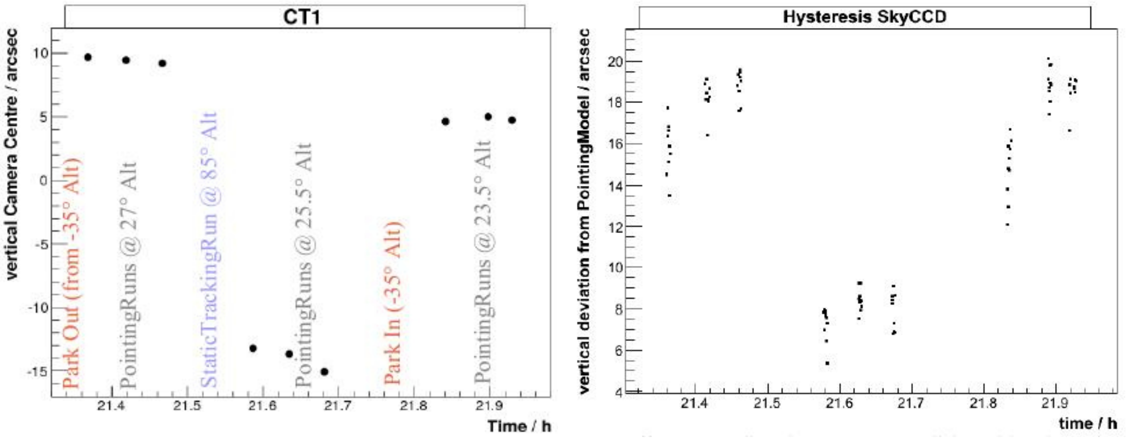

Figure 4.10: **Special test runs to investigate the hysteresis effect** were performed in May 2006. The left image shows the vertical position of the camera centre on CT1 for a sequence of pointing runs on the same star. The smaller overall trend to lower values corresponds to the difference in bending at the different altitudes of the setting star during the test. In the right image, the difference between modeled and measured star position in the SkyCCD is shown for the same runs.

The observations can only be explained by a deformation of the whole telescope structure of CT1.

Differences between an observation shortly after parkout and one after pointing the telescope close to zenith could threaten the valid application of special reference runs to a given observation. Therefore the observation procedure was changed to always park out to the zenith if the sun is below the horizon (effective late January 2007).

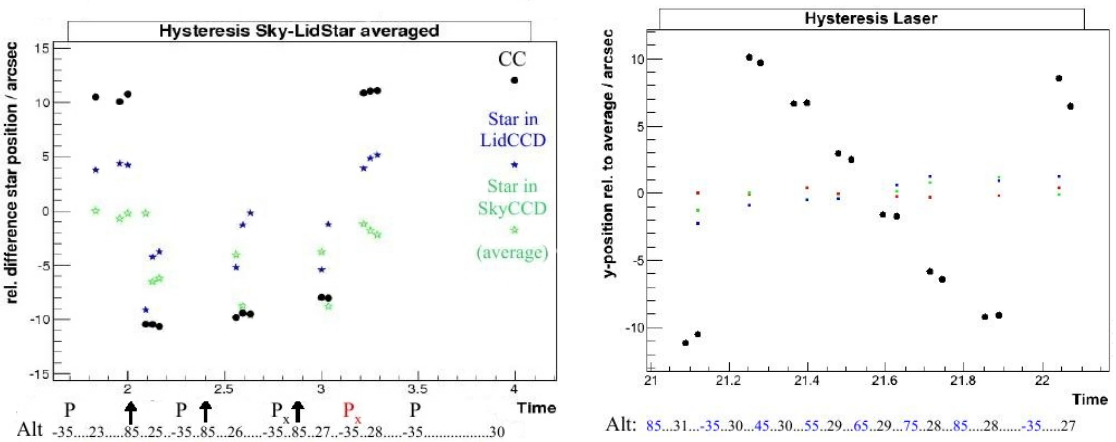

Figure 4.11: **Dedicated hysteresis test runs.** The left figure shows the movements of the pointing star in Lid- and SkyCCD compared to the camera centre. In average over the runs of each subset, the three observables show similar behaviour with the same direction, but different magnitudes. The star positions are additionally affected by a short term variation indicating that the telescope structure moves up on a timescale of minutes. The figure also shows no difference between a park in with closed (marked as P) or open camera lock (P_x). The right figure shows the dependence of the camera centre on the altitude the telescope was moved in between tests. Altitude values are given below the figure. Blue numbers indicating movements of the telescope to higher Altitudes or parking in (marked as Alt -35), black values show the altitudes at which the test pointing runs were taken. Small coloured points show the relative location of spots created by lasers attached to the LidCCD.

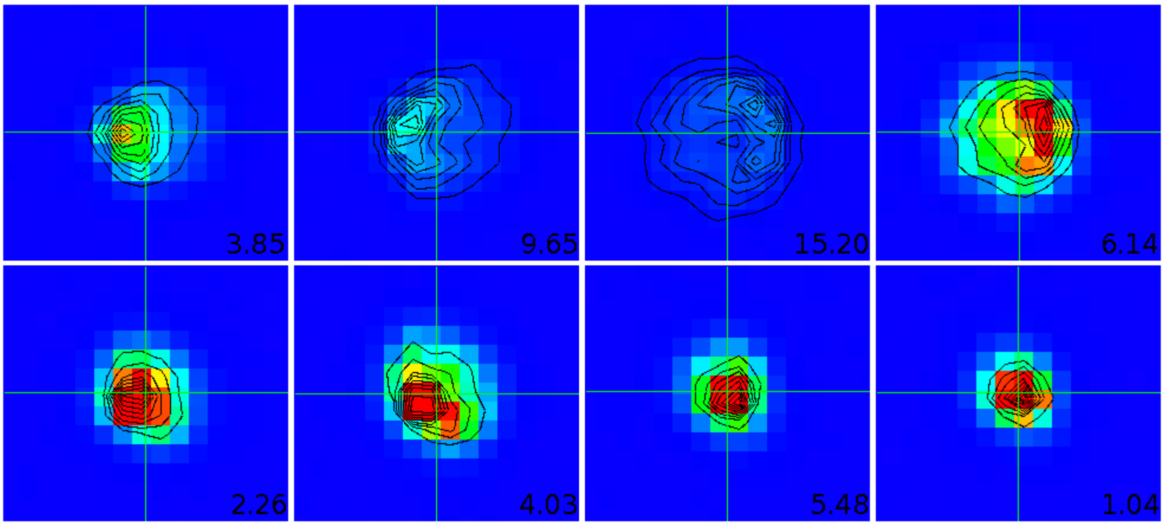

Figure 4.12: **Spot shapes of the eight LEDs on CT3.** The colour scale is linear and the same for all sub-images. The contours show eight isolevels between the background level and maximum pixel intensity of each spot with logarithmic spacing. The crosshair shows the reconstructed spot position. The deformation values are given for each spot.

4.2 Systematic Errors of the Measurement

Most of the studies discussed in the previous sections were performed with the help of the LidCCD, so it is necessary to understand its behaviour in order to evaluate the previous results. Pointing models are also based on CCD data, correct image processing, the modelling accuracy and a correct representation of the funnel entrances by the measured LED spots. This chapter contains the discussion of those components.

4.2.1 Analysis of the CCD Camera Optics

In H.E.S.S., the pointing accuracy depends strongly on the CCD cameras, which are subject to different inaccuracies in the lens or the placement of the CCD chip in its focal plane. Two observations indicate such effects:

- The images of some positioning LEDs in the LidCCD show deformations that are independent of the diffusors. An example image of CT3 is shown in figure 4.12. The two upper right spots appear as arc-like structures, while other spots

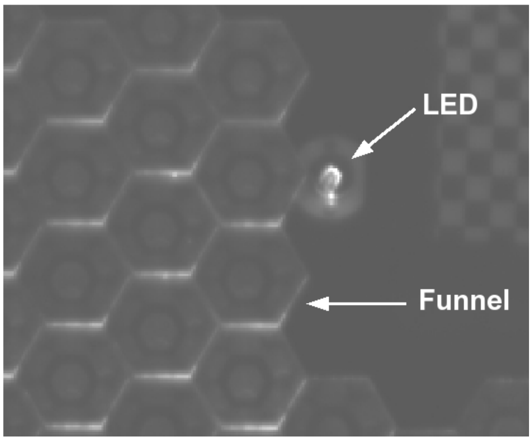

Figure 4.13: **Example for the wavelength dependence of the deformation.** The picture shows an image of the upper right positioning LED of CT3. The camera was illuminated with faint white light, therefore the funnels are visible. It can be seen that while the (red) LED is imaged as a large arc, the lines reflected from the funnels are not extended in a similar way.

in the lower right are point-like in comparison. The tail of a deformed spot points to the centre of the camera.

- Another observation can be seen in the left image of figure 4.13 that shows an illuminated section of the camera together with a positioning LED. The arc-shaped extension of the LED spot exceeds the width of imaged funnel structures, indicating that the deformation depends on the wavelength of the detected light.

To quantify the investigation of those two effects, a *deformation value* was introduced in [Mol04] that measures the intensity deviations of a spot from a fitted Gaussian shape. For each CCD pixel the deviation between the measured intensity and the value of the Gaussian fit is calculated. The sum is normalized to the integral over the Gaussian function. The values given in figure 4.12, but also figures 4.14 and 4.15 refer to this parameter.

These observations could either be caused by the lens or the chip of the CCD camera, so those two components will be studied separately in the following two sections.

4.2.1.1 Lens Aberrations

Any lens is subject to spherical and chromatic aberrations leading to imperfections either depending on the incident parameter relative to the optical axis or the wavelength of the projected light.

Chromatic aberrations are caused by a wavelength dependence of the refractive index called dispersion. Due to this effect, the focal length varies with colour and

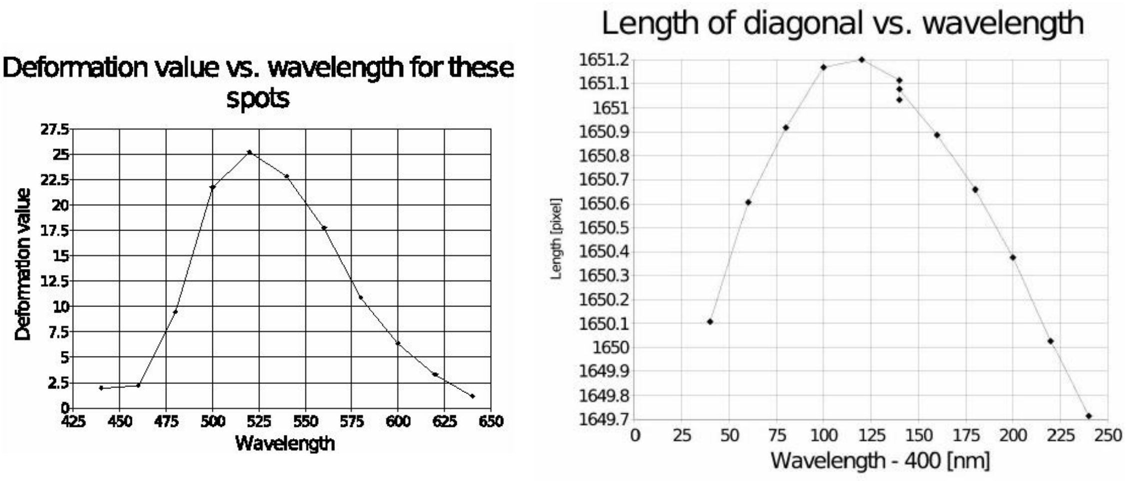

Figure 4.14: **Wavelength dependence of the deformation.** Images from [Mol04]. The wavelength dependence of the deformation value (left) and the length of a measured diagonal (right) is shown.

focusing can only be successful for a narrow spectral range, while other wavelengths will appear blurred. As any single lens suffers from this effect, quality camera lenses consist of an elaborate system of different correction lenses to compensate for dispersion in the visible range.

Chromatic aberration affects the pointing in two ways:

- because the sensitivity of the CCD chip used extends into the IR range, images of stars show a significant widening that is avoided using a filter to block IR light.
- the shape of a spot far from the optical axis depends on its colour, which affects images of the positioning LEDs. It was found that the deformation value was largest for 525 nm with smaller values towards blue and red light. This can also change the position of the peak, so individual spots in the corner could obtain position errors in the order of 0.5 CCD-pixels (or 7” for the LidCCD with the 135 mm lens) depending on their colour (see figure 4.14). Therefore the observed magnification is also wavelength dependent. It reaches a maximum for 525 nm. Close to the edge of the image, the values for 450 nm and 600 nm are 0.5 ‰ below that maximum (figure 4.14).

The large aperture desired to detect faint stars favours an additional error called **spherical aberration**. Rays that pass close to the edge of the lens are focused on a different plane than rays close to the optical axis. This additional blur of the image could be avoided with aspherical lenses, but because of their high costs, it is usually corrected to a large degree by the lens system. Off-axis spots may show tails called *coma* because of this effect. It can be reduced by closing the aperture to reject rays passing the lens far from the optical axis.

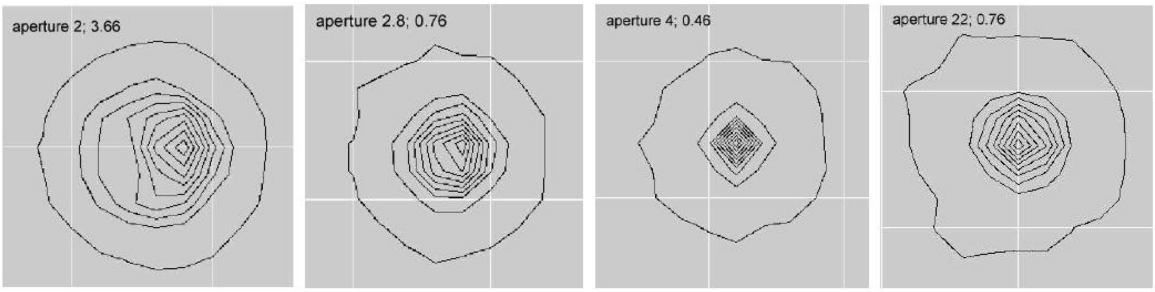

Figure 4.15: **Aperture dependence of the deformation.** Image from [Mol04]. The deformation value and spot contours are shown for images of the same spot taken with different apertures.

The LidCCD lenses show deformed spots toward the edge of the image for the large apertures of f/2 and f/2.8 (figure 4.15). The deformation lessens and then remains stable for apertures smaller than f/4, but shows a small increase again for f/22. As spherical aberration yields radially symmetric distortions, the influence on the reconstructed camera centre is insignificant as long as the image is symmetric, so it was decided to retain the large aperture of f/2.

Both, chromatic and spherical aberration change the shape of spots far from the optical axis of the CCD camera. This has an influence on the reconstructed position of the spot reaching as much as 7" for individual corner spots due to chromatic aberration. The influence of spherical aberration on the position can not be measured directly because the camera has to be touched in order to change the aperture, but the range of observed deformation values is small compared to chromatic aberration. Therefore optical aberrations are combined to a systematic error of 7" for individual spot positions. The error on the reconstructed camera centre depends on the symmetry of the image as discussed in section 4.2.2.2.
So far, it could be explained why off-axis spots show wavelength dependent deformations, but not why different corners of the image should be affected differently. The reason for this asymmetry will be investigated in the following section.

4.2.1.2 Chip Deformation and Expansion

This chapter covers studies to understand the influence of the CCD chip on the pointing accuracy. First, an explanation for the position dependence of the deformation will be given. Then two other properties of the CCD chip, the thermal expansion of the material and its segmentation into pixels with finite borders are investigated.

Tilt of CCD Chip It was assumed that the position dependent arc shapes could arise if the chip is not perfectly aligned with the optical axis of the lens. The sharpness variations over the field of view presented in appendix B also support this assumption.

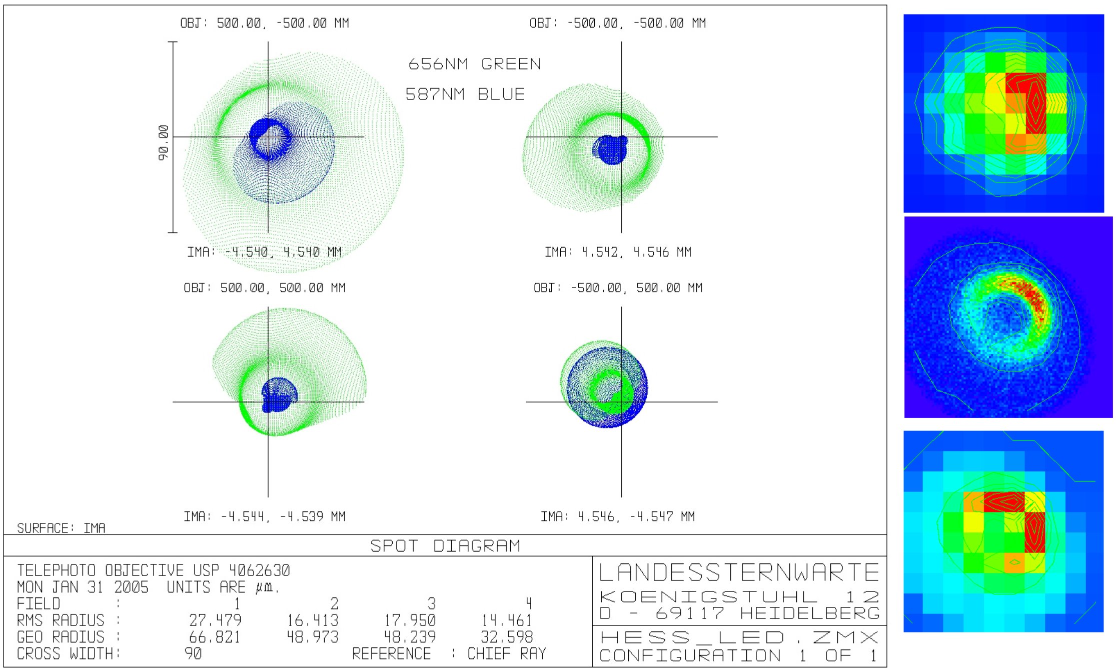

```
TELEPHOTO OBJECTIVE USP 4062630
MON JAN 31 2005  UNITS ARE µm.
FIELD       :       1        2         3         4
RMS RADIUS  :    27.479   16.413    17.950    14.461
GEO RADIUS  :    66.821   48.973    48.239    32.598
CROSS WIDTH:     90               REFERENCE  : CHIEF RAY
```

Figure 4.16: **Spot simulations in different corners of the field of view** assuming a 0.5° tilt of the CCD chip relative to the optical axis. Two different wavelengths of incident light were chosen, and the results are presented in green (656 nm) and blue (587 nm). The simulated spot shapes agree remarkably well with observations (right, top: observed spot, linear colour scale, middle: simulated spot with 10 times finer resolution, x inverted, bottom: simulated spot re-bined). The simulation was performed by Walter Seiferts at the MPI for Astronomy.

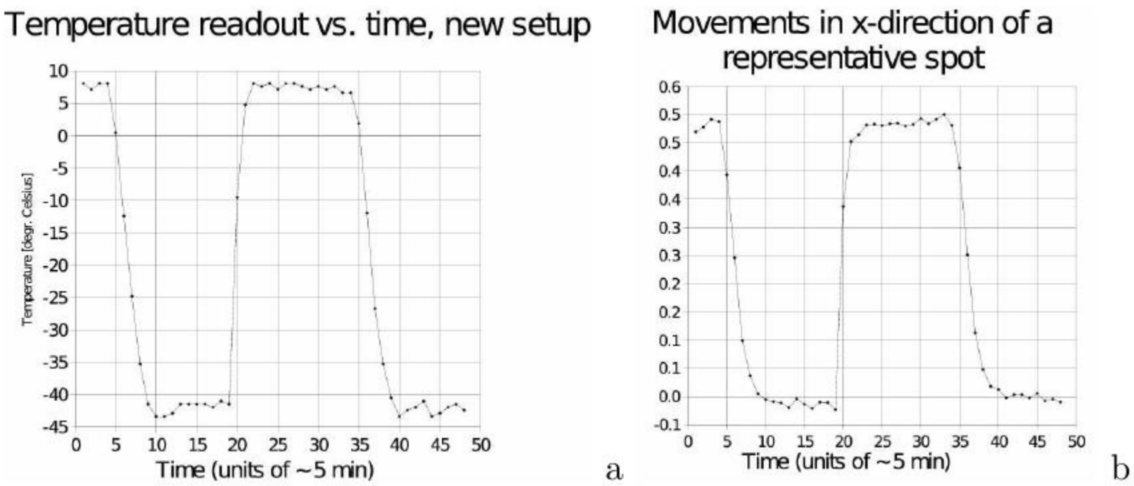

Figure 4.17: **Temperature sensitivity of the spot position on the CCD chip.** Image from [Mol04] showing the movement of a spot depending on the cooling state of the CCD camera. Subfigure (a) shows the procedure: images were taken with an uncooled camera, then the cooling was turned on and the temperature readout falls by about 50° within about 25 minutes. After 50 min in the cooled state, the cooling is turned off and the camera warms up again. After about 75 min, the cooling is turned on again. Subfigure (b) shows the position of a spot during those cooling cycles.

The relative quality of spots in different corners remains the same for different lenses, even the different type used before 2005. Therefore it can be concluded that the misalignment indeed originates within the CCD camera.

Ray tracing simulations were performed by Walter Seiferts at the MPI for Astronomy using a commercial software (ZEMAX [ZEM05]). The software package contains details about many lenses including one that should be very similar to the 135 mm lens. The simulated images are in very good agreement with the measurements for a tilt of 0.5° between chip and focal plane, including the different shapes in different edges and the intensity dip in the centre of strongly deformed spots. Figure 4.16 shows the results of those simulations for two wavelengths. The constructed spots were analysed with the standard spot extraction method to quantify the deviation from the expected position. The displacement between true and reconstructed position averages to 0.5 CCD-pixels or 7” for the LidCCD. This value agrees with the shift found due to chromatic aberration, but due to the asymmetric influence on different corners, the deformation caused by a tilt of the chip influences the reconstructed camera centre. For the simulated spots of figure 4.16, the centre would be reconstructed 10” too low.

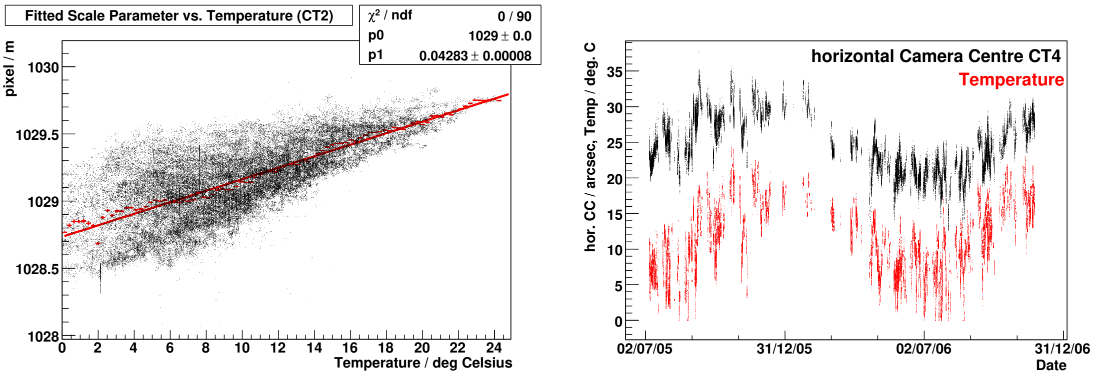

Figure 4.18: **Temperature sensitivity of the spot position.** For all CCD data from CT2 between April and November 2006, the scale of the camera centre fit (CCD pixel / m on the lid) is plotted vs. air temperature. The black points show the individual measurements and a red profile histogram of the same data with a linear fit is added to the figure. The measured slope corresponds to an expansion coefficient of 4.2 $\cdot 10^{-5}$/K. For CT4, the effect can also be seen directly as shown in the right figure.

CCD Cooling The CCD chip is cooled by a Peltier element which keeps it at a given temperature difference to the surroundings. It was noticed that the reconstructed position of a spot depends on the cooling status, so special test measurements were performed in the laboratory to investigate its influence on the image. It was found that the positions of spots move during the cool-down phase. When the camera was firmly attached to a large block of concrete, the spot moved by 8” and stopped in about 5 min.

The movement could be identified as an expansion of the chip relative to a fixed point in one corner. The correlation between temperature and position yields a linear thermal expansion coefficient of $6.5 \cdot 10^{-6}\ K^{-1}$, which is in the same order of magnitude as the expansion coefficient of pure silicon, $2 - 2.5 \cdot 10^{-6}\ K^{-1}$. For a temperature difference of 30 K this corresponds to a maximal error of 4”.

A stronger temperature dependence can be seen in images from the CCD cameras mounted on the telescopes. Figure 4.18 shows the scale of the LED fit as function of temperature. The expansion coefficient of (4.2 $\cdot 10^{-5}$/K) is a factor ten larger than the expansion coefficient of pure silicon and results in a difference of 12”/m for 20 K temperature difference. The discrepancy could be caused by thermal expansion of the lens and CCD mount which are affected by the air temperature, but not the cooling state of the chip. If the chip is fixed in one corner, the camera centre moves by 8”. As a consequence, the CCD cameras in Namibia are now cooled before observation and the air temperature enters as an additional parameter into the new precision pointing method discussed in chapter 5.

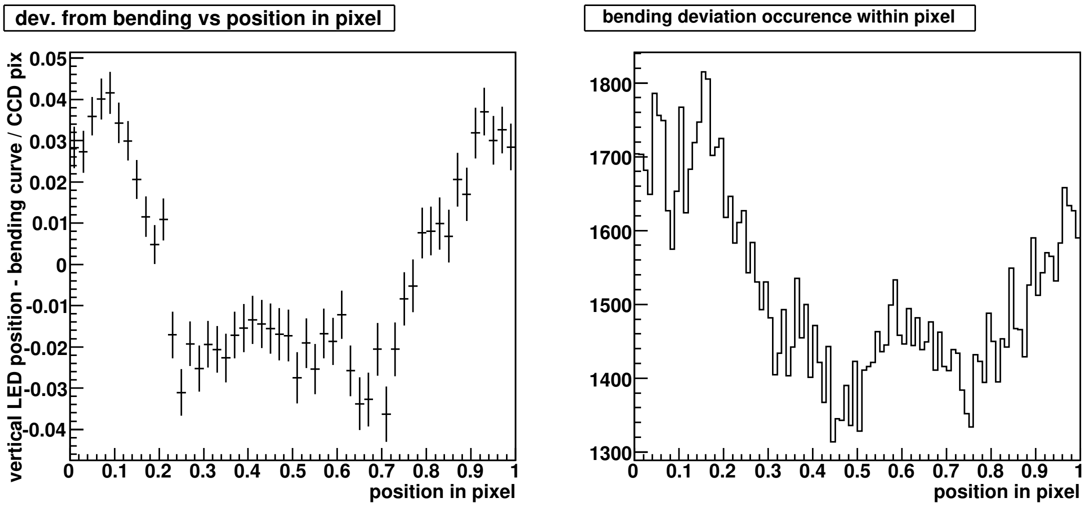

Figure 4.19: **Digitisation.** A bending parametrisation for each individual LED is created (here for CT3). Then the expected vertical LED position according to that model is subtracted from the actual spot position and plotted vs. the reconstructed fraction within each pixel (left figure). The right figure indicates that values with small deviations from pixel borders are favoured in the reconstruction.

Digitisation Effects Binning effects (a small dependence of the reconstructed position on the location within a pixel) in the order of less than 0.1 CCD-pixel can also be seen in real images. It was not found in simulated ones, so the deviation is caused by the borders between CCD pixels and not an artifact of the analysis. Figure 4.19 shows how the mast bending can be used to identify binning effects. Between an altitude of 20° and 90°, the spot regularly crosses about 5 CCD pixels, which can be used for the analysis. It can be seen that the deviations from the expected vertical position are larger at the pixel edges. The effect is part of the residuals to the bending curve and not corrected, but should cancel out for a large number of measurements.

4.2.2 Inaccuracies of the Image Analysis

All methods using CCD images to identify pointing deviations are subject to a common source of error caused by the analysis procedure used to extract spot positions from images. Influences of the spot shape and intensity or a second spot in the analysis region were investigated.

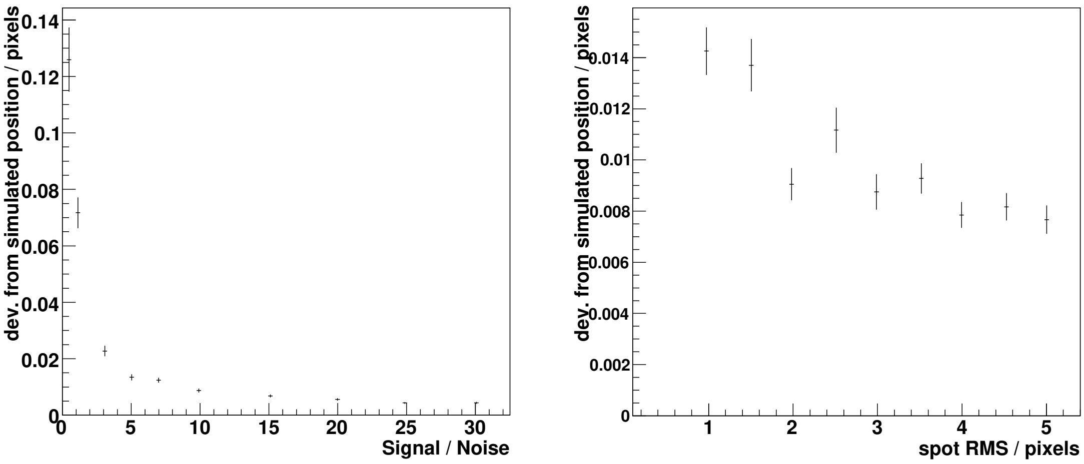

Figure 4.20: **Spot extraction errors** from simulated spots. Each plot is created from 500 images of a Gaussian shaped, randomised peak in a fits image, 50 in each data point. The deviation from the simulated position is shown as a function of signal to noise ratio and spot RMS.

4.2.2.1 Spot Extraction Errors

To independently test the spot extraction (described in 3.3.1), point-like spots with different sizes and intensities have been simulated as two dimensional Gaussian shaped peaks over a typical background level that was randomized following a Gaussian distribution for each pixel value. The extraction algorithm determined the correct position with an accuracy of 0.005 to 0.05 pixels depending on the signal to noise ratio and spot RMS (see figure 4.20). For the LidCCD this would induce an error of 0.07” to 0.7” respectively, while the error for typical spot values is 0.1”. In the SkyCCD this corresponds to 0.016”.

Elongated spots, that were simulated to mimic the extended reflected star on the Lid at altitudes below 50°, usually show errors between 0.5” and 0.8”.

To investigate the influence of a reflection or second star on the reconstructed spot position, images with two Gaussian spots within an analysis window were simulated. Several combinations of spot intensities, background levels and spot RMS were tested for different distances between the two spots (see figure 4.21). A typical value for the influence of a secondary spot with an intensity of 5% of the primary spot with 3 pixels RMS (standard for central star) is 0.17 CCD-pixels or about 2” for the LidCCD.

4.2.2.2 Fit Accuracy

An additional spot within the readout window of the LED can change the result significantly. But also the absence of one or more reference points can influence the

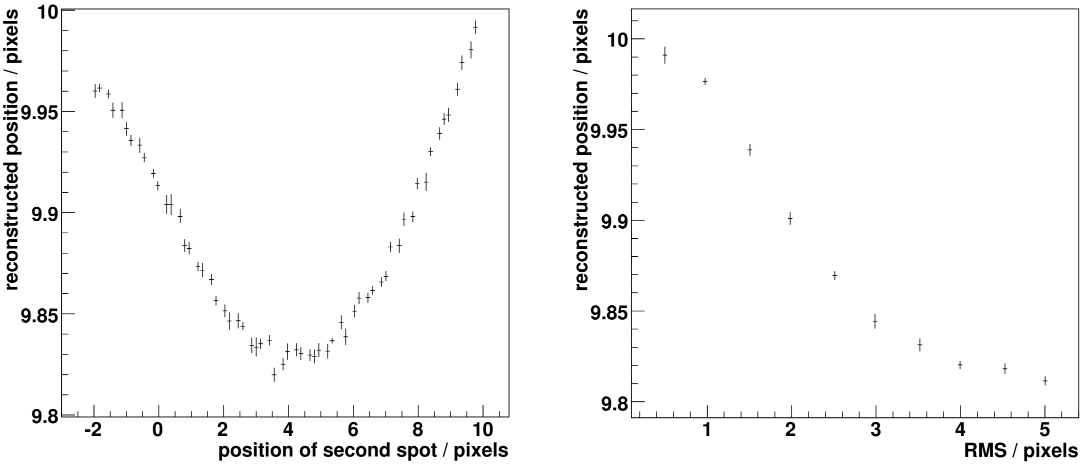

Figure 4.21: **Influence of a second spot on the spot extraction** from simulated spots. A main spot was simulated at a position of 10.0 pixels with a signal to noise ratio of 5 and (only in the left image) an RMS of 3.5. A second spot with the same RMS and 5% intensity of the main spot (25% of the BG) was added with a varying offset. Each data point contains 10 images. The let figure shows the dependence of the influence on the position of the second spot. It can be seen that the reconstructed value differs most from the simulated value when the two spots have a distance of about 6 pixels. The second spot even influences the position if it is outside of the analysis frame (starting at 0). The right image shows the dependence of the size of this effect at 5 pixels distance on the RMS of the spots. It can be seen that the increasing overlap of the two spots enlarges the shift towards the position of the second spot, but the influence on the width levels off when the RMS approaches the distance between the two spots.

reconstructed centre if the relative positions do not perfectly match the design pattern. Optical aberrations and a tilt of the CCD chip with respect to the optical axis add to the mechanical variations. A measure for the relative differences is the residual of each single LED to the fit result, which is shown in figure 4.22. A small sheer of the positions is visible for all telescopes, the upper half of the image appears shifted to the opposite direction of the lower half, the discrepancy is largest for CT3.

Due to those differences between the individual LEDs, missing spots can shift the reconstructed centre as seen in figure 4.23. For model creation, images with a minimum of seven LEDs are selected to reduce the expected error to 4” (CT4) or less.

In order to estimate the accuracy of the fitting routine under controlled conditions, whole LidCCD images were filled with simulated spots of randomised intensity like those described in section 4.2.2.1 and analysed with the regular procedure. The right

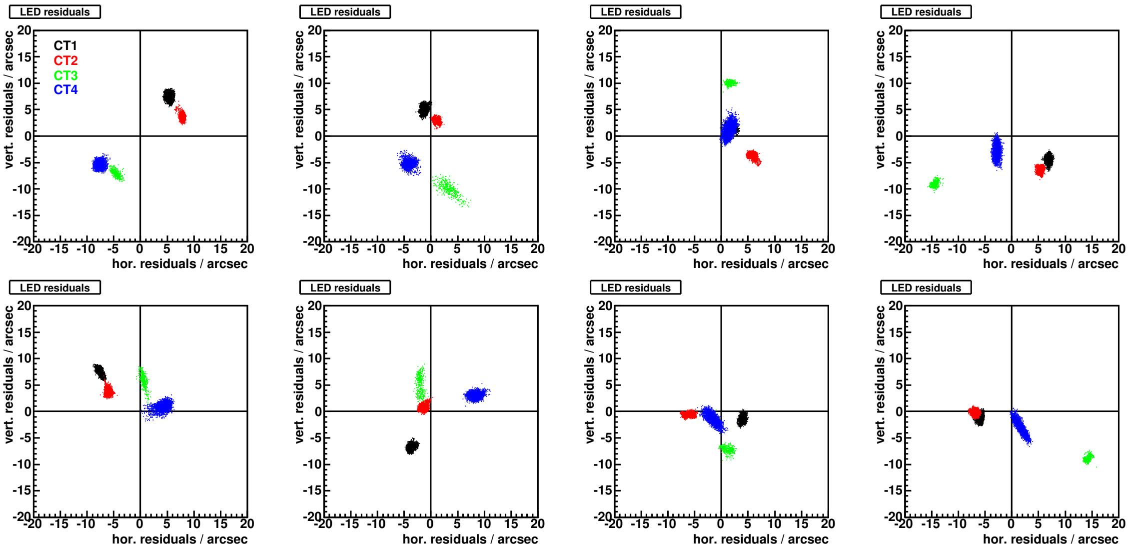

Figure 4.22: **Residuals of individual LEDs to the fit** for about 2000 images per telescope taken in October 2006. The arrangement of subfigures corresponds to the location of the LEDs on the Cherenkov camera.

plot in figure 4.23 shows that the fitting routine returned the correct value for the reconstructed centre with an accuracy of 0.1". Therefore it can be assumed that the previously mentioned variation of the camera centre is indeed caused by physical effects and not an artifact of the fitting procedure.

4.2.3 LEDs as Valid Representation of the Funnel Plate

So far, all measurements of the camera position referred to the positioning LEDs, yet the desired parameter is the location of the Winston cone entrances. This chapter will give details about the accuracy of the connection of those two values.

Both, LED-diffusors and Winston cones are mounted on the funnel plates at positions crafted with a mechanical accuracy of 0.2 mm or 2.5". An accurate measurement is desired to quantify possible additional effects like the fastening of the diffusors, funnel bending and differences between the three funnel plate segments. Especially the position of the central plate, which does not have any positioning LEDs attached to it, can only be measured through funnel imaging.

Initial tests using an illumination of the funnel edges by the moon like in figure 2.5 could not be used to determine the absolute shift because the image was dominated by reflections from the dust inside the funnels instead of from its edge, but this method is still useful for relative measurements between the three plates. A step of 0.4 mm could be identified between two segments on one telescope. This shift may change when the

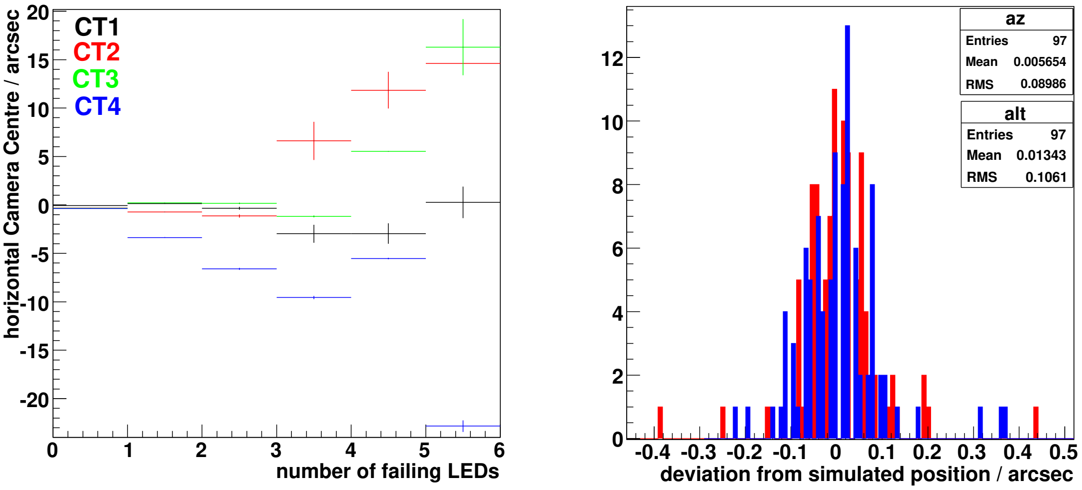

Figure 4.23: **Influence of missing LEDs** on the horizontal reconstructed camera centre. Images taken between July and November 2006 were used. The right plot shows the deviation of the reconstructed camera centre for simulated LidCCD images.

funnel plates are removed for maintenance work on the drawers (and, unless it affects only the central segment, is also seen in the LED positions (see figure 4.24)).

A direct testing method relative to the LED positions was desired, that should avoid the reflections from dust inside the funnels and be harmless for the touch-sensitive funnels and light-sensitive camera. An optical measurement with the LidCCD had the advantage of getting the deviation from the centre as it is determined in regular pointing- or observation runs.

The chosen design of so called *funnel markers* is shown in figure 4.25. Sixty markers were produced and inserted between the funnels of three CTs in Namibia for test images. They were illuminated with green LEDs from the central dish to ensure minimal chromatic aberrations without harming the PMTs. Images were taken at three different altitudes and with different exposure times. Each image was cleaned from reflections on the unshielded funnels, then the lines were fitted and shifted to the centre using a previously determined optimal image scale and rotation. The intersections of those lines give the centre position as well as its statistical error. The systematic error can be derived from the line-finding method (0.09 CCD-pixels statistics + 0.1 CCD-pixel systematics), the error caused by the assumed scale and rotation (0.01 CCD-pixel systematic) and the statistical spread in the images with different exposure time (0.05 CCD-pixels), yielding 0.2 CCD-pixels or 3" for the combined error of the method. Figure 4.26 shows the results of this measurement. While it is unfortunate that no shift could be measured for CT3 where the previous chapters indicated the largest

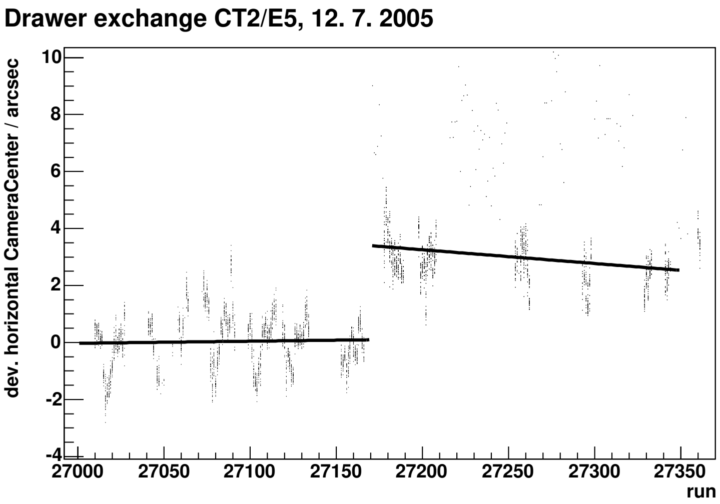

Figure 4.24: **Shift of the camera centre after a drawer exchange**

LED problems, no significant shift of the whole camera was found within the accuracy of the method for any of the three telescopes.

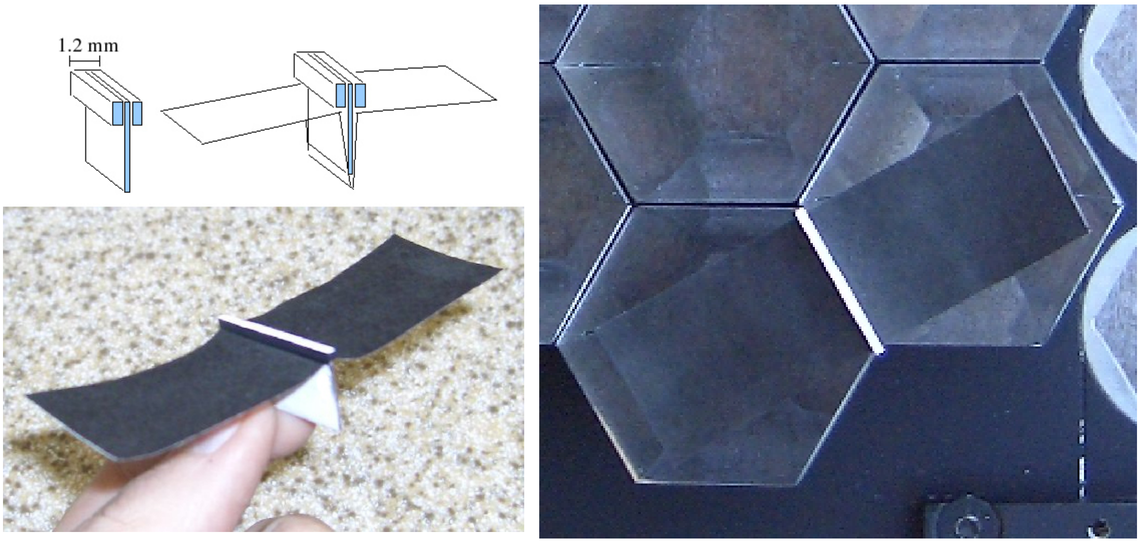

Figure 4.25: **Funnel marker:** the design consists of thin metal blades with additional metal pieces attached at the top edge to form a symmetric T-structure for better visibility. The top is painted white, the sides black. "Wings" made of black paper block light from inside the funnel.

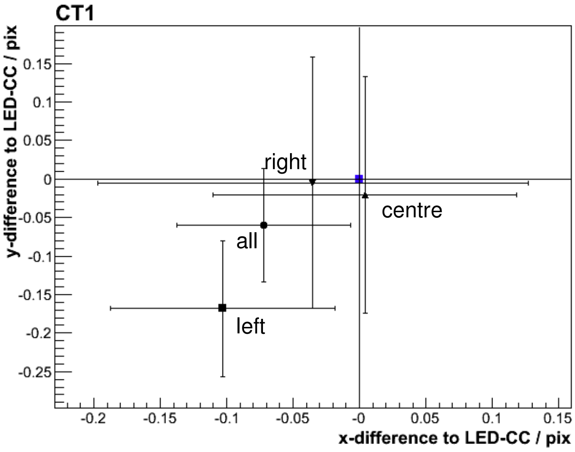

CT	hor. Shift	vert. Shift
CT1	-1.0”± 3”	-0.8”± 3”
CT2	-1.8”± 3”	-0.8”± 3”
CT4	-3.7”± 3”	+0.6”± 3”

Figure 4.26: **Difference of the camera centre between LEDs and funnel marker.** The diagram shows the determined differences for the different funnel plate sections of CT1 and the whole image. The table presents the overall values for all three tested telescopes.

4.3 Overall Performance

Being a stereoscopic instrument, H.E.S.S. uses a combination of data from different telescopes for the reconstruction of the source location. For showers seen in two telescopes, the error of one telescope enters into the averaged error on a source with a factor 1/2 for events including the affected CT, which is the case for one half of these events. The influence is even less for the rarer three- and four-fold events. Therefore a 20” error that is unique to one telescope like the hysteresis error of CT1 can be expected to shift the source position by less than 5”. For the hysteresis example, however, the smaller shifts seen in the other telescopes are not independent of each other, so they are not added quadratically and yield a combined error of 8”.

In general, the individual errors σ_i of the CTs were combined to the error Δ_{system} of the array according to

$$\Delta_{system} = \sqrt{\sum_i^{CTs} (\sigma_i/4)^2} \qquad (4.2)$$

if the errors for the different telescopes were independent and

$$\Delta_{system} = \sum_i^{CTs} (\sigma_i/4) \qquad (4.3)$$

if the cause of the error was external and therefore the errors connected.

Table 4.2 presents a collection of the errors discussed throughout this chapter. The column "Com." states whether the errors of individual CTs are assumed to be independent (Q) or not (L) for the calculation of the system inaccuracy.
Additional remarks:

- *Misorientation* denotes the error from a different shaft encoder initialisation value than during model creation.
- *Tracking* describes the ability of the tracking system to correctly follow a source. It is marked as systematic error, because for high altitudes, the telescope might be systematically "behind" the source due to the limited tracking speed. It is also a statistical error.
- *Refraction model* accounts for the possibility that the used parametrisation is not correct (estimated from the difference of two different models), *Refraction* means the instantaneous differences due to atmospheric parameters or the wavelength.
- the two values given for *Hysteresis* are valid for the camera centre and the star on the lid respectively.
- *Optical aberrations* are seen for the individual LEDs, but their influence on the pointing is limited to asymmetric conditions, which are covered by the points *Tilt of the CCD chip* and *Fit accuracy.*

To calculate the combined accuracy of the system, statistical errors (written in italics) affecting the Star on the Lid (Star_L) and the camera centre (C.C.) were added quadratically for each telescope assuming independence. Then, the telescope errors are combined according to (4.2).

Four systematic errors depend on the altitude, three of them being larger for lower altitudes: the error due to an inaccurate refraction model, the shift of the camera centre when the camera lid is opened and hysteresis. The refraction affects a different observable then the opening of the lid and is in first order independent of the hysteresis[1]. The error of opening the lid should not depend on the history of the observation, but since it was not tested for a correlation, these two errors will be added linearly. The rest of the errors are assumed to be independent and are added quadratically, because the large number of errors to be combined makes it highly improbable that all of them influence the result in the same direction.

The combined error of the H.E.S.S. array in four telescope operation using the standard pointing method six months after the creation of the applied model can be given as ±5" (statistical) ±13" (systematical).

---

[1] ignoring the connection that low observations without going to high altitudes first are more probable at the beginning of the night, when it is typically warmer and the error of the refraction model could be different

Effect		CT1	CT2	CT3	CT4	Com.	Δ_{system}	depends on / remarks
Instrumental errors								
Misorientation	Star$_{L,S}$	3”	3”	3”	3”	Q	1.5”	
Tracking	Star$_{L,S}$	1”	1”	1”	1”	L	1”	altitude (tracking speed)
Refraction model	Star$_{L,S}$	5”	5”	5”	5”	L	5”	model
Refraction	*Star*$_{L,S}$	*O(2”)*	*O(2”)*	*O(2”)*	*O(2”)*	*L*	*O(2”)*	*alt,* λ*, atmosphere*
Telescope tilting	Star$_{L,S}$	1”	0.7”	4”	0.7”	Q	1”	[per month] time
Mast Bending Residuals	*C.C.*	*7”*	*3”*	*4”*	*2”*	*Q*	*2.3”*	
Dish Bending	*Star*$_L$	*8”*	*6”*	*12”*	*7”*	*L*	*8.4”*	
Opening the lid	C.C.	1.8”	1”	1”	2”	L	1.5”	alt
Hysteresis	All	25”/10”	2”/2”	5”/2”	2”/4”	L	8”/5”	CT, previous altitudes, time
Methodic errors								
Optical aberrations	LED	<7”	<7”	7”	<7”	Q	0”(sym)	λ, aperture, lens
Thermal expansion	All	9”	9”	8”	6”	L	8”	temperature
Tilt of CCD chip	All	O(3”)?	O(3”)?	O(10”)	O(3”)?	Q	O(2”-5”)	telescope
Spot extraction	*All*	*1”*	*1”*	*1”*	*1”*	Q	*0.5”*	*spot quality, elongation*
Second spot	All	2”	2”	2”	2”	L	1”	field of view, reflections
Fit accuracy	*C.C.*	1”	1”	1”	4”	Q	*1”*	*number of LEDs*
Funnel-Diffusor	C.C.	1.3”	2”	>O(5”)?	4”	Q	O(2”)	mounting of funnel plate
Sum systematic	Star$_L$	19”	11”	15”	10”	Q	7/9/15”	(1/6/12 months after model)
Sum systematic	C.C.	27”	10”	15”	8”	Q	8”	
Sum systematic	**Model**	31”	15”	21”	13”	L	**11/13/17”**	(1/6/12 months after model)
Sum statistical	Star$_L$	8”	7”	12”	8”	Q	5”	
Sum statistical	C.C	7”	3”	5”	5”	Q	3”	
Sum statistical	**Model**	11”	7”	13”	9”	Q	**5”**	
Model accuracy		~10”	~10”	~10”	~10”			number of pointing runs

Table 4.2: **Contributions of individual error sources.** Statistical errors are written in italics.

5 Precision Pointing

Knowing the diversity of errors presented in previous chapter, a new approach is necessary to minimize the systematic errors of the pointing direction. Many influences have been shown to depend on time, so it would be favourable to measure as much information as possible in parallel with observations.

During observation runs, it is possible to use the SkyCCD to get information on misorientation and tilting, and the LidCCD to measure the camera location including the deformation of masts or differences from opening the camera lid. But it is not possible to detect the image of stars in the focal plane in observation run, so some model derived from reference runs is still needed.

Many of the effects described before affect both CCDs, so their relative behaviour can be expected to be much more stable than deformations of the whole telescope. A model that only describes the relative differences between the CCD cameras is valid for longer time periods and can be used to predict the position of reflected stars in the LidCCD from the stars seen in the SkyCCD. This holds, as long as mirror and dish deformations can be assumed reproducible.

5.1 Procedure

In parallel to γ-ray observations, images from stars in the field of view of the SkyCCD provide information about the telescope orientation relative to the sky. The spots in the SkyCCD are fitted to the star positions in the observation direction and a mis-pointing vector for the SkyCCD is determined (see figure 5.1).
This SkyCCD mis-pointing needs to be translated into a mis-pointing for the Cherenkov camera, that corresponds to the offset of the mirrored sky in the focal plane from the nominal observation position (figure 5.2). The correlation between those two shifts depends on the telescope altitude, azimuth and environment temperature. It should be noted, that in addition to the misorientation of the telescope, this camera mis-pointing is affected by the bending of the dish, but not the deformation of the camera masts.

When the mis-pointing between nominal and actual location of the observation direction in the focal plane is known, camera centre information from the LidCCD is applied in a third step to determine the shift of the observed sky to the position of

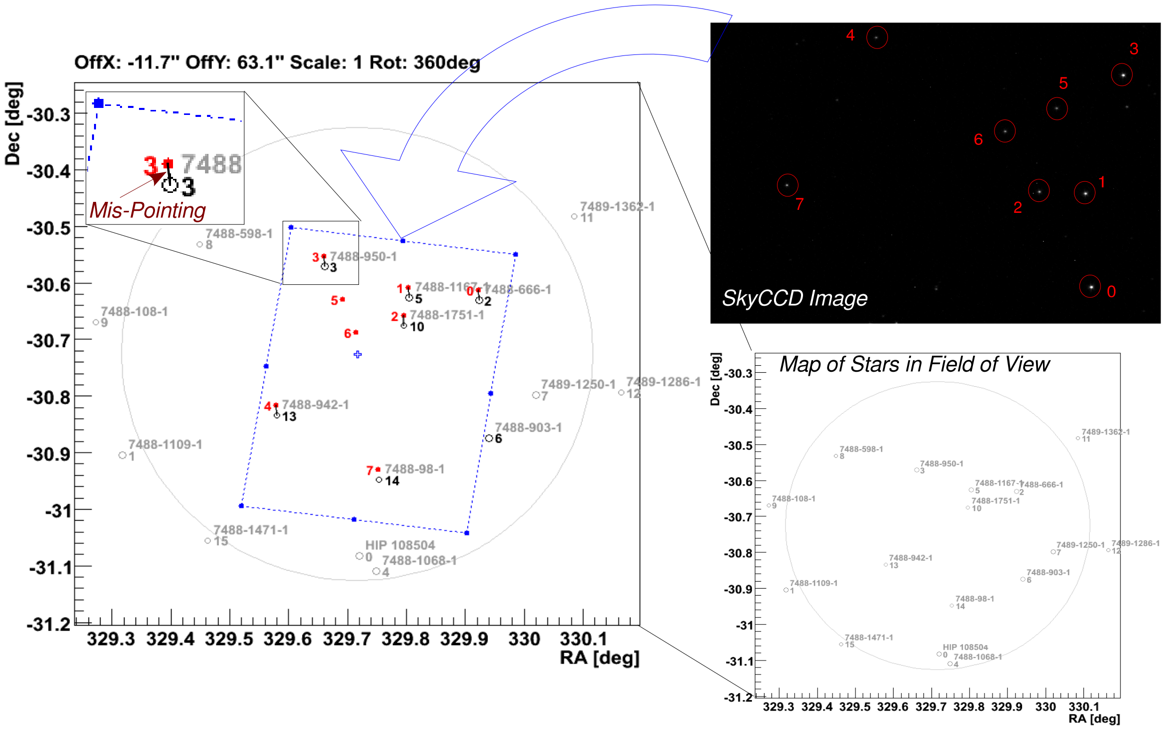

Figure 5.1: **Determination of the SkyCCD mis-pointing.** Illustration of the procedure computing the mis-pointing seen in the SkyCCD. Spots are extracted from the SkyCCD image and transformed into RA-Dec using the nominal pointing direction of the telescope. The spots are matched to observable stars from the Tycho and Hipparcos catalogue using an iterative selection procedure. A χ^2-fit determines the deviation of the whole set.

the Cherenkov camera. This shift is computed for each LidCCD image and can be applied to the image parameters of corresponding Cherenkov data.

Model Creation

The critical step of the procedure described above is the transformation of a mis-pointing measured in the SkyCCD to the corresponding shift on the camera lid. The connection between the two systems can be determined from reference pointing runs as used for the standard pointing approach. In those runs, the LidCCD mispointing can be measured as the distance between the image of the tracked star and the nominal centre of the LidCCD field of view. The SkyCCD mis-pointing is again computed from the difference between the projected star image and its nominal coordinate. Figure 5.3 shows the correlation between the star positions in the two CCD cameras.

It was seen that the average corrections created with this model drift over time, while the overall dependencies of the model parameters described below don't change signif-

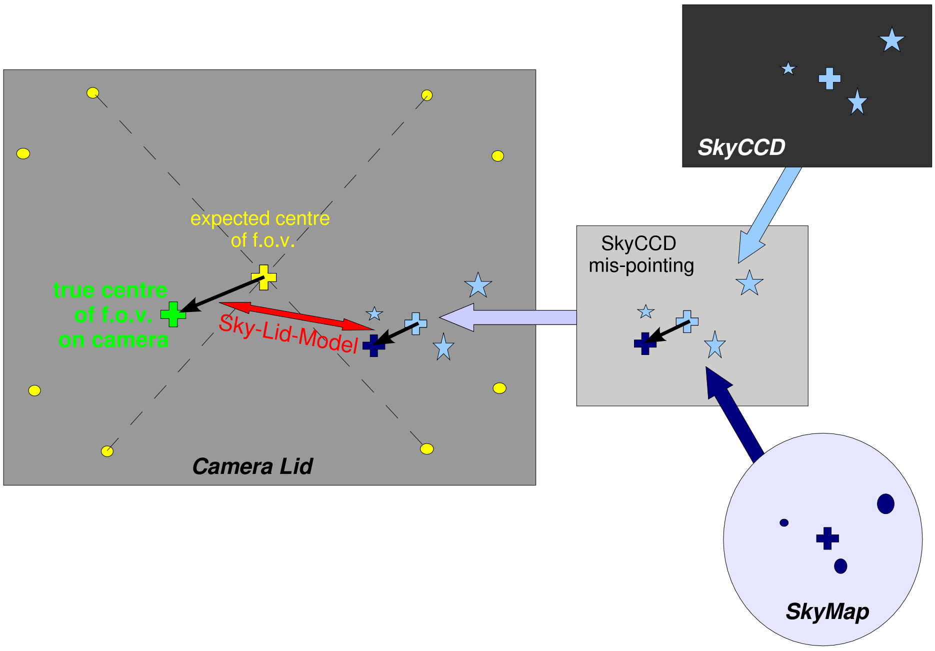

Figure 5.2: **Precision pointing in observation runs.** The figure illustrates the concept of the Sky-Lid-Model. In observation runs, the spots seen in the SkyCCD are matched to stars in the field of view (f.o.v) as described in figure 5.1. The observed SkyCCD mis-pointing and the Cherenkov camera mis-pointing between the centre of the camera (expected centre of f.o.v.) and the location of the target observation position (true centre of f.o.v. on camera) are connected through the Sky-Lid-Model

icantly. This quality allows to use a large set of pointing runs for the accurate creation of a model and apply the information on the temporal evolution independently.

The model is created in several steps that are demonstrated in figure 5.4:

1. a linear correlation between the two values in azimuth and altitude is fitted. The following corrections apply to the residuals of this fit.
2. the altitude dependence of the residuals is mainly caused by dish bending and fitted with a sine function:

$$\delta_{Az/Alt} = p_0 + p_1 * sin(Alt + p_2) \tag{5.1}$$

3. the azimuth dependence of the corrected residuals is fitted to a sine function like equation 5.1.
4. a linear dependence on the outside temperature is corrected.
5. the temporal stability of the previous modeling steps allows to use the residuals of each calibration period to the combined model to account for time evolution

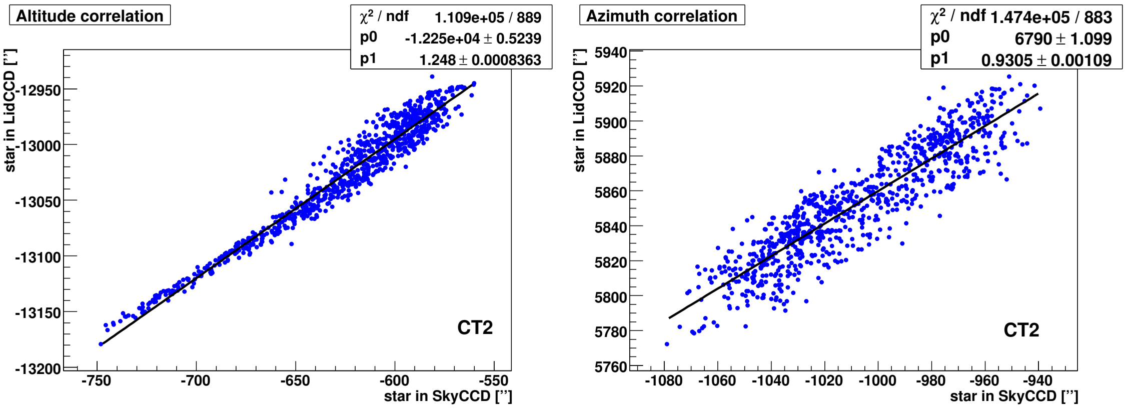

Figure 5.3: **Correlation between Sky- and LidCCD.**

(divided by maintenance work on one of the CCD cameras). Figure 5.5 demonstrates that the residuals of the model follow a Gaussian distribution with a typical RMS of the between 3" and 6.4" (average: 4") depending on the sky coverage of the data set. The mean deviation within one pointing calibration period is the last parameter of the model and applied as a shift to the data.

5.2 Investigation of Remaining Systematic Errors

The new approach eliminates most instrumental error sources presented in the previous chapter: all effects changing the orientation of the telescope or caused by differences in the atmosphere or the refraction model are ineffective due to the online measurements with the SkyCCD, while the LidCCD covers mast- and camera effects. However, the observed hysteresis is reduced, but not removed (see appendix D for details) and dish behaviour variations might still cause a statistical spread in the data.

Most methodic errors are still valid, but the introduction of a temperature dependent term into the model cancels the largest influence on the overall systematic error (the camera centre is measured with correct temperature). The spot extraction error was derived from an absolute error in CCD pixels, therefore it has to be reduced to 17% for the SkyCCD according to the better resolution of the camera and becomes irrelevant. The image of the sky is not symmetric, so an estimate about the optical aberration of the SkyCCD lens has to made, but since stars of different positions on the CCD chip will be combined in the analysis, the error becomes statistical.

In total, 6 of the 17 error sources in table 4.2 do not apply to the precision pointing approach and two are reduced significantly. Table 5.1 presents the remaining errors in a comparable way to table 4.2. The error of the entire experiment can now be stated as ±5" (statistical) ±6" (systematical).

Effect		CT1	CT2	CT3	CT4	Com.	Δ_{system}	remarks
Instrumental errors								
Misorientation	$\text{Star}_{L,S}$	-	-	-	-	Q	-	
Tracking	$\text{Star}_{L,S}$	-	-	-	-’	L	-	
Refraction model	$\text{Star}_{L,S}$	O(1”)	O(1”)	O(1”)	O(1”)	L	O(1”)	reduced to shower-star difference
Refraction	*$\text{Star}_{L,S}$*	*O(2”)*	*O(2”)*	*O(2”)*	*O(2”)*	*L*	*O(2”)*	*alt, λ, atmosphere*
Telescope tilting	$\text{Star}_{L,S}$	-	-	-	-	Q	-	
Mast Bending Residuals	*C.C.*	-	-	-	-	*Q*	-	
Dish Bending	*Star_{L}*	*8”*	*6”*	*12”*	*7”*	*L*	*8.4”*	*telescope*
Opening the lid	C.C.	-	-	-	-	L	-	
Hysteresis	$\text{Star}_{L,S}$	15”	2”	2”	6”	L	”	modified according to App.D
Methodic errors								
Optical aberrations	*Star_{S}*	*2”*	*2”*	*2”*	*2”*	*Q*	*1”*	*λ, aperture, lens*
Thermal expansion	All	-	-	-	-	L	-	model parameter
Tilt of CCD chip	C.C.	O(3”)	O(3”)	O(10”)	O(3”)	Q	O(2”-5”)	
Tilt of SkyCCD chip	Star_{S}	O(2”)	O(2”)	O(2”)	O(2”)	Q	O(1”)	
Spot extraction	*All*	*1”*	*1”*	*1”*	*1”*	Q	*0.5”*	*spot quality, elongation*
Second spot	All	2”	2”	2”	2”	L	1”	field of view, reflections
Fit accuracy	*C.C.*	1”	1”	1”	4”	Q	*1”*	*number of LEDs*
Funnel-Diffusor	C.C.	1.3”	2”	>O(5”)?	4”	Q	O(2”)	mounting of funnel plate
Sum systematic	$\text{Star}_{L,S}$	18”	4”	4”	7”	Q	5”	
Sum systematic	C.C.	4”	4”	11”	7”	Q	4”	
Sum systematic	**Model**	19”	6”	12”	9”	Q	**6”**	
Sum statistical	$\text{Star}_{L,S}$	8”	7”	13”	8”	Q	5”	
Sum statistical	C.C	2”	2”	2”	4”	Q	2”	
Sum statistical	**Model**	8”	7”	12”	9”	Q	**5”**	
Model accuracy		$\sim$6”	$\sim$6”	$\sim$6”	$\sim$6”			number of pointing runs

Table 5.1: **Contributions of individual error sources for Precision Pointing.** Statistical errors are written in italics.

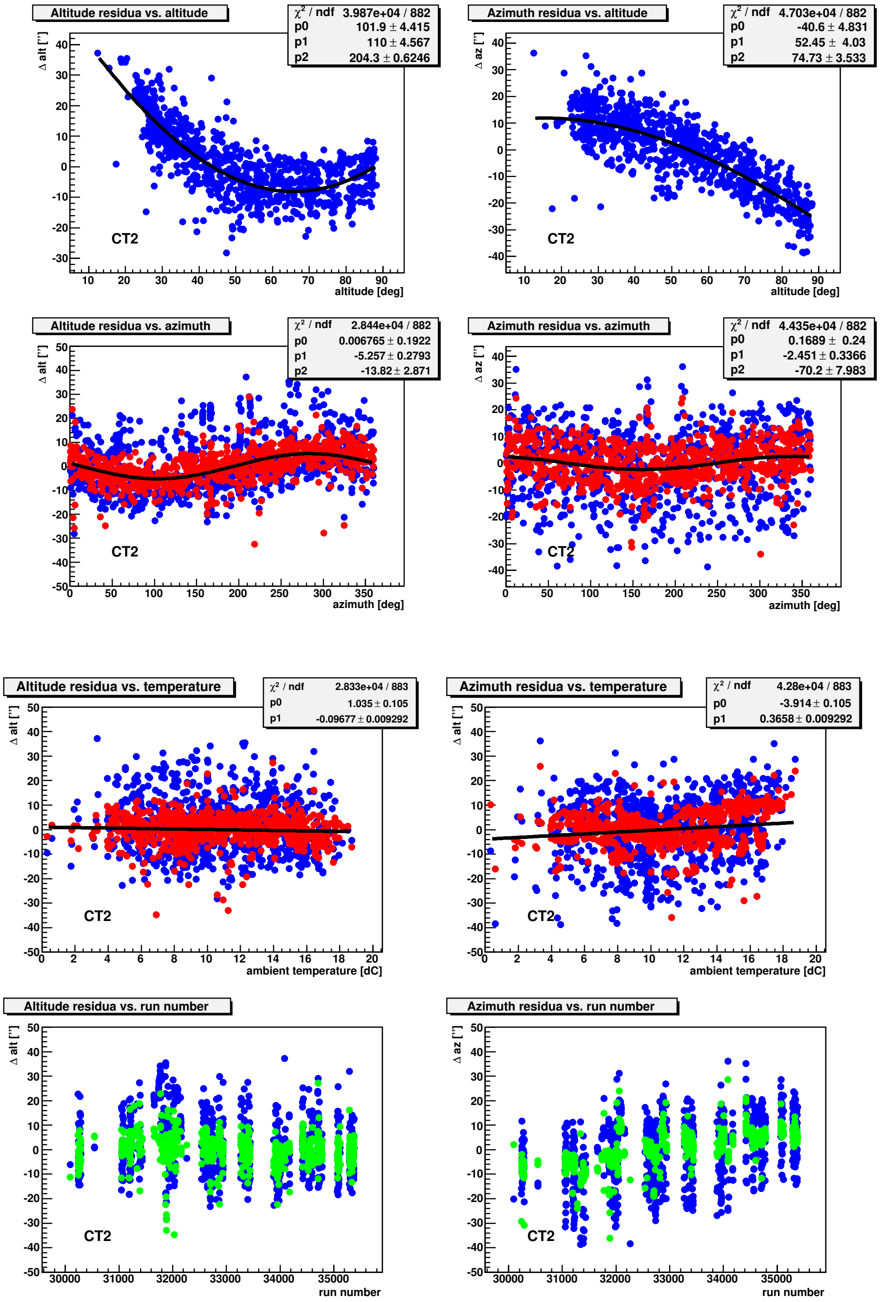

Figure 5.4: **Steps in the creation of the Sky-Lid pointing model.** The different modeling steps (2.-5.) for the residuals from a linear correlation are shown for the CT2 pointing data from January to October 2006. The left and right columns refer to altitude and azimuth residuals, the upper images show the altitude dependence of the residuals, the row below the azimuth dependence, and below that row the temperature dependence with blue and red points indicating data before or after the previous correction steps. The bottom row shows the remaining drift of the residuals in 2006, with blue data points for uncorrected residuals and green points including all corrections.

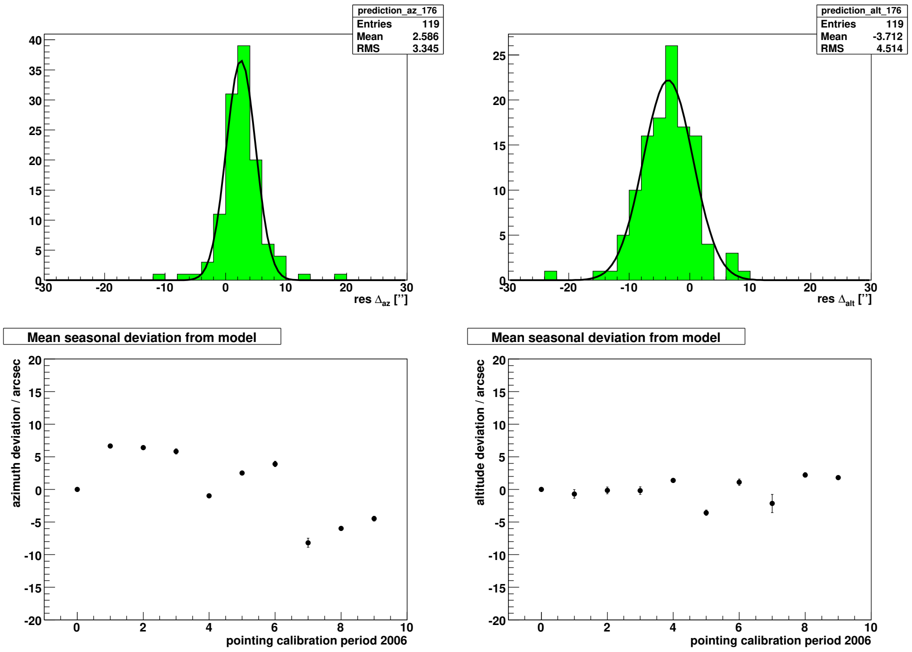

Figure 5.5: **Temporal evolution in the Sky-Lid model** in different moon periods of 2006. The first two histograms show the distribution of azimuth and altitude residuals to the model within one pointing calibration period, the lower two plots present the temporal development of the mean shifts in 2006.

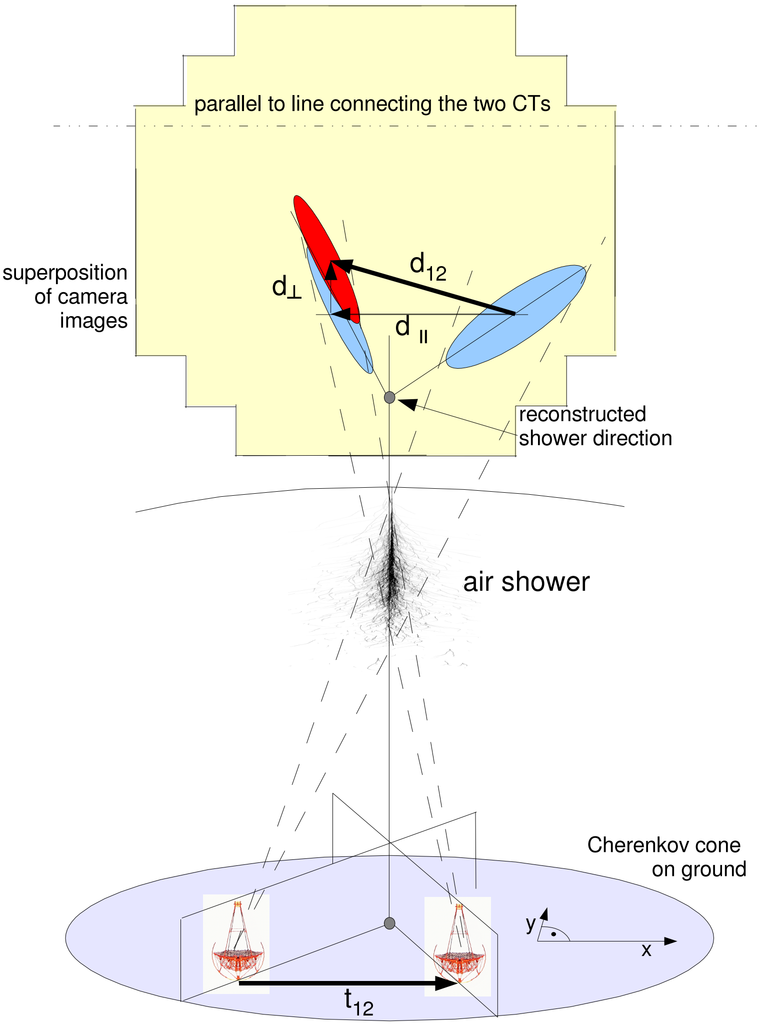

Figure 5.6: **Stereoscopic observation.**

5.3 Independent Test using Shower Images

To see the effect of this improvement, independent pointing check procedures with a better resolution than the method described in chapter 3.4 are needed. Stereoscopy provides such an additional check of the pointing accuracy using a technique described in [Gil04]. It is based on the geometrical correlation between relative telescope positions and the images seen of the same shower: the line connecting the centres of gravity in the overlaid images of two telescopes is parallel to the line connecting the telescope locations on the ground. This can be explained with the help of figure 5.6:
First of all, assume that two telescopes pointing to zenith observe the same vertical shower halfway between them. The vector connecting the telescopes $\vec{t}_{12}$ can be chosen along the x-axis. Then the overlaid shower images would appear as ellipses pointing toward each other on the x-axis.
If the impact point of the shower axis is now moved along the y-axis, both shower im-

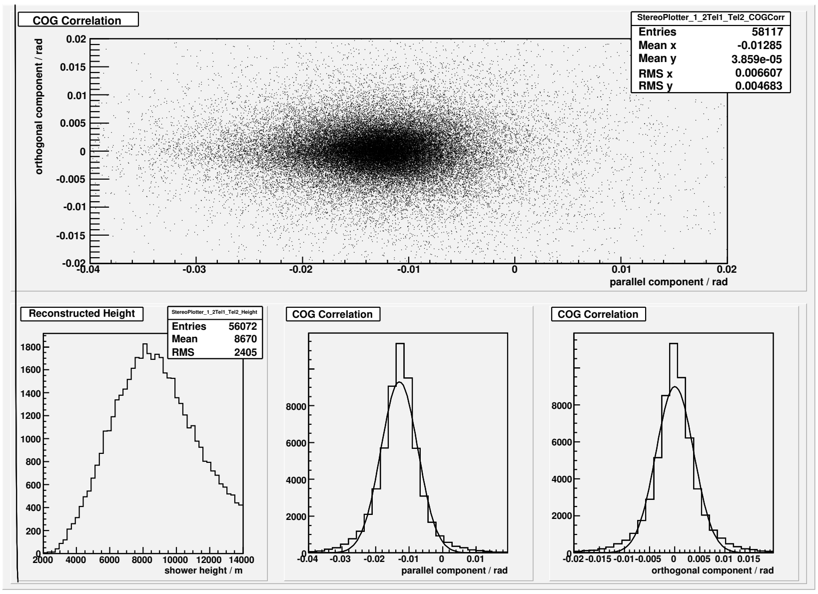

Figure 5.7: **Independent Test using Stereo Shower Images.** The centres of gravity of two Hillas ellipses imaging the same shower seen by CT1 and CT2 are superimposed and subtracted. The difference vector has a non-zero component parallel to the line connecting the two telescopes that is influenced by the height of the shower in the atmosphere and a perpendicular component that should in average be zero if the two cameras are correctly superimposed. In this example, the average orthogonal distance is 8 ± 4", so not consistent with zero.

ages would incline towards the reconstructed shower direction, but because they are still at the same distance from the shower, the difference vector $\overrightarrow{d}_{12}$ between the centres of gravity would certainly remain parallel to $\overrightarrow{t}_{12}$. The same is valid for different observation altitudes perpendicular to $\overrightarrow{t}_{12}$.

The vector $\overrightarrow{d}_{12}$ can be split into a component parallel and perpendicular to $\overrightarrow{t}_{12}$. While the length of the parallel component depends on the height of the observed shower, a non-vanishing orthogonal component indicates an error in the assumed telescope geometry. Depending on the source of this error, the effect varies with azimuth or shows a constant shift:
A constant shift might arise from a wrong determination of $\overrightarrow{t}_{12}$ and indicate that:

- both cameras are rotated by the same amount,
- the horizontal telescope position is wrong for one or both telescopes and/or
- the array orientation relative to the geographic north is not determined correctly.

This method works only if averaged over the whole field of view, strong sources or asymmetric wobble distributions may cause problems. A selection of nearly aligned

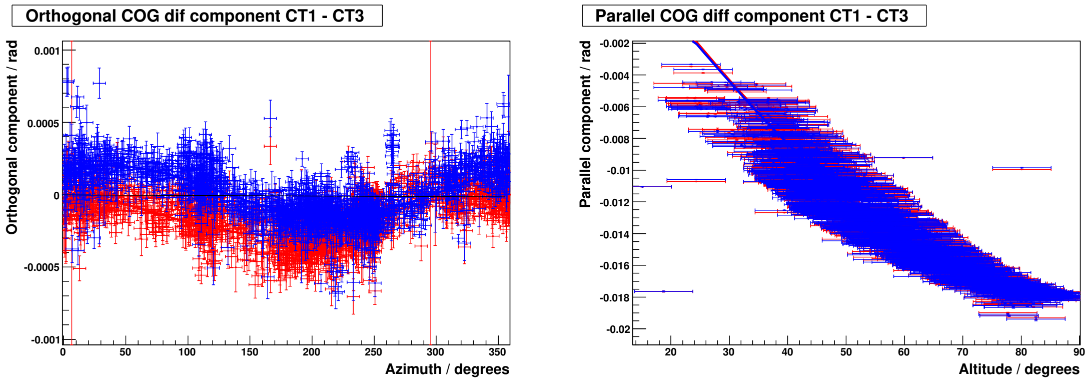

Figure 5.8: **Comparison of stereo event deviation for different pointing procedures** on the example of CT1-CT3 with all four-telescope runs from 2005 and 2006 that qualify for precision pointing (1890 runs). The altitude dependence of the parallel component of $\overrightarrow{d}_{12}$ (right image) is not changed by the pointing procedure.

shower images reduces the error due to different image shapes. For the analysis below, only events with less than 3° angle between the reconstructed shower axes were selected.

Table 5.2 presents the average offsets of the vertical component for the different telescope combinations and pointing schemes. It can be seen that the Precision Pointing yields smaller deviations that become consistent with zero in all cases.

	Standard Pointing	Sky-Lid Pointing
CT1-CT2	1.9” ± 10”	1.8” ± 9”
CT1-CT3	-29.2” ± 14”	-1.3” ± 15”
CT1-CT4	-9.4” ± 10”	-2.3” ± 10”
CT2-CT3	-23.1” ± 10”	-2.5” ± 10”
CT2-CT4	1.9” ± 14”	3.5” ± 14”
CT3-CT4	-11.2” ± 10”	3.6” ± 10”

Table 5.2: **Average Offset.** Average of all 1980 runs in 2005 / 2006 with CCD data for all four telescopes. The given error is the average error on the mean for the values of individual runs.

However, the spread is not randomly distributed but shows a dependence on azimuth as seen in figure 5.8 that implies an error in the merging of the two camera images:

- the determination of the relative camera centres are incorrect and/or
- the relative telescope height between the two CTs is erroneous.

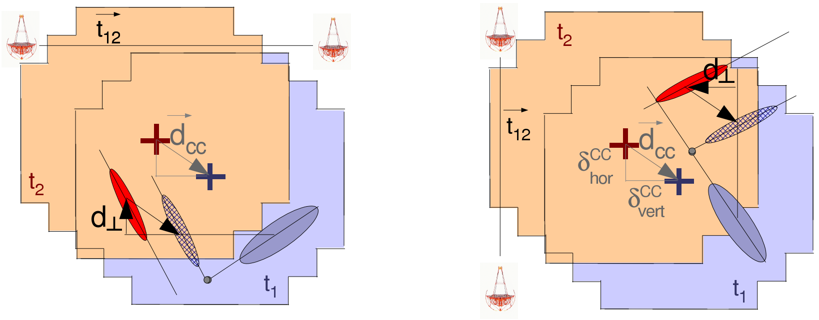

Figure 5.9: **Influence of the telescope orientation on the orthogonal stereo offset** demonstrated for two telescope configurations. When the telescopes are observing in a direction perpendicular to $\vec{t}_{12}$ (left image), $d_\perp$ is determined by the vertical component of the distance between the two camera centres.

The fit parameter values of an azimuth dependence like

$$\vec{d}_{12} = P_0 + P_1 * \sin(Az - P_2) \tag{5.2}$$

with offset P_0, amplitude P_1 and phase P_2 are given in table 5.3. It can be seen that the constant offset is reduced significantly by the new pointing scheme, and that the amplitude of the sinusoidal effect is not reduced for all combinations and even increases in some cases.

The phase contains information on the direction of the offset. A vertical error in one camera centre will have the largest influence on $\vec{d}_{12}$ when the observation direction is perpendicular to $\vec{t}_{12}$, only a horizontal error is relevant for parallel alignment (figure 5.9). Therefore, with the knowledge of the azimuth at which the telescopes are aligned, one can determine the relative horizontal and vertical camera offsets between them. Table 5.4 shows the implied offsets derived with this method.

There appears to be a problem with the camera centre of CT3, and since no funnel plate measurements (see section 4.2.3) could be performed on CT3, the error on the camera offset could be larger than assumed. It is also possible, that the error does not arise from a problem on the individual telescope, but rather the relation to the rest of the array.

While the test still unveils significant discrepancies for the relative camera centres, especially when CT3 is part of the studied pair, the average systematic offset seen with standard pointing is reduced by a factor of three to five to below 4” when applying the precision pointing procedure.

To reliably check the influence of this problem on the final pointing accuracy, Cherenkov data from strong point-like γ-ray sources with known position are used. An ideal candidate is the AGN PKS 2155-304, which was observed by H.E.S.S. in several campaigns

CTs	Standard			Sky-Lid		
	Ampl. / ”	Offset / ”	Phase /°	Ampl. / ”	Offset / ”	Phase /°
1-2	13.8±0.2	2.7 ± 0.2	-77.0 ± 1.3	4.0± 0.2	-0.1 ± 0.2	-67.7± 4.2
1-3	29.4±0.4	-27.9± 0.3	-102.9 ± 0.8	36.2± 0.4	5.1 ± 0.3	-54.5± 0.7
1-4	-12.6±0.3	-29.0 ± 0.2	28.3 ± 1.0	32.0± 0.3	-2.0 ± 0.2	-102.0± 0.6
2-3	31.1±0.2	-12.4± 0.2	242.6 ± 0.3	37.9± 0.2	-0.3 ± 0.2	242.9± 0.3
2-4	-12.3±0.4	2.0 ± 0.3	49.0 ± 1.5	-13.4± 0.5	0.9 ± 0.2	-5.1± 1.4
3-4	-21.0±0.3	-13.5 ± 0.2	62.4 ± 0.8	27.0± 0.3	4.1 ± 0.2	12.3± 0.6

Table 5.3: **Sine fit to azimuth dependence of offset.**

CTs		Standard		Sky-Lid	
	Az($\overrightarrow{t}_{12}$)/°	Δ_{hor} / ”	Δ_{vert} /”	Δ_{hor} / ”	Δ_{vert} /”
1-2	-45.2	7.3	-11.7	1.0	-3.9
1-3	-89.9	6.7	-28.7	-21.0	-29.6
1-4	45.9	7.6	17.1	1.6	19.5
2-3	45.9	-3.6	12.1	17.5	26.8
2-4	-89.8	8.1	-9.2	13.4	1.2
3-4	-45.0	20.0	-6.3	-22.8	-14.6

Table 5.4: **Relative differences of the camera centres**

between 2004 and 2006. Detailed systematic tests have been performed on influences on the position of this source that can be found in the next chapter.

6 Results for Gamma Ray sources

The previous chapters discussed individual effects measured with the CCD cameras. Now it remains to be shown that the claimed improvements actually have an effect on the position of a measured source.

The analysis steps needed to determine the source location are introduced in the first section of this chapter. It is followed by a comparative analysis considering several influences on the pointing accuracy and their impact on standard and precision pointing. In the final section, the γ-ray signals for several sources are analysed using the new precision pointing algorithm. Following the main theme of this work, the analysis concentrates on the reconstructed position of the sources.

6.1 Analysis Procedure

The important analysis steps used to compute the measured source locations will be given in this section. The general procedure is presented in [Aha06e], only topics with special relevance for pointing will be covered in more detail. A summary of the additional requirements to enable the usage of precision pointing will be given in section 6.1.1. Apart from the correct telescope orientation, two analysis steps are needed to determine the location of a γ-ray source from the recorded shower images: the reconstruction of the arrival direction for an individual γ-ray candidate and the correct fit to the superposition of many events. These two topics will be discussed in sections 6.1.2 and 6.1.3, respectively.

6.1.1 Run Selection

In contrast to the standard pointing scheme, precision pointing requires the successful operation of both CCD cameras during each observation run. This condition together with not very stringent sanity checks introduces the following additional selection criteria:

- the run contains at least five SkyCCD pictures showing stars.
- the run contains at least five LidCCD pictures showing a minimum of seven LEDs.

- the spread of the azimuth or altitude correction for the SkyCCD does not exceed 10” RMS.
- the spread of the camera centre does not exceed 3” RMS in the horizontal or 5” RMS in the vertical component.

For comparison, the following studies only use data that qualifies for the new approach. Most tests will be done only with runs where all four telescopes pass the cuts. 103 of the original 150 runs on PKS 2155-304 in 2005 and 2006 passing the regular selection cuts for all telescopes fulfill this criterium. Most runs in this list were excluded by the first cut, because few possible guiding stars exist within the SkyCCD field of view around the AGN. The fraction of 81% passing the SkyCCD cut e.g. increases to 98% for the data on the X-Ray binary LS 5039 located in the Galactic plane.

Systematic influences are identified by dividing the runlist into several sub-sets taken under different physical conditions. The events of these data sets are processed with the standard H.E.S.S. analysis procedure using a Hillas analysis with "standard cuts" and the "ring-background model" as described in [Aha06e].

6.1.2 Direction Reconstruction

To reconstruct the direction of a shower in stereoscopic observation, the major axes of shower images in multiple cameras are intersected (see figure 6.1). An error of the method can be calculated if more than two telescopes detected the shower and the intersection point is over-determined. In this case, the resulting intersection points are weighted with the sine of the intersection angle to take into account that maximum precision is achieved from perpendicular intersection lines. This method corresponds to algorithm 1 in [HJK99].

Advanced direction reconstruction The paper also presents more advanced methods like algorithm 3 (also shown in figure 6.1), which uses the connection of the shape (explicitly *width/length*) of the ellipse with the distance between the centroid of the shower image and the image of the source (distance d in figure 6.1). For each telescope, error ellipses for the source position are derived from Monte-Carlo simulations and then combined to locate the source. More information on the implementation of this method can be found in [Ber06]

Point Spread Function The apparent extension of a point source, the point spread function (PSF) of the experiment, depends on the zenith angle of the observation and the offset of the source to the centre of the field of view. It is a measure for the precision of our knowledge on the direction of individual γ-rays and determined from Monte-Carlo simulations. The improved direction reconstruction of algorithm 3 also reduces the size of the PSF. For the case of the selected runs on PKS 2155-304, algorithm 3 offers a reduction of the 68% containment radius by 7% to 0.101°.

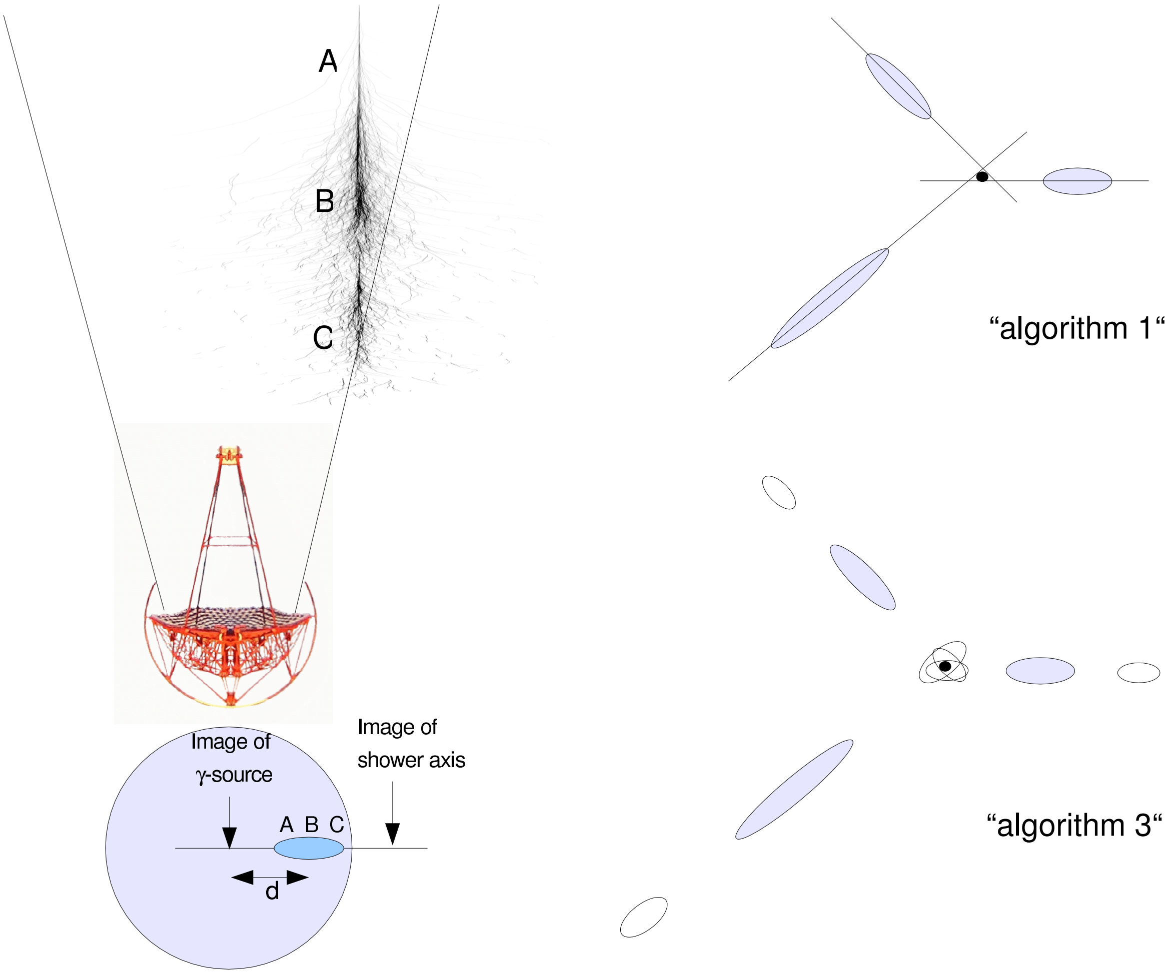

Figure 6.1: **Different direction reconstruction methods** according to [HJK99]. The left part of the image visualizes the connection between the shower and its image in the camera. The top right figure illustrates the standard reconstruction procedure, the intersection of extended major axes. The lower right figure presents the technique using the shape of the images. It may sometimes be referred to as *directionmaker*-procedure (DM) following the implementation nomenclature within the H.E.S.S. analysis framework.

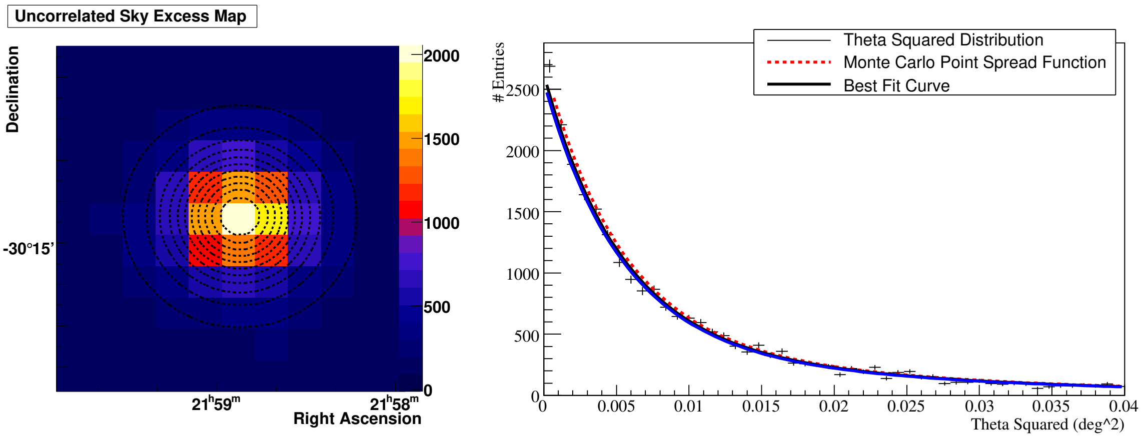

Figure 6.2: **Source Fit:** on the left, the central region of the γ-ray excess map of PKS 2155-304 and contours of the fitted two-dimensional PSF are shown, the right image shows the distribution of events as function of the squared angular distance from the fitted source position (θ^2). The fit matches the data and the simulated PSF for the assumed spectral index of 3.3.

6.1.3 Source Fitting Routine

Various methods are implemented to determine the source position from the arrival directions of all events in a set of runs. In general, one can either fit the histogram containing all events and make an assumption on the shape of the background or fit the uncorrelated excess map, a fine-binned histogram containing excess γ-ray events after bin-wise background subtraction (see figure 6.2).

The latter cannot be fitted with a log-likelihood procedure, because due to the background subtraction, its errors do not follow Poisson statistics which is assumed by this fitting routine. Therefore the originally uncorrelated excess map has to be rebinned until signal bins contain enough events to perform a chi-squared fit.

The statistical accuracy of point source locations is given by the limited angular resolution of the experiment (PSF) and the available γ-ray statistics. Figure 6.3 shows the expected position error as a function of the significance of the γ-ray excess. The figure can be read to show the range of significances for which the overall error is dominated by the error of the fit. Point sources up to significances around 50 are therefore not dominated by the pointing error.

In the following, the data are fit with the two-Gaussian profile reflecting the angular resolution for a given distribution of zenith angles and offsets.

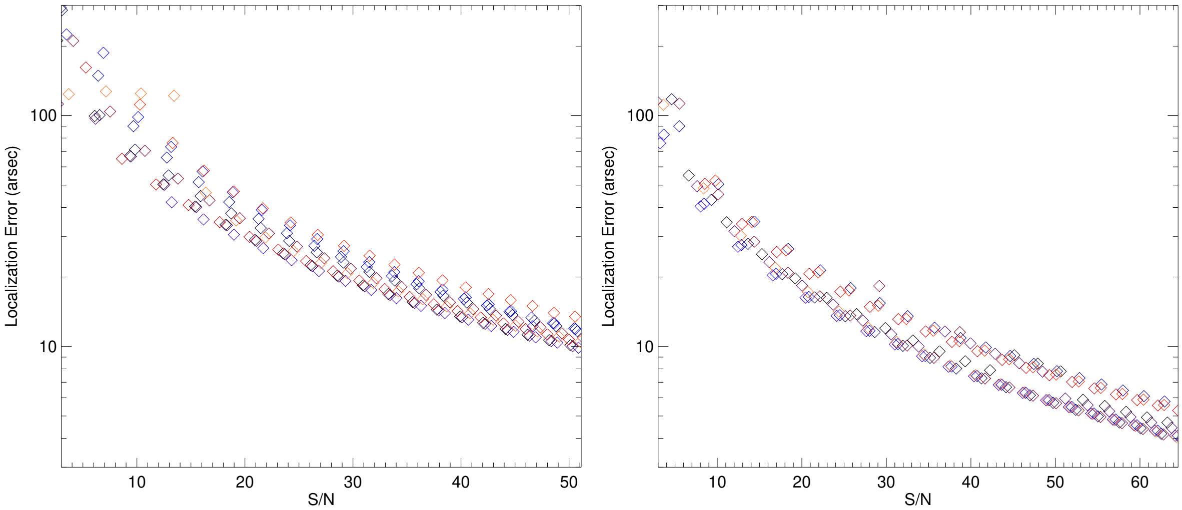

Figure 6.3: **Source Fit location error.** Preliminary (!) plot showing the statistical error due to the source fit to the PSF vs. significance of the signal for standard cuts (left) and hard cuts (right). Hard cuts select events with higher energy, and the improved direction reconstruction reduces the corresponding width of the PSF. Different coloured data points correspond to different absolute background values.

6.2 Influences on the Position of the Signal from PKS 2155-304

A direct comparison between the performance of the two pointing approaches presented in chapters 3 and 5 will be given to support the previous statements on the improved accuracy of the new model and to identify remaining problems. Figure 6.4 shows the deviation of the reconstructed source location from the known position of PKS 2155-304[1] in right ascension and declination for standard and precision pointing (black / red) as well as two different run selections. For this image, algorithm 1 was used to determine the shower direction. It can be seen that using precision pointing the offset of about 15” in declination with standard pointing is eliminated. With precision pointing, the target position agrees with the reconstructed source position within the stated systematic error of 6”.

The strong signal is not sensitive to reasonable changes of the binning or fit-range, but the "divide et impera"- technique used below to determine systematic influences results in data-sets with much smaller statistics, where these factors may become important.

The small difference between the results for runs where all four telescopes qualify for precision pointing and the data set including all possible observations in figure 6.4

---

[1] $(21^h58^m52.0651^5 RA/-30°13'32.118''Dec)$[CDS07] or $(329.7169°/-30.2256°)$

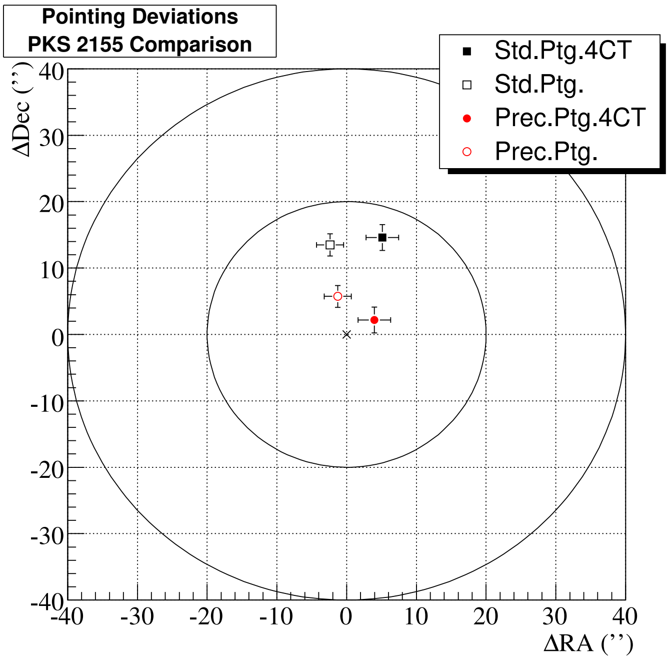

Figure 6.4: **Comparison of the two pointing approaches** with the standard direction reconstruction. The difference between the reconstructed source location and the position of PKS 2155-304 is shown (fit position - target position). Solid symbols indicate that the analysis was performed with runs where all four telescopes passed precision pointing criteria. Each point combines the direction of about 18 000 excess events. Open symbols mark the location derived from all runs, but ignoring individual telescopes that did not qualify for precision pointing in the analysis (about 22 000 excess events). A fit area of 1° diameter centered on the target position and a bin size of 0.05° were chosen for the fit of the excess map. The error bars represent the statistical error of the fit.

indicates a possible problem with the influences of individual telescopes. This will be discussed in the following chapter.

6.2.1 Individual Telescopes

Some of the error sources only affected one or two of the four telescopes. Therefore it is interesting to know if the reconstructed source position changes when a presumably problematic telescope is excluded from the analysis. The influence of individual telescopes depends on the observation position for non-zero zenith angles, because the array is effectively contracted by perspective and different telescopes gain different trigger probabilities and weights in the reconstruction.

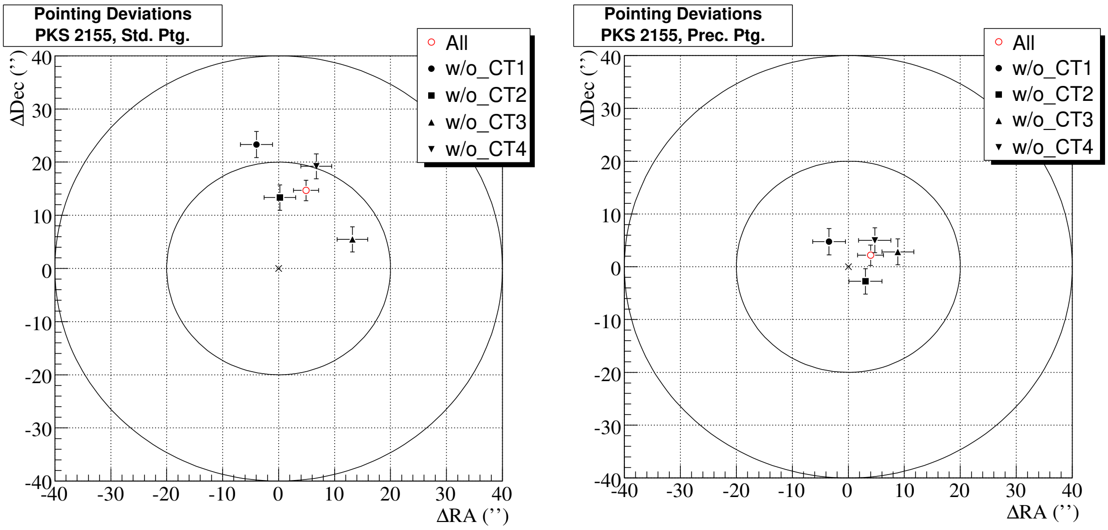

Figure 6.5: **Influence of individual telescopes.** One telescope at a time was artificially removed from the analysis of the same four-telescope runlist. The left image shows the comparison of the different reconstructed positions for standard pointing, the right image is the corresponding plot for precision pointing.

It can be seen in figure 6.5 that for both pointing methods the exclusion of one telescope yields a slightly different position.

The difference caused by the exclusion of individual telescopes creates an additional systematic error when runs with less than four telescopes passing the selection cuts are included in the analysis. For the analysed data on PKS 2155-304, 47% of the additional runs were processed without CT1 only, which explains the shift mentioned in the last chapter as a shift toward the position of the data point without CT1 in figure 6.5.

The improved direction reconstruction of algorithm 3 is expected to show a better behaviour in this regard, because the different relative projected distances are accounted for. Figure 6.6 repeats the test for this method showing a clear improvement. For the standard pointing method it can be seen that the largest influence indeed comes from CT3, as was expected from the systematic error. The combination of precision pointing and the improved direction reconstruction yields a perfect agreement between the measured γ-ray source and the location of PKS 2155-304 within statistical errors (1.4"±2.1"/1.1"±1.8"). For the rest of this analysis, algorithm 3 will be used.

6.2.2 Wobble Offsets

The data set was divided into the four Wobble directions (positive or negative 0.5° offsets in Right Ascension (RA) or Declination (Dec)), which yields information on

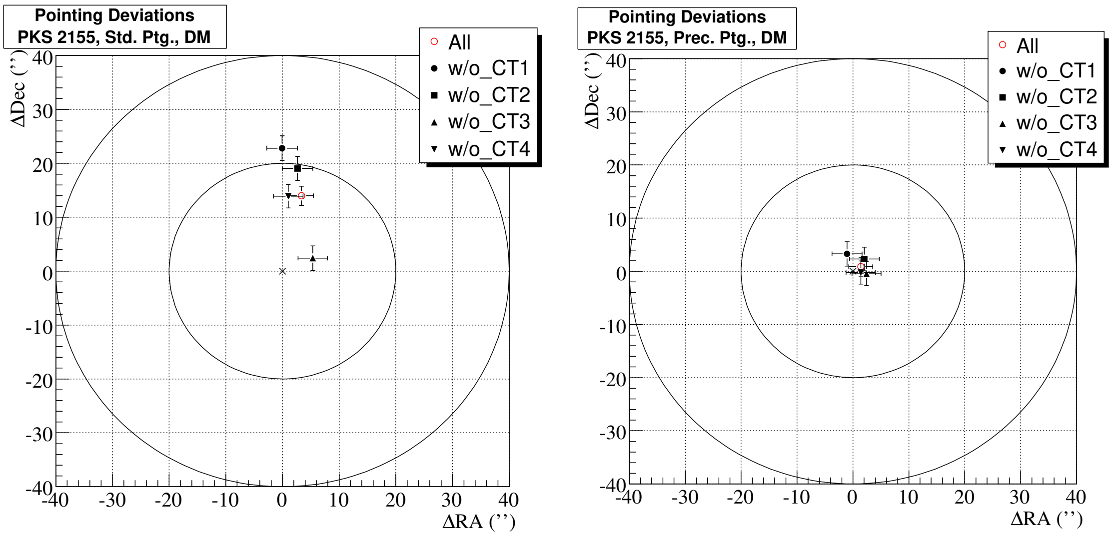

Figure 6.6: **Influence of individual telescopes with enhanced direction reconstruction:** results of the test shown in figure 6.5, now using algorithm 3.

those systematics sensitive to different regions of the sky. The offset changes between subsequent runs, therefore the data sets are to first order distributed homogeneously in time and observation direction.

The four sub-set data points for precision pointing in figure 6.7 are not completely coincident with each other, but agree within their given statistical errors. This confirms that no major mistakes are made in the identification of the stars in a given field of view. The larger pointing error seen for the positive RA Wobble direction is caused by the relatively void region of the sky for this observation position, which causes a large fraction of the runs to fail the pointing selection criteria for at least one telescope, thus giving a larger statistical error. The similarity of the behaviour in standard and precision pointing proves that the difference is not introduced by a faulty identification of an observed guiding star or its position determination.

6.2.3 Telescope Orientation

Many presented errors were influenced by telescope orientation. Inaccuracies of the model could be visible as different reconstructed positions depending on azimuth and altitude of the observation.

Since the path of the source on the sky does not vary much within an observation campaign, divisions in altitude and azimuth are correlated. Four altitude regions were chosen in the eastern and western hemisphere, hence following the rising or setting source. The observation policy of H.E.S.S. favours smaller zenith angles, therefore the number of events for the lower altitudes is small.

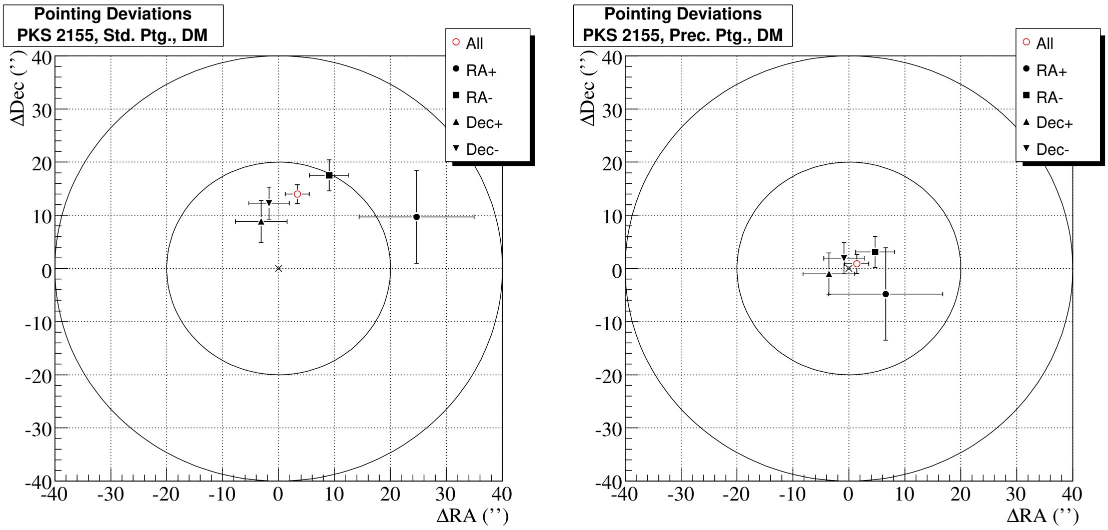

Figure 6.7: **The reconstructed source locations for runs taken with different Wobble Offsets** as well as the overall dataset are presented for standard (left) and precision pointing (right). The error bars indicate statistical errors only. Excess gamma events contained in the individual subsets: 985 (RA+), 6053 (RA-), 3850 (Dec+), 5974 (Dec-), 16868 (All). or significances 37 (RA+), 125 (RA-), 90 (Dec+), 118 (Dec-), 195 (All).

Figure 6.8 shows the source positions for runs pointing in different regions of the sky. The wide spread of the data points within the standard pointing scheme is reduced by the Sky-Lid approach, but not all points are coincident within their statistical errors, especially lower altitude observations of rising sources in the east appear systematically lower in declination.

The possible splitting between east and west observations could be related to the azimuth dependent superposition problems seen in chapter 5.3.

6.2.4 Atmospheric Conditions

In chapter 4, two major effects depended on atmospheric conditions: refraction and thermal expansion. The most important atmospheric parameter - the temperature - is a parameter of the new pointing scheme and should be corrected.

Figure 6.9 shows the reconstructed positions for subsets taken in different temperature bands. For standard pointing, the individual data points are not compatible within 1-σ errors. As expected, the spread of the data points is reduced for precision pointing, but a difference between the coldest and warmest nights can not be excluded. A difference could be explained by a temperature dependent error in the identification of the camera centre from the LEDs and the difference in refraction between starlight and Cherenkov light.

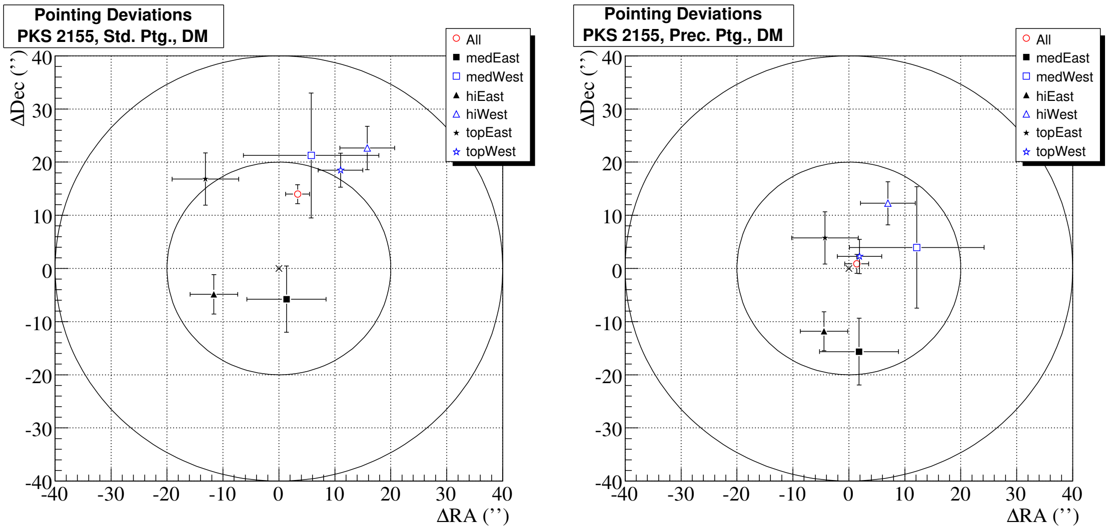

Figure 6.8: **Different Telescope Orientations:** the runs were divided according to their average azimuth (east-west) and altitude. The presented altitude bands are "medium"(30°<alt<50°),"high"(50°<alt<70°) and "top"(alt>70°)

6.2.5 Time Evolution

PKS 2155-304 is a highly variable source, therefore dividing the data set into intervals covering equal time periods produces points with very different statistical significance.

For the standard model, time dependent errors could induce an apparent movement of the source. A time dependence of the pointing model on the timescales needed to include enough statistics is not a large issue for precision pointing.

With an average temperature of 17.6°C (for comparison: average in 2006: 6.6°C) at least part of the shift could arise from the previously discussed temperature dependence. Also, all runs in 2005 have been taken in a narrow azimuth interval, therefore the effect could again be caused by the problems seen in chapter 5.3. The fact that the practically background free flare period does not show any offset could also indicate a problem with the background.

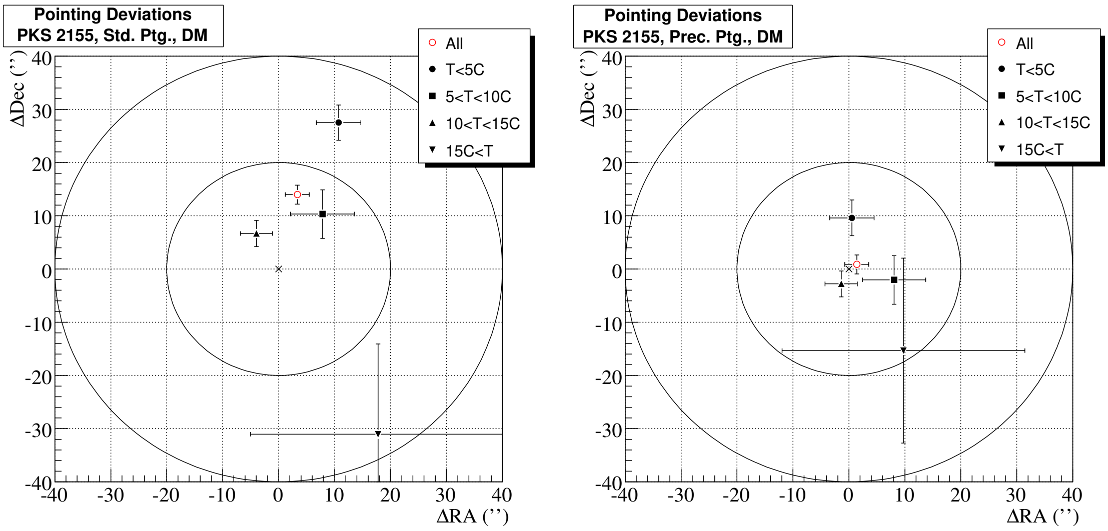

Figure 6.9: **The reconstructed source locations for runs taken with different Temperatures** as well as the overall dataset are presented for standard (left) and precision pointing (right).

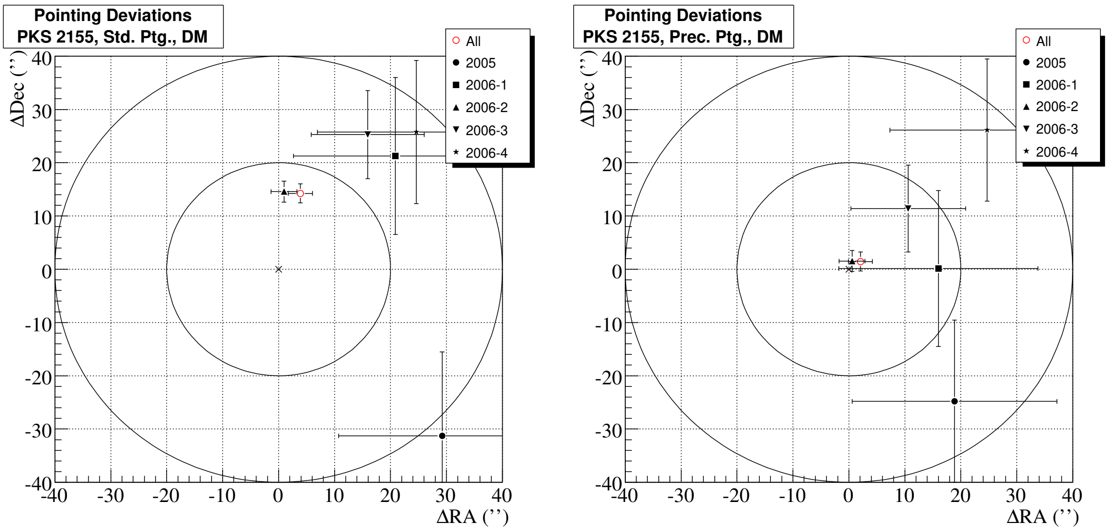

Figure 6.10: **The reconstructed source locations for runs taken in different Time periods**

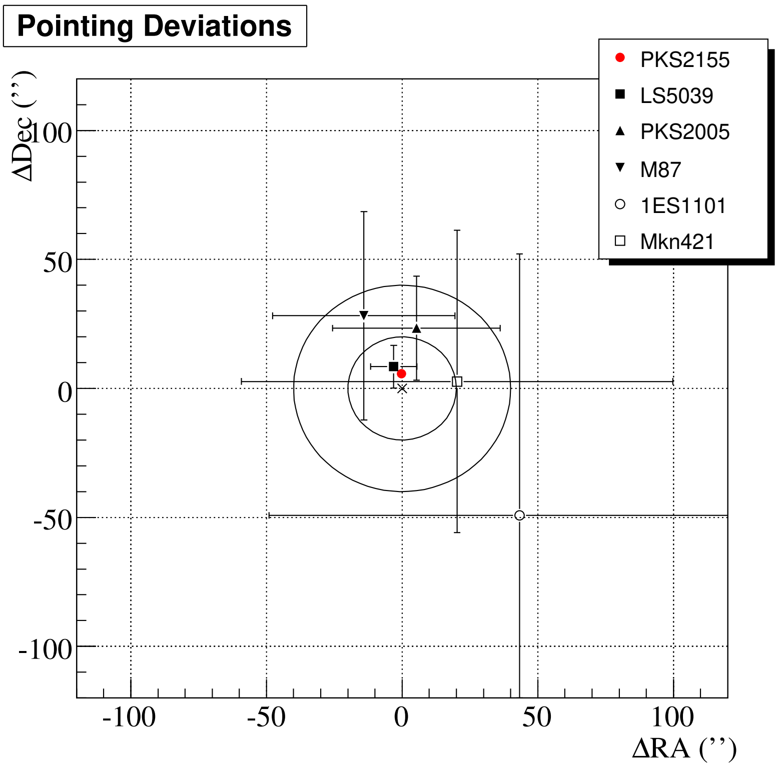

Figure 6.11: **Point Sources observed with H.E.S.S.**

6.3 Point Source Locations

The combination of algorithm 3 for the direction reconstruction and Precision pointing can determine the location of a γ-ray source with high accuracy for a large set of runs. H.E.S.S. observed several point sources sufficiently long in 2005 and 2006 to extract a position using the precision pointing algorithm. A small preliminary ensemble study of the reconstructed signal positions of those point sources observed with H.E.S.S. is shown in figure 6.11.

In addition to PKS2155-304[Aha05c], it includes the active galaxies PKS 2005-489[Aha05b], Markarian 421 [Aha05d], M 87 [Aha06c] and the high mass X-ray binary LS 5039 [Aha05a]. More information on the VHE signal from those sources can be found in the cited papers of the H.E.S.S. collaboration.

All six source locations are consistent with the coordinates of their counterparts from [CDS07]. This demonstrates that the pointing behaviour of the H.E.S.S. telescopes is well understood and that the experiment is capable to determine the location of a γ-ray source with a systematic error of 6". Of course, each source should be tested in more detail for systematical problems.

7 Summary

This work presents detailed systematic studies to understand the pointing of the H.E.S.S. instrument. A comprehensive set of measurements was performed to characterise the mechanical behaviour of the telescope structure and understand its long-term behaviour. A critical point in the analysis was the correct estimation of systematic errors arising from the analysis of CCD data.

The standard pointing procedure in H.E.S.S. using reference runs on stars is presented. The location of the star relative to the pixel matrix of the Cherenkov camera is recorded by a CCD camera and modeled to predict the dislocation for a given observation direction. The systematic error of this standard procedure is derived and an alternative approach is introduced that uses CCD images taken in parallel with the Cherenkov data. It was shown that this method reduces the systematic pointing error of the experiment to 6", which is the best pointing accuracy so far in the field of ground based γ-ray astronomy.

The validity of the given systematic error is tested on point sources of known position and dependencies of the source location on physical conditions are discussed. This new pointing procedure will be useful to identify γ-ray sources in regions with more than one possible counterpart like the Galactic Centre region.

Appendix

A Obtaining a Power-Law Spectrum

The following deduction of a power-law spectrum in energy from basic assumptions on the nature of the acceleration can be found in [KKZ97]. A particle with initial energy E_0 gains energy in several acceleration steps. If the gained energy ΔE is proportional to its energy ($\Delta E = \epsilon E$), after n steps it will carry

$$E_n = E_0(1+\epsilon)^n \tag{A.1}$$

Therefore,

$$n = \frac{\ln\left(\frac{E}{E_0}\right)}{\ln(1+e)} \tag{A.2}$$

steps are necessary to reach energy E.

If P_e is the escape probability in each acceleration step, the probability to remain in the acceleration process after n steps is (1-P_e)^n. This yields a fraction of $N(>E)$ particles with an energy above E according to

$$N(>E) \sim \sum_{m=n}^{\infty}(1-P_e)^m = \frac{(1-P_e)^n}{P_e} \tag{A.3}$$

Using equation A.2, one gets the power law distribution for particle numbers

$$N(>E) \sim \frac{1}{P_e}\left(\frac{E}{E_0}\right)^{-\gamma} \tag{A.4}$$

with

$$\gamma = \frac{\ln\left(\frac{1}{1-P_e}\right)}{\ln(1+\epsilon)} \tag{A.5}$$

B Focusing the LidCCD-Cameras

Due to the large aperture of the LidCCD, the manual focusing of a LidCCD camera can be a time-consuming process, and relying on the personal impression of sharpness is obviously not the ideal method to decide on the focus of the image. Tools have been implemented to

- make a quick comparison between images taken under identical lighting conditions: the program returns the largest intensity difference between neighbouring pixels.
- quantitatively determine the sharpness of an image (figure B.1): a pattern of black and white stripes is attached to the lid and imaged in the LidCCD. The intensity values along slices covering a transition between black and white areas are fitted with a Fermi-type function like

$$I(x) = A + B * \frac{1}{1 + e^{\,(x-x_0)/\Delta}}. \tag{B.1}$$

The second technique was used to compute the values of Δ in equation B.1 for different regions on the CCD chip of the four LidCCDs (figure B.2). The values for Δ in the central region of the CTs are between 0.63 pixels (CT4) and 0.83 pixels (CT4).

They can be converted into an RMS to disentangle the focusing of the CCD camera from the PSF of the telescope. The intrinsic PSF of CCD camera and lens ranges from 1.1 to 1.4 CCD pixels.

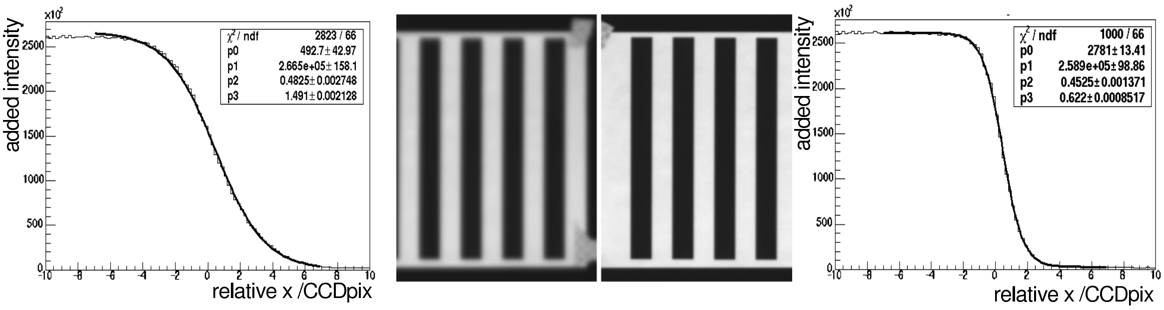

Figure B.1: **Image sharpness** determined for two example images.

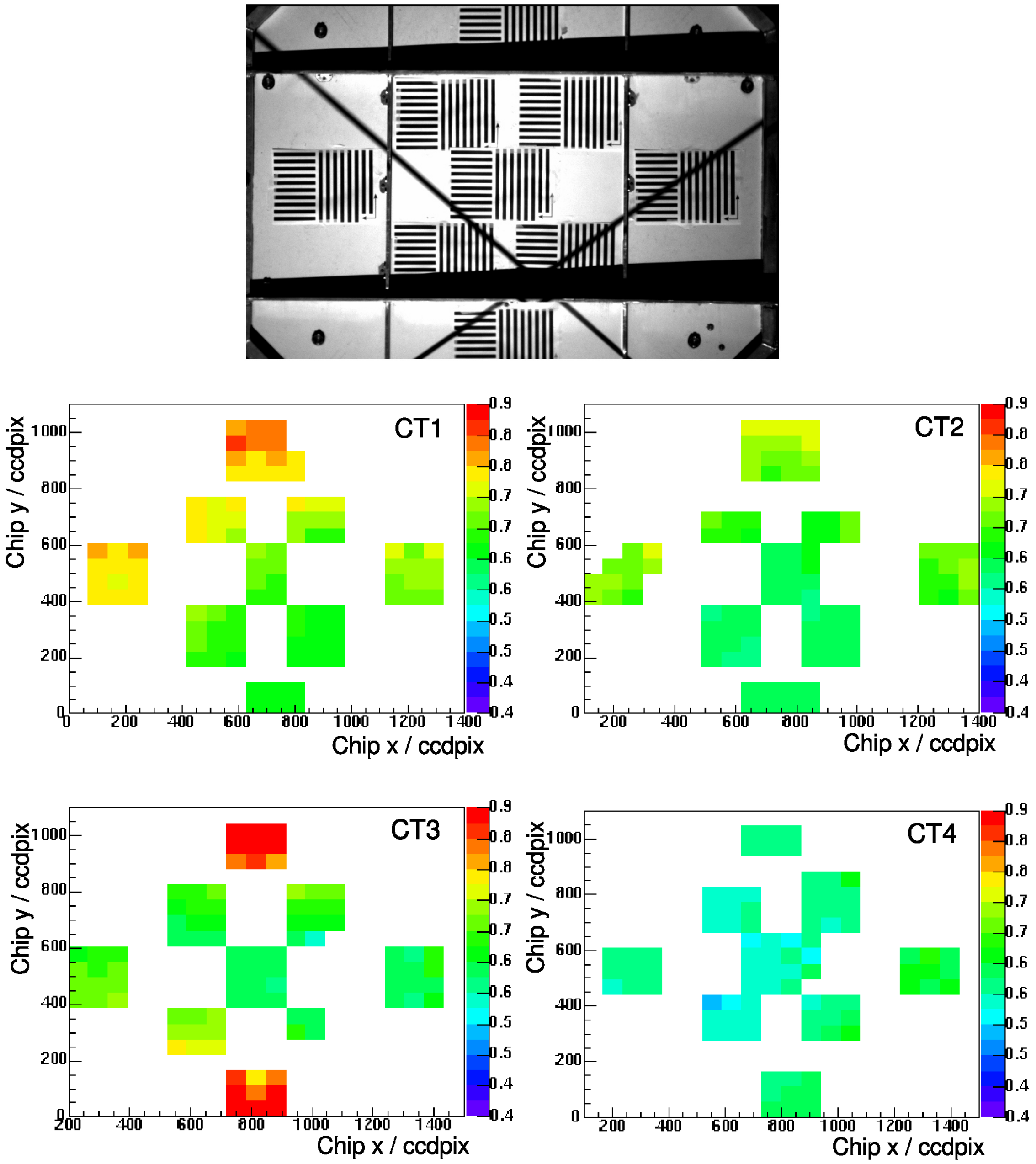

Figure B.2: **Image sharpness on CCD chip**. The values of Δ are determined at different locations on the CCD chip. CT1 and CT3 show a strong position dependence of the focus.

C Additional Information about the CCD-Cameras

The different rotations of the eight CCD cameras may cause some confusion when a user wants to interpret the CCD images directly without the transformations implemented in H.E.S.S.. Therefore sample images for each CCD type and CT (for the LidCCD see figure C.1, for the SkyCCD figure C.2) have been created as they would be seen in a fits viewing software like *fv* or *ds9*. The orientation of a regular Alt-Az coordinate system in the image is shown.

CCD Data are read out via parallel port to a computer in the electronics hut on the telescope for both cameras, but the SkyCCD data are amplified by a "remote boost unit" in the dish. This allows one to transfer SkyCCD data at the regular speed, while the reception of LidCCD data is slowed down artificially to avoid data confusion caused by dispersion in the 45 m long cables. The readout time of a full-frame image is less than two seconds allowing to measure short term variations. Since the corrections do not suffer extreme fluctuations in time, CCD exposures are not taken at the full rate to optimally use the limited lifetime of CCD shutters.

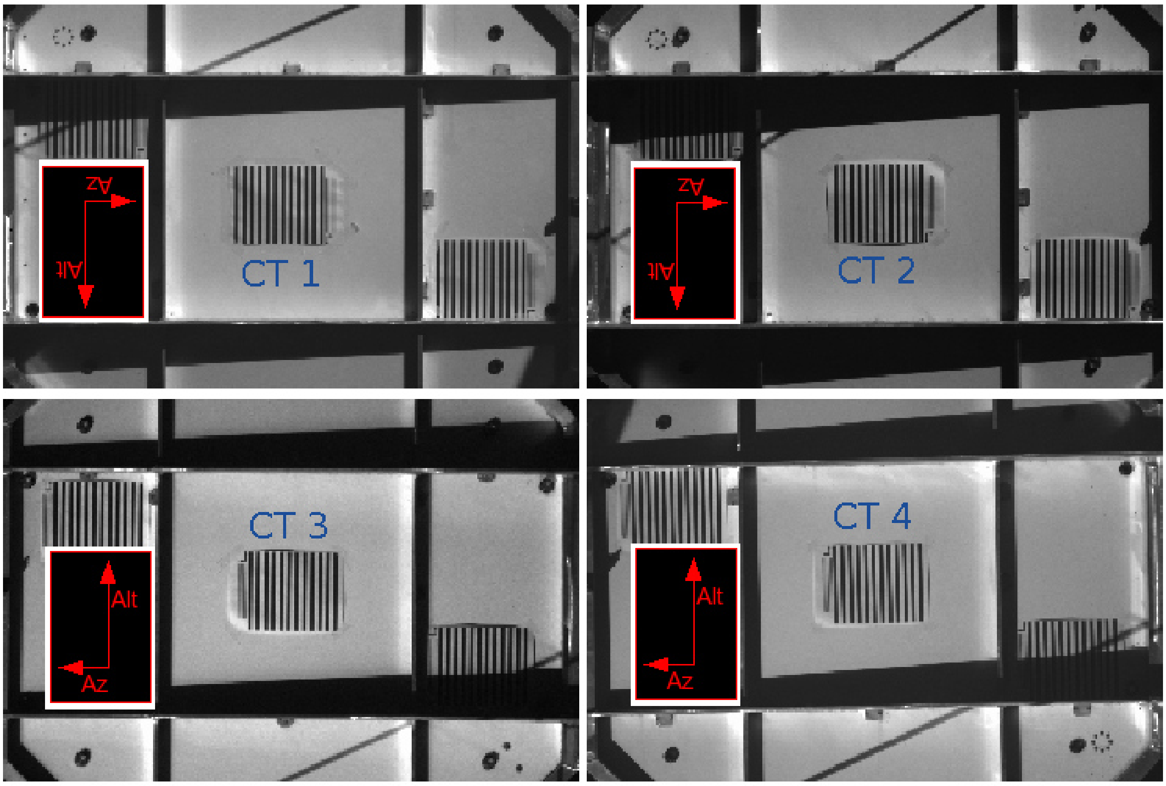

Figure C.1: **LidCCD Orientation** .

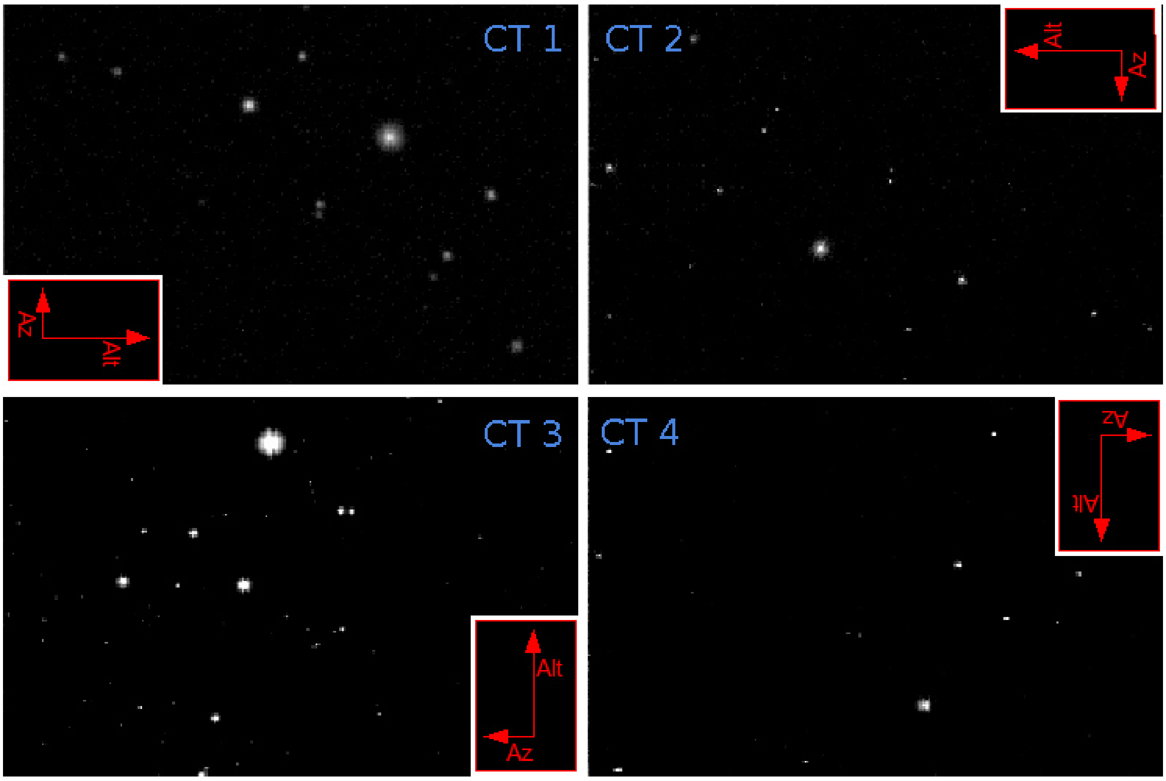

Figure C.2: **SkyCCD Orientation** .

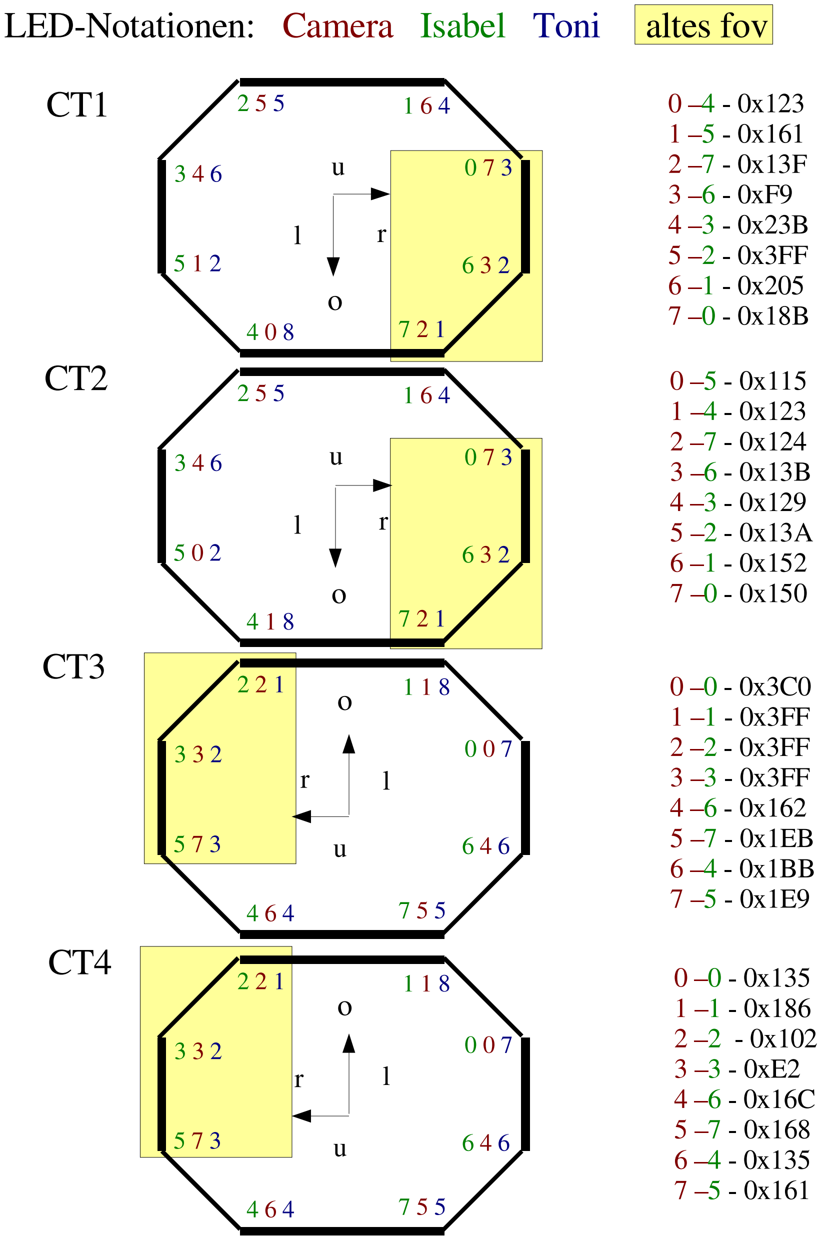

Figure C.3: **LED Notations** .

D Close look on hysteresis

As mentioned in chapter 4.1.4, inelastic deformations have been seen on the telescope CT1. The extensive investigations performed to find the cause for this problem and additional information on the comparison to the other telescopes (see figure D.1) are discussed here.

The following components are possible candidates for inelastic deformations. Some of them can easily be ruled out.

- positioning LED diffusors: all LEDs move sychoneously, therefore it is not caused by faulty diffusors or reflections.
- camera support masts: SkyCCD and LidCCD are affected in the same manner, so it is not caused by the masts.
- LidCCD mount: lasers attached to the LidCCD proved that the camera is fixed to the central hub. Hence it cannot be explained by a mere tilting of the CCD camera (see figure D.2).
- camera lock: the bolt securing the camera in the shelter exerts a force on the masts, that could cause the deformations. It was shown that no difference in parking in with or without closing the lock exist, so the lock is not the reason for the deformations (figure D.3).
- mirrors/mirror support structure: differences in the width of the reflected star show that the mirror support structure is affected. Since it is also seen in the SkyCCD and the camera centre, the mirror segments can't be the origin.

The park-in reset starts approximately at the horizon and increases gradually to the observed value. The stars follow a combination of two effects, one changes on the timescales of minutes, the other remains stable for hours, the short term effect is seen in all CTs and is not caused by the mirrors, because it is also seen in the SkyCCD. The consequences of this star movement will be discussed in the following section.

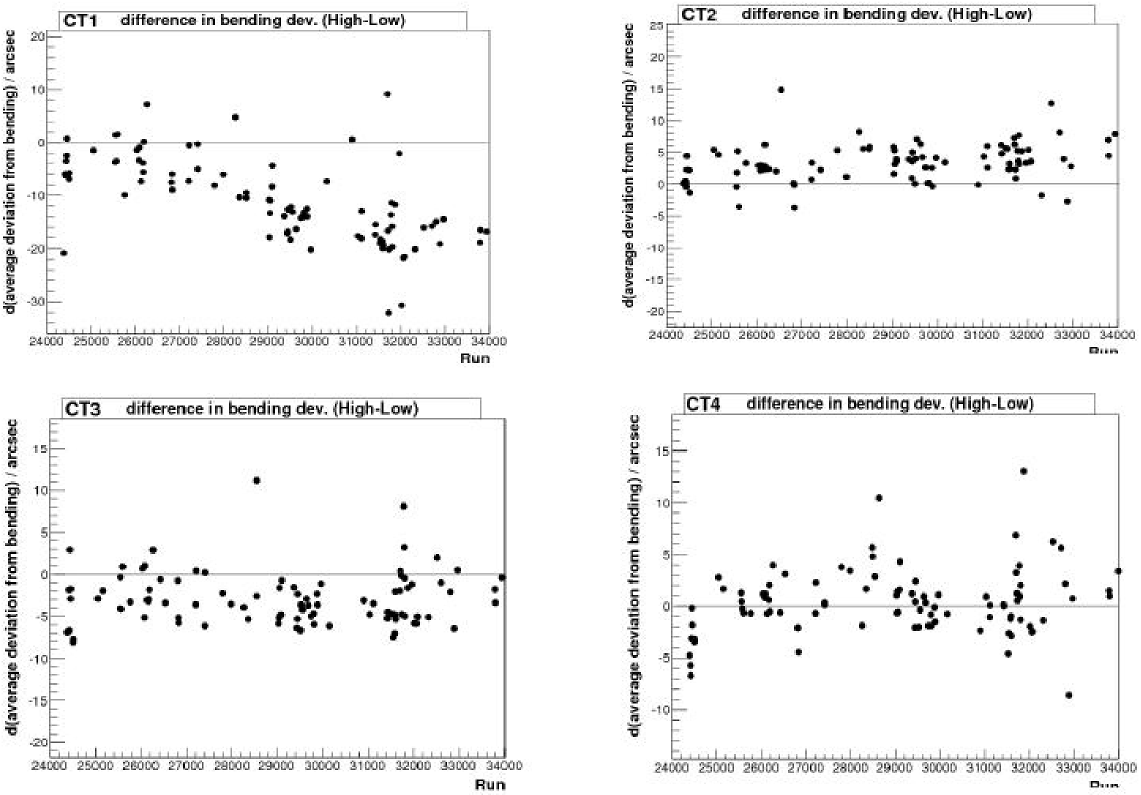

Figure D.1: **Comparison of the Development of the Hysteresis Magnitude** for all CTs between June 2005 and August 2006. Similar to figure 4.8, the camera centres measured in pointing and observation runs were divided according to the maximum altitude previously observed in that night. Different histograms were filled with the deviation from the expected bending curve for measurements where the telescope has been above 80° or stayed below 50°, until each contained at least 20 values. The means of those histograms were subtracted and plotted vs. run number. The increasing split in CT1 and the different direction of the effect in CT2 can be seen.

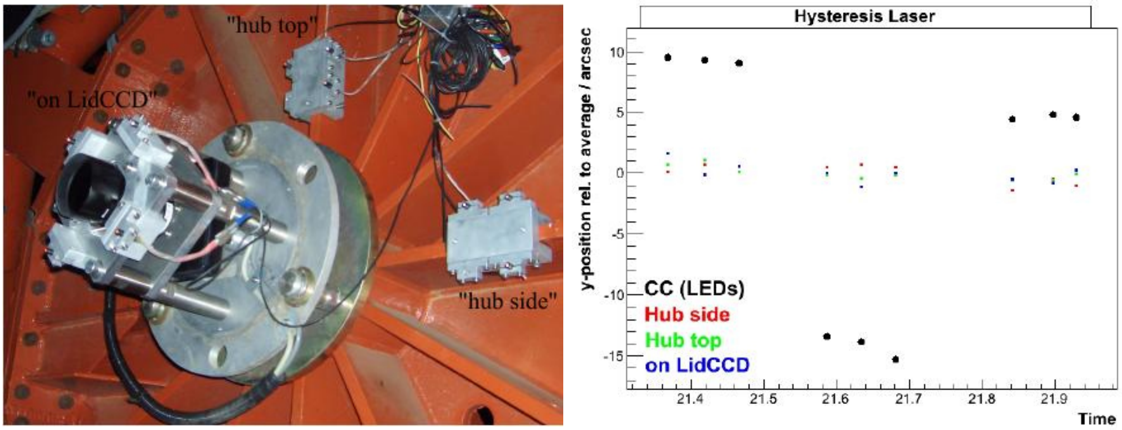

Figure D.2: **Lasers were attached to the LidCCD and the central hub** to investigate the stability of the LidCCD mount. The hysteresis test measurements show no movement of the laser spots comparable to those of the camera centre (CC). In addition, no significant difference between the lasers mounted directly on the structure holding the lens of the LidCCD (blue) and those mounted on the central hub could be seen. This confirms the stable connection between LidCCD and central hub.

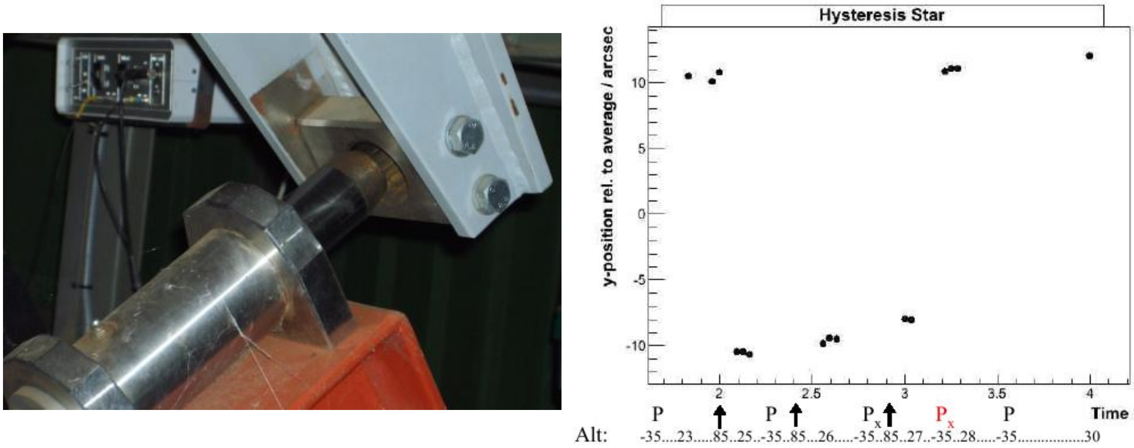

Figure D.3: **The influence of the camera lock** was investigated by a series of test runs. The figure shows that no difference exists between parking in with (denoted as **P**) or without closing the lock (marked as $\mathbf{P}_x$)

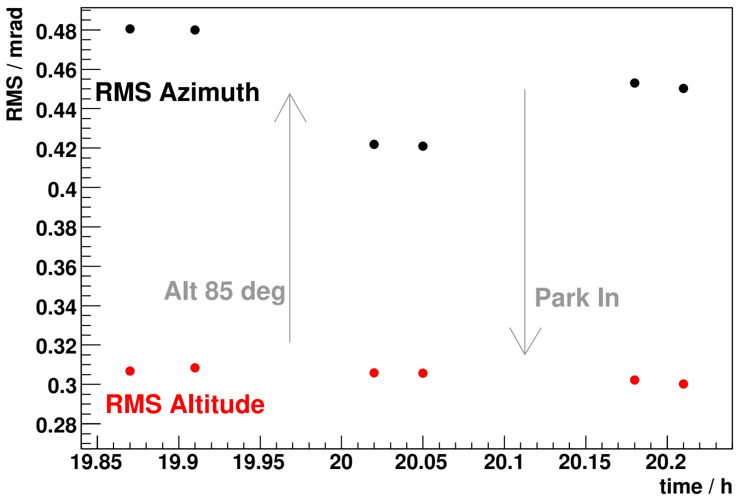

Figure D.4: **Star width in hysteresis test runs** at a star around 20° altitude. The shape of the central reflected star on the lid is influenced by the previous orientation of the telescope. The vertical (altitude) width remains unchanged, while the horizontal (azimuth) RMS, that is more affected by dish deformation, shows steps similar to the other observables. The spot is smaller after the telescope pointed to high altitudes, which can be explained by the fact that the mirror alignment was performed at higher altitudes.

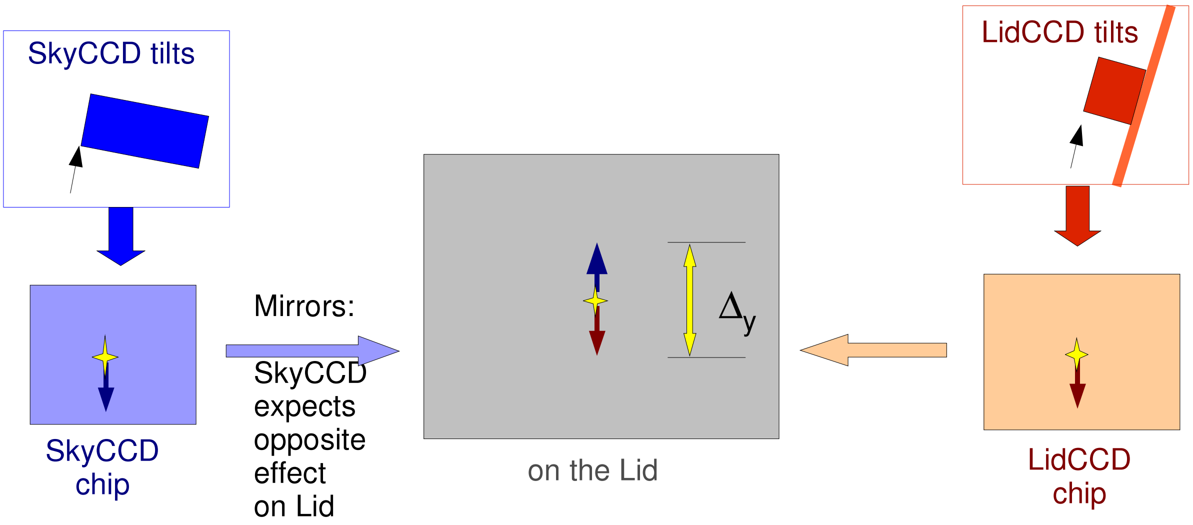

Figure D.5: **The influence of CCD/dish hysteresis on precision pointing** is demonstrated. Since movements of star images are assumed to go in different directions in the two CCD cameras, parallel effects add up.

The observed inelastic behaviour of the masts and camera centre is insignificant for the precision pointing approach. Yet, smaller changes have also been observed for the guiding stars in the Sky- and LidCCD. According to Fig. D.5, the effects in the two cameras do not cancel out, but add for the precision pointing method. Figure D.6 shows the apparent movements of the star images on the lid and in the SkyCCD being a superposition of the two effects mentioned above: the short-term movements in opposite directions and the long-term steps in a common direction that follow the hysteresis of the camera centre.

To visualise the remaining effect on precision pointing, the two deviations are added (sign change due to mirrors). Fig. D.6 shows a step of 15” for CT1. A similar behaviour with an amplitude of 6” can be seen for CT4, the other two telescopes show less significant steps of below 2”.

The short term effect behaves like a misorientation of the whole telescope (that is not seen in the shaft encoder information) and is therefore corrected in precision pointing.

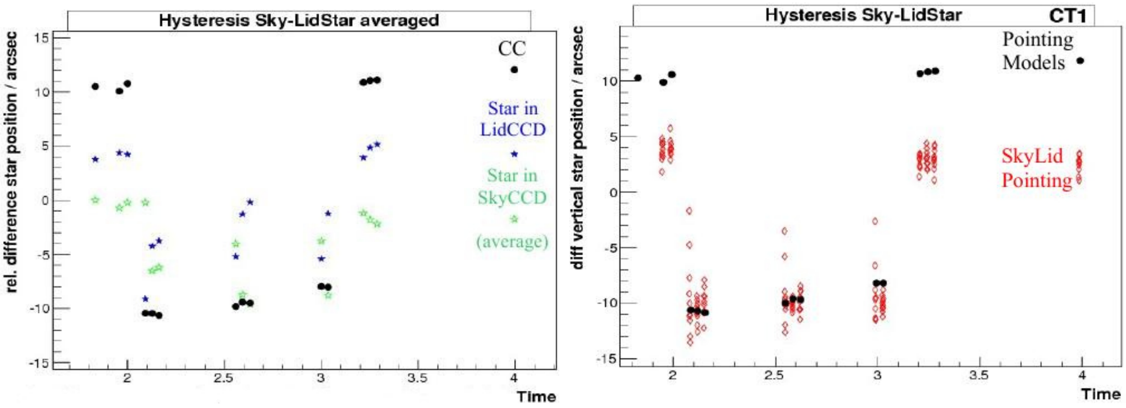

Figure D.6: **The star movement in hysteresis test runs** of the star position in the SkyCCD (green) and the reflected star in the LidCCD (blue) is a combination of a general long-term effect similar to the camera centre and a movement on the scale of minutes (positive values indicate higher altitudes, the normalisation is arbitrary). The correlation between the movements in both cameras is shown in the right figure, where the deviation in the LidCCD is deducted from the SkyCCD difference. The remaining step of about 15” at about 30° altitude influences precision pointing (here called "SkyLid Pointing").

List of Figures

Bibliography

[AAA06] J. Albert, E. Aliu, and H. Anderhub et. al. Observation of Gamma Rays from the Galactic Center with the MAGIC Telescope. *Astrophysical Journal*, 638:L101–L104, February 2006.

[AAV95] F. A. Aharonian, A. M. Atoyan, and H. J. Voelk. High energy electrons and positrons in cosmic rays as an indicator of the existence of a nearby cosmic tevatron. *Astronomy & Astrophysics*, 294:L41–L44, February 1995.

[Aha04a] F.A. Aharonian. *Very High Energy Cosmic Gamma Radiation.* World Scientific, 2004.

[Aha04b] Aharonian et al. (H.E.S.S. Collaboration). Calibration of cameras of the H.E.S.S. detector. *Astroparticle Physics*, 22:109–125, November 2004.

[Aha04c] Aharonian et al. (H.E.S.S. Collaboration). Very high energy gamma rays from the direction of Sagittarius A*. *Astronomy & Astrophysics*, 425:L13–L17, October 2004.

[Aha05a] Aharonian et al. (H.E.S.S. Collaboration). Discovery of Very High Energy Gamma Rays Associated with an X-ray Binary. *Science*, 309:746–749, July 2005.

[Aha05b] Aharonian et al. (H.E.S.S. Collaboration). Discovery of VHE Gamma Rays from PKS 2005-489. *Astronomy & Astrophysics*, 436:L17–L20, April 2005.

[Aha05c] Aharonian et al. (H.E.S.S. Collaboration). H.E.S.S. observations of PKS 2155–304. *Astronomy & Astrophysics*, 430:865, February 2005.

[Aha05d] Aharonian et al. (H.E.S.S. Collaboration). Observations of Mkn 421 in 2004 with H.E.S.S. at large zenith angles. *Astronomy & Astrophysics*, 95:437, June 2005.

[Aha06a] Aharonian et al. (H.E.S.S. Collaboration). A detailed spectral and morphological study of the gamma-ray supernova remnant RX J1713.7-3946 with HESS. *Astronomy & Astrophysics*, 449:223–242, 2006.

[Aha06b] Aharonian et al. (H.E.S.S. Collaboration). A low level of extragalactic background light as revealed by γ-rays from blazars. *nature*, 440:1018–1021, April 2006.

[Aha06c] Aharonian et al. (H.E.S.S. Collaboration). Fast variability of tera-electron volt rays from the radio galaxy M87. *Science*, 314:1424–1427, 2006.

[Aha06d] Aharonian et al. (H.E.S.S. Collaboration). HESS Observations of the Galactic Center Region and Their Possible Dark Matter Interpretation. *Physical Review Letters*, 97(24):249901–+, December 2006.

[Aha06e] Aharonian et al. (H.E.S.S. Collaboration). Observations of the Crab nebula with H.E.S.S. *Astronomy & Astrophysics*, 457:899–915, July 2006.

[Atk04] Atkins, R. et al. TeV Gamma-Ray Survey of the Northern Hemisphere Sky Using the Milagro Observatory. *Astrophysical Journal*, 608:680–685, 2004.

[BCD93] D. J. Bird, S. C. Corbató, and H. Y. Dai et. al. Evidence for correlated changes in the spectrum and composition of cosmic rays at extremely high energies. *Phys. Rev. Lett.*, 71(21):3401–3404, Nov 1993.

[BCC03] K. Bernlöhr, O. Carrol, and R. Cornils et. al. The optical system of the HESS imaging atmospheric Cherenkov telescopes. Part I: layout and components of the system . *Astroparticle Physics*, 20:111, 2003.

[Ber06] D. Berge. *A detailed study of the gamma-ray supernova remnant RX J1713.7-3946 with H.E.S.S.* . PhD thesis, Ruprecht-Karls Universität, Heidelberg, 2006.

[BG70] G. R. Blumenthal and R. J. Gould. Bremsstrahlung, Synchrotron Radiation, and Compton Scattering of High-Energy Electrons Traversing Dilute Gases. *Reviews of Modern Physics*, 42:237–271, 1970.

[Bol04] O. Bolz. *Absolute Energiekalibration der abbildenden Cherenkov-Teleskope des H.E.S.S. Experiments und Ergebnisse erster Beobachtungen des Supernova-Überrests RX J1713.7–3946* . PhD thesis, Ruprecht-Karls Universität, Heidelberg, 2004.

[Bro05] A.M. Brown for the H.E.S.S. collaboration. Atmospheric monitoring for the H.E.S.S. Cherenkov telescope array by transmissiometer and LIDAR. In *Proc. 29th ICRC*, August 2005.

[BUB98] L. Bergström, P. Ullio, and J. H. Buckley. Observability of Gamma Rays from Dark Matter Neutralino Annihilations in the Milky Way Halo. *Astroparticle Physics*, 9:137, 1998.

[BV04] J. H. Buckley and VERITAS Collaboration. Discovery of TeV Gamma-Ray Emission from the Galactic Center. In *Bulletin of the American Astronomical Society*, pages 945–+, August 2004.

[CDS07] CDS. SIMBAD Astronomical Database. http://simbad.u-strasbg.fr/simbad/, 2007.

[CFG89] M. F. Cawley, D. J. Fegan, and K. G. Gibbs et. al. Detection of TeV gamma rays from the Crab Nebula using the atmospheric Cherenkov imaging technique. *Irish Astronomical Journal*, 19:51–54, September 1989.

[CGJ03] R. Cornils, S. Gillessen, and I. Jung et al. The optical system of the H.E.S.S. imaging atmospheric Cherenkov telescopes. Part II: mirror alignment and point spread function. *Astroparticle Physics*, 20:129–143, November 2003.

[CGS97] J. Cronin, T.K. Gaisser, and S.P. Swordy. Cosmic Rays at the Energy Frontier. *Sci. Amer.*, 276:44, 1997.

[DC57] J. Davies and E. Cotton. Design of the quartermaster solar furnace. *Journal of Solar Energy Sci. and Eng.*, 1:16–20, 1957.

[Dev01] N. Devillard. Astronomical Data Analysis Software and Systems X. ASP Conf. Ser., 2001.

[DHH97] A. Daum, G. Hermann, and M. Hess et.al. First results on the performance of the HEGRA IACT array. *Astroparticle Physics*, 8:1–2, December 1997.

[Fer05] Ferenc, D. for the MAGIC Collaboration. The MAGIC gamma-ray observatory. *NIM A*, 553:274–281, 2005.

[FHH04] S. Funk, G. Hermann, and J. Hinton et. al. The trigger system of the H.E.S.S. telescope array. *Astroparticle Physics*, 22:285–296, November 2004.

[Fun05] S. Funk. *A new population of very high-energy γ-ray sources detected with H.E.S.S. in the inner part of the Milky Way.* PhD thesis, Ruprecht-Karls Universität, Heidelberg, 2005.

[Gil99] S. Gillessen. Überwachung der Abbildung eines Cherenkov-Teleskops und automatische Spiegeljustierung mit einer CCD-Kamera. Diploma thesis, 1999.

[Gil04] S. Gillessen. *Sub-Bogenminuten-genaue Positionen von TeV-Quellen mit H.E.S.S.* PhD thesis, Ruprecht-Karls Universität, Heidelberg, 2004.

[God07] Goddard Space Flight Center. http://imagine.gsfc.nasa.gov/docs/science/know_l2/pulsars.html, 2007.

[Gru00] Claus Grupen. *Astroteilchenphysik*. Vieweg, 2000.

[GS68] V. L. Ginzburg and S. I. Syrovatskii. On the Spectrum of Relativistic Electrons accelerated in Cosmic-Ray Sources. *Astrophysics and Space Science*, 1:442–+, 1968.

[GS69] V. L. Ginzburg and S. I. Syrovatskii. *The origin of cosmic rays.* Topics in Astrophysics and Space Physics, New York: Gordon and Breach, 1969.

[HAB06] J. Holder, R. W. Atkins, and H. M. Badran et al. The First VERITAS Telescope. *Astroparticle Physics*, 25:391, 2006.

[Hec01] Heck, D. et al. Extensive Air Shower Simulation with CORSIKA: A User's Guide . Forschungszentrum Karlsruhe, 2001.

[Hei54] W. Heitler. *Quantum Theory of Radiation.* Oxford University Press, 1954.

[Hes12] V.F. Hess. Über Beobachtungen der durchdringenden Strahlung bei sieben Freiballonfahrten . *Physikalische Zeitschrift*, 13:1084, 1912.

[Hil85] A.M. Hillas. Cerenkov light images of EAS produced by primary gamma rays and by nuclei. In *Proc. 19th ICRC*, pages 445–448, August 1985.

[HJK99] W. Hofmann, I. Jung, and A. Konopelko et al. Comparison of techniques to reconstruct VHE gamma-ray showers from multiple stereoscopic Cerenkov images. *Astroparticle Physics*, 12:135, 1999.

[Hör05] J. R. Hörandel. Overview on Direct and Indirect Measurements of Cosmic Rays. *International Journal of Modern Physics A*, 20:6753–6764, 2005.

[Jel58] J.V. Jelley. *Cerenkov Radiation and Its Applications.* Pergamon Press, 1958.

[JR75] F. James and M. Roos. Minuit A System For Function Minimization And Analysis Of The Parameter Errors And Correlations. *Comput. Phys. Commun.*, 10:343, 1975.

[KKZ97] H.V. Klapdor-Kleingrothaus and K. Zuber. *Teilchenastrophysik.* Teubner Studienbücher, 1997.

[Kuz06] C. Kuznetsov. private communication, 2006.

[Lev00] A. Levinson. Particle Acceleration and Curvature TeV Emission by Rotating Supermassive Black Holes. *Physical Review Letters*, 85:912, 2000.

[LFM94] A. Lukasiak, P. Ferrando, and F. B. McDonald et al. The isotopic composition of cosmic-ray beryllium and its implication for the cosmic ray's age. *Astrophysical Journal*, 423:426–431, March 1994.

[Lon94] Malcom S. Longair. *High Energy Astrophysics.* Cambridge University Press, 1994.

[Man06] Mantsch, P. for the Pierre Auger Collaboration. The Pierre Auger Observatory progress and first results, 2006.

[MBF02] Y. Maeda, F. K. Baganoff, and E. D. et al. Feigelson. A Chandra Study of Sagittarius A East: A Supernova Remnant Regulating the Activity of Our Galactic Centre? *Astrophysical Journal*, 570:671, 2002.

[Mol04] A.J. Molenaar. Analysis of images from a H.E.S.S. 'lidCCD' camera: influences on center finding precision. Internship report, Twente University, the Netherlands, 2004.

[Mor00] M. Mori. Status Report of the CANGAROO-III Project. In *High Energy Gamma-Ray Astronomy, Proceedings to the International Symposium on High Energy Gamma-Ray Astronomy (Heidelberg, Germany)*, 2000.

[Nau92] Nautical Almanac Offices. *Explanatory Supplement to the Astronomical Almamach*. University Science Books, 1992.

[PDH97] G. Pühlhofer, A. Daum, and G. Hermann et al. Locating TeV Gamma-Ray Sources with Sub-Arcminute Precision: the Pointing Calibration of the HEGRA System of Imaging Atmospheric Cherenkov Telescopes. *Astroparticle Physics*, 8:101–108, December 1997.

[PMB05] S. Park, M. Muno, and F. K. Baganoff et al. A Candidate Neutron Star Associated with Galactic Center Supernova Remnant Sagittarius A East. *Astrophysical Journal*, 631:964–975, October 2005.

[RV07] M. J. Rees and M. Volonteri. Massive Black Holes: formation and evolution. *ArXiv Astrophysics e-prints*, January 2007.

[SBB05] M. Schroedter, H. M. Badran, and J. H. Buckley et al. A Very High Energy Gamma-Ray Spectrum of 1ES 2344+514. *The Astrophysical Journal*, 634:947, 2005.

[SOG02] R. R. Schödel, T. Ott, and R. Genzel et al. A star in a 15.2-year orbit around the supermassive black hole at the centre of the Milky Way. *Nature*, 419:694, 2002.

[TEK04] K. Tsuchiya, R. Enomoto, and L. T. Ksenofontov et. al. Detection of Sub-TeV Gamma Rays from the Galactic Center Direction by CANGAROO-II. *Astrophysical Journal*, 606:L115–L118, May 2004.

[TG97] Mark Trueblood and Russel Merle Genet. *Telescope Control*. Willmann-Bell, 1997.

[UP95] C. M. Urry and P. Padovani. Unified Schemes for Radio-Loud Active Galactic Nuclei. *Publicatins of the Astronomical Society of the Pacific*, 107:803–+, September 1995.

[WCF89] T. C. Weekes, M. F. Cawley, and D. J. Fegan et. al. Observation of TeV gamma rays from the Crab nebula using the atmospheric Cerenkov imaging technique. *Astrophysical Journal*, 342:379–395, July 1989.

[Wie98] C.A. Wiedner. Site aspects of the H.E.S.S. project: astronomical and visibility conditions. H.E.S.S. internal note, 1998.

[WLG06] Q. D. Wang, F. J. Lu, and E. V. Gotthelf. G359.95-0.04: an energetic pulsar candidate near Sgr A*. *Nonthly Notices of the Royal Astronomical Society*, 367:937, 2006.

[Wul09] Th. Wulf. Über die in der Atmosphäre vorhandene Strahlung von hoher Durchdringungsfähigkeit. *Physikalische Zeitschrift*, 5:152–157, 1909.

[Yan98] H.-J. Yan. Improvement of astronomical refraction by mapping function. *Chinese Astronomy and Astrophysics*, 22:487–496, February 1998.

[ZEM05] ZEMAX Development Corporation. Software For Optical System Design, 2005.

Acknowledgements/Danksagungen

Abschliessend möchte ich noch kurz diese Gelegenheit für ein paar persönliche Worte des Dankes ergreifen. Viele Menschen haben auf die eine oder andere Weise so maßgeblich zu dieser Arbeit beigetragen, daß ihnen sicherlich weit mehr Anerkennung gebührt, als ich in diesen wenigen Zeilen ausdrücken kann.

Als erstes gilt mein besonderer Dank Prof. Dr. Werner Hofmann für die Möglichkeit, einen Beitrag zum H.E.S.S. Experiment leisten zu dürfen.

Prof. Dr. Stefan Wagner danke ich für die Übernahme des Korreferats.

Meinen Kollegen der Heidelberger H.E.S.S. Gruppe danke ich für die Unterstützung bei jeder aufkommenden Frage und das angenehme Arbeitsklima, insbesondere dem bestmöglichen Zimmerkollegen Dr. Oliver Bolz, Dr. Christopher van Eldik, Dr. Conor Masterson, Dr. Konrad Bernlöhr und Dr. German Hermann, die in unterschiedlichen Phasen meiner Arbeit jederzeit bereit waren, meine Fragen zu beantworten. Herrn Dalibor Nedbal danke ich außerdem fürs Durchhalten in jenen Nächten im Kontrollraum, Dr. Wystan Benbow für einen freien Tag im roten Sand und Herrn Stefan Hoppe sowie natürlich Dr. Andreas Förster für die Freundschaft und die vielseitigen Gespräche der letzten Zeit.

Herrn Jörg Baumgart und Herrn Frank Garrecht und dem Team der Werkstatt danke ich für die regelmäßige Hilfe während des praktischen Teils meiner Arbeit. Das gleiche gilt besonders auch für die Crew vor Ort, Herrn Toni Hanke, Herrn Eben Tjingaete und Maveipi Kanjii für den Einsatz und die Untertützung bei vielen Experimenten.

Ein besonderer Dank geht auch an Frau Ruth Crespo für die Betreuung in allen organisatiorischen Angelegenheiten.

Ausserdem danke ich meinen treuen Freunden, insbesondere Roman, unserem stets hilfsbereiten Latex-Spezialisten und Christin für die Gastfreundschaft wenn ich dringend Internet in weniger als 65 km Entfernung benötigte.

Der wichtigste Dank jedoch gilt meiner Familie: meinem Vater für die Sehnsucht nach dem Horizont und nach dem Wissen, meiner Mutter für den sicheren Halt, der mich mit Zuvericht den interessantesten Weg wählen läßt und die Unterstützung unterwegs, meiner großen Schwester und Freundin für den nie versiegenden Quell der Loyalität und des Vertrauens, auch die schwierigen Stellen zu meistern, und schließlich meinem geliebten Mann, der mir die Energie gibt, mit ihm voranzuschreiten und dabei wahrlich glücklich zu sein.